MŰEGYETEM 1782

Thermosensitive hydrogel – carbon nanoparticle composites

PhD Thesis

Barbara Berke

Supervisors:

Orsolya Czakkel

Krisztina László

NEUTRONS
FOR SOCIETY

2017

Acknowledgement

List of frequently used abbreviations

AUC	area under curve
CGO	GO prepared from natural graphite from China
CNP	carbon nanoparticle
CNP@PNIPAM	CNP containing PNIPAM composite gel
CNT	carbon nanotube
ESD	mass-based equilibrium swelling degree (m_{gel}/ m_{dry})
GO	graphene oxide
IPN	interpenetrating network
LCST	lower critical solubility temperature
m_{dry}	mass of the dry polymer network
m_{gel}	mass of the swollen polymer network
MGO	GO prepared from natural graphite from Madagascar
NSE	Neutron Spin-Echo
OZ	Ornstein-Zernike model
PNIPAM	poly(*N*-isopropylacrylamide) gel
Q	wave vector
R	cross-link density (mol cross-linker/ mol monomer)
RGO	reduced graphene oxide prepared from natural graphite from Madagascar
SANS	small-angle neutron scattering
SAXS	small-angle X-ray scattering
UCST	upper critical solubility temperature
VPT	volume phase transition
VPTT	volume phase transition temperature
ϕ	volume fraction of the polymer network
ξ	static correlation length
Θ	correlation length describing the structural inhomogeneities

Table of content

1.   Introduction

Responsive hydrogels are three-dimensional, cross-linked polymers that can absorb a large amount of water and are able to react to changes in their environment. Despite their numerous advantageous properties, they have certain drawbacks as well. Their poor mechanical strength, for example, limits their use in load-bearing applications. Limited drug uptake and its non-uniform distribution within the system, particularly in the case of hydrophobic drugs, could also compromise certain applications. These challenges may conceivably be overcome by composite hydrogels. Carbon nanoparticles (CNP) are widely used for strengthening in polymer nanocomposites. Recently they also got into the focus of interest as components of responsive polymer hydrogel nanocomposites. In these systems, CNPs may act not only as reinforcing agents but due to their special structure, infrared sensitivity, and tuneable conductivity, they can also provide new or modified sensitivity to these complex systems.

Nanotechnology developments have rapidly increased the interest in research on responsive polymer nanocomposites resulting in an increasing number of investigations on systems containing carbon nanofibers and nanotubes as well as graphene and its derivates. In spite of the long investigations, the knowledge on the relationship between the structure of the carbon fillers and the properties of the resulted composites is rather insufficient. In view of numerous potential applications (e.g., sensors, actuators, microfluidics, drug delivery vehicles, etc.), the lack of these details motivated the further studies in order to produce systems with tuneable properties.

In my thesis, a systematic study of the structural and dynamical properties of carbon nanoparticle containing poly(N-isopropylacrylamide) (PNIPAM) hydrogels is presented. Results on the structural and dynamic properties on both the micro- and macroscale are provided to gain a deeper understanding of the relation between the different scales.

2.   State-of-the-art

2.1.   Responsive polymer gels

Polymer gels are three-dimensional polymer networks filled with a fluid. Hydrogels, water-filled polymer networks, have been in the focus of scientific attention in the last few decades owing to their numerous beneficial properties like high water content and relatively good deformability [1,2]. Moreover, thanks to the physiochemical similarity of their network to the native extracellular matrix they are potentially biocompatible. Based on the physical nature of the main interactions in the gel matrix physical and chemical gels can be distinguished. Physical gels are formed through microcrystallization or the entanglement of polymer chains with noncovalent bonds, including electrostatic or hydrophobic interaction, hydrogen bonding and coordination bonds (Figure 1a). Chemically cross-linked hydrogels (chemical gels) are permanent networks formed via covalent bonds [3,4] (Figure 1b). There is a third group of gels, which might fit into both categories. The interpenetrating polymeric networks (IPN) are made of two, independent physically or chemically cross-linked component (Figure 1c).
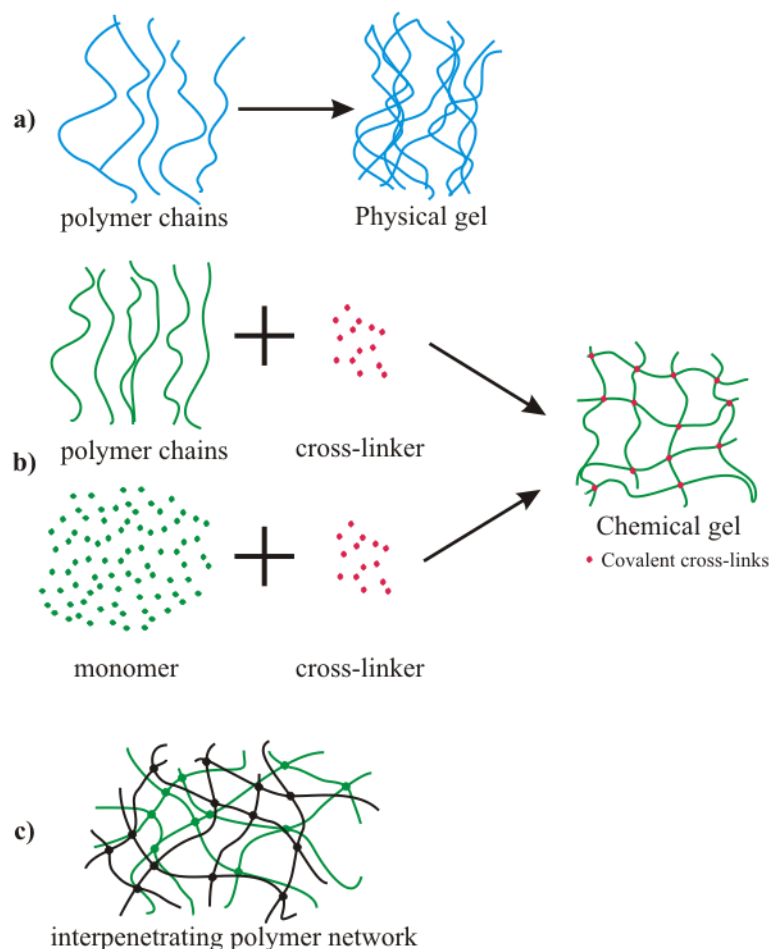
Figure 1. Physical- and chemical gels and interpenetrating polymer network.

The gel formation might start with linking of macromolecular chains together which initially leads to a progressively growing, branched, yet soluble polymer unit, whose final properties depend on the starting material [5]. The mixture of such, mostly polydisperse soluble branched polymer is called 'sol'. Continuation of the (cross-)linking process results in increasing the size of the branched polymer with decreasing solubility. This 'infinite' polymer is the gel or network and is permeated with a finite branched polymers (Figure 1). The transition from a system with finite branched polymer to infinite molecules is called sol-gel transition (or gelation) and the critical point where gel first appears is called the gel point [6]. Gelation can take place either by physical linking (physical gelation) or by chemical linking (chemical gelation) [5]. Chemical gels can also be prepared via direct synthesis when the polymerisation and the cross-link formation happen at the same time, i.e., monomers or monomer mixtures are used as initial material (Figure 1b). For determining the cross-link density (R), which strongly affects the properties of the prepared system, the molar ratio of the monomer and the cross-linker is used.

Hydrogels are complex systems with at least two components (polymer matrix + swelling agent). The polymer network can (in most of the cases reversibly) take up water (swelling) or expulse it (deswelling). The ratio of the two components in the equilibrium swollen state is governed by the occurring interactions during the mixing of the polymer matrix and the solvent and the structural characteristics of the polymer matrix itself [7]. The driving force of the volume change (=swelling or deswelling) is the desire to reach the thermodynamic equilibrium. The swelling process of gels is determined by two opposing effects, the osmotic pressure and the elastic restraining force of the network [8]. The Gibbs free energy of the gels is reduced by mixing it with a solvent; however, it is increased by the caused chain-deformation of the process.

$$\Delta G_{tot} = \Delta G_{mix} + \Delta G_{def} \tag{1}$$

where, G_{tot}, G_{mix}, and G_{def} are the Gibbs free energy of the system, the mixing and deformation process, respectively. The permanent junctions inside the chemical gels set the upper limit of the swelling [7]. This value, the equilibrium swelling degree (ESD) can be calculated from the mass (ESD_m) or volume (ESD_V) of the dry polymer network (m_{dry} or V_{dry}) and that of the swollen gel (m_{gel} or V_{gel}).

$$ESD_m = \frac{m_{gel}}{m_{dry}} \qquad\qquad ESD_V = \frac{V_{gel}}{V_{dry}} \tag{2}$$

In thermodynamic descriptions, instead of the ESD_V, its reciprocal value, the volume fraction (ϕ) of the polymer in the swollen state is commonly used.

Similarly to the Gibbs free energy of the gels, the chemical potential of the solvent has two components:

$$\Delta\mu_1 = \Delta\mu_{1,mix} + \Delta\mu_{1,def} \tag{3}$$

where $\Delta\mu_1$ is the difference between the chemical potentials of the solvent inside and outside of the gel. The chemical potential of the solvent as a function of the polymer's volume fraction is shown in Figure 2.
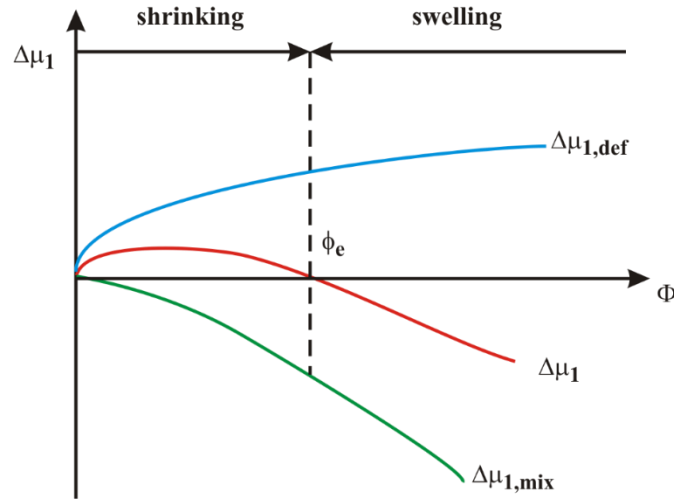
Figure 2. The chemical potential of the solvent as a function of the volume fraction of the polymer at a constant temperature. ϕ_e is the equilibrium volume fraction [7].

The system is in equilibrium (ϕ_e) if $\Delta\mu_1$=0. If $\Delta\mu_1$>0, the volume of the gel should decrease, while if $\Delta\mu_1$<0, the gel needs to swell to reach the equilibrium. The ESD, and therefore, the ϕ_e can be modified by changing the temperature, the composition of the solvent or the cross-link density of the gel.

Partially miscible polymer solutions, that behave similarly to the polymer gels, often exhibit two solubility boundaries, the upper critical solution temperature (UCST) and the lower critical solution temperature (LCST), which both depend on the molar mass and the pressure. At temperatures below LCST, the system is completely miscible in all proportions, whereas above LCST partial liquid miscibility occurs. LCST also depends on the composition, the degree of polymerization, as well as on the polydispersity and branching. For polymer gel systems with LCST or UCST, we can distinguish between negative and positive temperature sensitivity, respectively. Due to the same thermodynamic driving forces responsive gels exhibit a reversible volume phase transition (first reported by Tanaka [9]), that can be triggered by changes in certain environmental conditions [10,11], such as the nature of the swelling medium (composition [9], pH [12], ionic strength [12]), temperature [9,13,14], light

irradiation [15], electric [16] or magnetic field [17,18]. The phase transition can be continuous or sharp (collapse), during which the transport-, mechanical and optical properties of the gel change drastically. In the sharp volume phase transition of the responsive gel, the swelling medium of the polymer, along with its dissolved ions, molecules or drugs, is released into the surroundings upon a small change in the environment. This phenomenon makes the responsive systems very attractive for vehicles in drug delivery [19–22], sensors [23,24], actuators [25,26], microvalves [27], etc..

For applications relying on the responsiveness, the time scale of the phase transition is of incredible importance, therefore, the precise knowledge and tuneability of the response rate of swelling and deswelling is inevitable. Important to note that the reported shrinkage rate in case of temperature sensitive gels is usually about an order of magnitude slower than the swelling [28]. The swelling and shrinkage kinetics have been investigated in different thermosensitive gel systems in detail [29–46]. The direct, numerical comparison of the different results are sometimes difficult, as various materials and methods are in use, but all the authors agree on the main factors which influence the response rate [47]. These are the size and shape of the gel sample [48–51], the initial and final temperatures [46] and the swelling agent [52–54].

Gels are neither true liquids nor true solids. On short-range scales, they exhibit thermal fluctuations similar to those encountered in polymer solutions, but the monomer units are hindered not only because of spatial restrictions but cross-links as well [55]. For many years gels have been considered simply as swollen rubbers, but the experimental results were not in agreement with the rubber elasticity theory indicating a need for a more complex approach.

Polymer gels are highly deformable and exhibit a relatively low elastic modulus. This originates from the fact that elastic polymers do not store any potential energy in stretched chemical bonds. When the work is done upon them, all work is 'released' (not stored) and appears immediately in the polymer as thermal energy. It means that the ability of an elastomer to do work depends only on entropy-change considerations. The energy to do work comes entirely from thermal energy, and only the positive entropy change of the polymer allows its internal thermal energy to be converted efficiently into work.

It was commonly accepted that the structural properties of gels could be described in terms of the sole mesh size (i.e., the average strand connecting first neighbour cross-links along the network). However, experimental results suggested the presence of interactions at length scales larger than the mesh size (long-range fluctuations) [55].

10

The original theories of rubber elasticity are valid in principle for networks in the bulk as well as in the swollen state, if the elastic elementary chains are assumed to interact only at the cross-links. The conformations of the elementary chain are believed to be statistically independent, so the only length scale that defines the structure is the mesh size. This is the characteristic size of the system. These systems are 'idealized gels': their networks are filled with solvent and no correlations are believed to exist beyond the scale of the mesh and they fluctuate locally because of thermal agitation [55].

The gel structures are widely investigated by scattering techniques. Typical examples of a small-angle neutron scattering spectra (plotted on a log-log scale) of neutral gels can be seen in Figure 3, where the scattered intensity is plotted as a function of the wave vector (*Q*). (The detailed description of this method can be found in section 2.4.) In order to produce contrast, the networks, made of protonated polymer, were swollen in a deuterated, good solvent.
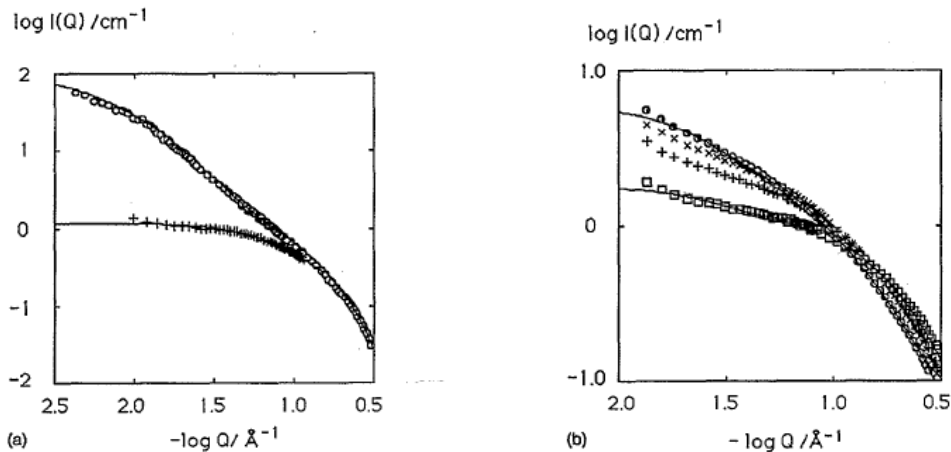
Figure 3. Small-angle neutron scattering spectra of neutral gels at maximum swelling (a) PVAc-toluene, (b) PDMS gels in toluene at different swelling degrees [56].

The scattering intensity from gels is much larger for the smaller wave vector values than that from the semi-dilute solution, although their shape is similar. At low *Q* in the saturation region the spectrum can be fitted satisfactorily to an Ornstein-Zernike [57] equation:

$$I(Q) = \frac{I(0)}{1+(Q\xi)^2} \tag{4}$$

where *I(Q)* is the measured intensity, *I(0)* is the extrapolated intensity, and ξ is the correlation length, which characterises the distance between the cross-links (~ mesh size). Some systems exhibit an upturn at very low *Q*. This effect, possibly arising from interchain associations or trapped impurities, might perturb the estimation of *I(0)* and ξ [55]. As ξ represents the

11

characteristic distance between intra-cluster and inter-cluster correlations, its value varies strongly with the swelling degree of the networks.

As the cross-link density increases and the equilibrium mass swelling degree decreases, there is often an increase of the scattering intensity at low Q owing to the concentration fluctuations that are amplified by the increasing number of cross-links [55]. On the other hand, the nature of the scattering signal is not affected strongly by the change in the cross-link density; however, small changes in the shape of the curves reveal the increase of the correlation length, i.e., the spatial fluctuations. This behaviour does not correspond to that of 'idealized gels'. The reason for the increase of the scattering intensity might be that a raise of cross-link density amplifies the 'thermal' fluctuations of polymer concentration. The second option is that quenched fluctuations of polymer concentration are formed and enhanced under the introduction of cross-links in the system. Lastly, non-homogeneous distribution of the cross-linkers can also cause excess scattering at low Q [55].

2.1.1. Poly(N-isopropylacrylamide)

PNIPAM (Figure 4) is one of the most popular temperature sensitive responsive hydrogels, owing to its peculiar volume phase transition temperature (VPTT) that is at ~34 °C, close to the temperature of the human body [9,19,58].
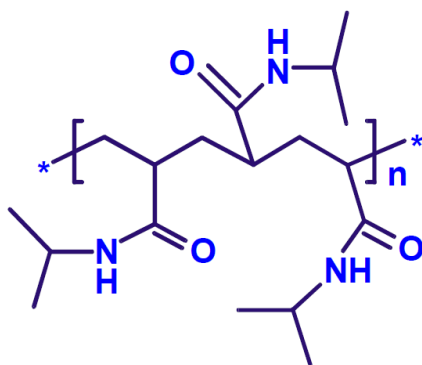
*Figure 4. Poly(*N-*isopropylacrylamide) (PNIPAM).*

The preparation of PNIPAM can be carried out by various methods, free radical initiation of organic solutions and redox initiation in aqueous media have been the most widely used-techniques [59]. *N,N′*-methylenebisacrylamide (BA) is the most commonly used cross-linker, which is probably a consequence of its structural similarity to NIPAM. Free radicals may be created by γ-irradiation or by the above-mentioned redox initiation. Typically used initiators are ammonium persulfate (APS) or potassium persulfate (KPS) where either sodium

metabisulfite or *N,N,N',N'*-tetramethylethylenediamine (TEMED) are used as the accelerators [59–61].

The PNIPAM hydrogel shows negative temperature sensitivity, i.e., its volume decreases with the increased temperature. Below its VPTT the hydrogel is swollen. In this state, due to the high water content, its refractive index is close to that of the water. Above the VPTT the gel becomes white and deswells. The VPT is an entropy-driven, reversible process [59], which is governed by the competition between the H-bonds and the hydrophobic interactions. During the collapse, the polymer dehydrates. The H-bonds between the water molecules and the polymer chains are stronger than those between the water molecules in the bulk [62,63]. This is why energy input is needed for the rearrangement of the water molecules (endothermic process), while the formation of new intermolecular interactions in the polymer system is accompanied by energy gain (exothermic process) [62–64]. At the VPTT the endothermic process is always more pronounced, resulting in an overall endothermic collapse [65].

The properties of the gel can be tuned by the parameters of the preparation procedure. Takata et al. [66] found that the preparation temperature strongly influenced the swelling behaviour of the systems. The equilibrium swelling degree increases with the preparation temperature up to 31.5 °C, which is due to the formation of a loosely connected network by clustering NIPAM domains. At higher temperatures, an incomplete network was formed, in which connectivity is locally lost. The shrinkage kinetics also showed a strong dependence on the preparation temperature. PNIPAM gels prepared above 25 °C exhibit faster VPT, which is explained by a network model containing spatial inhomogeneities, such as topological incompleteness and clustered structure.

The homogeneity of the formed gel structure depends as well on the cross-link density. When a higher amount of cross-linker is present in the precursor mixture, the viscosity increases faster, this way the diffusion of the components is hindered. Experimental data of Chetty et al. confirmed this description [67].

2.2. Polymer nanocomposites

Despite the already-mentioned advantages, hydrogels have certain drawbacks as well. The poor mechanical strength, for example, limits their use in load-bearing applications. Limited drug uptake and its nonuniform distribution within the system, particularly in the case of hydrophobic drugs, could also compromise certain applications. High water content combined with very wide pores often results in uncontrolled and/or undesirably rapid drug release [68,69], which can be detrimental to targeted drug delivery systems. These challenges

may conceivably be overcome by composite hydrogels. Due to the great diversity and the outstanding amount of attention in the field (>200.000 results on Google Scholar for "polymer nanocomposites" since 2010), in this chapter, I cite only some selected, representative articles.

Generally, polymer composites consist of at least two components and at least two phases. The filler materials are combined with the polymeric matrix to 'fill out' a certain required volume. This filling allows obtaining composites with modified properties. Moreover, the use of fillers might decrease the price of the final composite. These are the reasons why polymer composites are so widely used in industry nowadays.

Inorganic or organic materials that can be used as filler are classified according to the chemical family or to the geometrical features, such as shape, size and aspect ratio. Fillers may have a geometrical form of short fibres, flakes, platelets, spheres, or other irregular particles [70].

The widely used micrometric fillers may apply significant limitations to the applicability of the polymer composites by causing e.g., reductions in the strength of failure or impact resistance or fracture toughness. It appeared that this problem could be overcome by replacing the micro-sized fillers with fibres, platelets or spherical particles with nanosize dimensions.

Materials containing fillers having at least one dimension is in the range of 1-100 nm are known as nanocomposites [70]. These nanoparticles can be physically entrapped within the hydrogel matrix or chemically cross-linked to the hydrogel network via interfacial chemistry in order to obtain nanocomposite materials with enhanced characteristics such as improved mechanical strength or well-defined optical, thermal, electronic, and magnetic properties [71]. Nanoparticles due to size could provide numerous advanced and useful properties alone as well, but their applicability faces difficulties for example, because of the sometimes low biocompatibility and the difficulties in case of their handling. In turn, the preparation of hydrogel nanocomposites can provide benefits for the application of the nanoparticles too, such as generally enhanced biocompatibility, tuneable cell interactions, and improved control over drug release with higher loading capacities and better release characteristics [69,72].

The general philosophy of the fabrication of high-performance composite materials is to synergistically combine the strengths of multiple constituents and optimize the primary mechanical properties [73]. The degree of reinforcement of the composite depends mainly on the mechanical properties of the matrix and fillers selected for the preparation. The advantages of nanofiller based composites over microcomposites are that the former

contains a higher interfacial contact area allowing more effective interactions between the intermixed phases [70,74]. Additionally, the interactions between the filler particles within the polymer mixture are stronger and thus may increase the mechanical strength, the thermal stability and further factors that are relevant for the potential applications of composites. Because of the higher surface area of nanoparticles, complex preparation procedures, including controlled mixing/compounding and stabilization of the resulting dispersion, are required to obtain a homogeneous dispersion in the polymeric medium [75,76].

2.2.1. Preparation

To tailor and optimize the properties of the complex systems, it is necessary to disperse the nanoparticles homogeneously to ensure strong interaction and adhesion between the matrix and fillers [77,78]. Till date, various routes have been published which can be used for nanocomposite preparation. The most commonly used are the following.

- Solution mixing

   This is the simplest and probably most widely used method for processing nanocomposites in which the nanoparticle and polymer are mixed with a suitable solvent which then can evaporate in a controlled condition after forming nanocomposite films on the surface of the substrate [77,79,80]. To achieve better dispersion of the nanoparticles many variations has been demonstrated by researchers such as ultrasonic agitation [81,82], surface modification by adding functional groups for proper dispersion [83] or surfactants addition [84]. In some cases, agglomeration takes place after solvent evaporation. To avoid this problem, the drying method should be modified. Alternative techniques are spin casting [85] or electro-spinning [86,87].

- Melt processing

   The solubility of the polymers can be a limiting factor for the solution mixing approach. For thermoplastic polymers melt processing can be a preferred alternative [77,88–91].

   This method involves melting of polymer to form viscous liquid followed by blending with the nanoparticles. The homogeneity of the dispersion can be improved by shear mixing which can be achieved by extrusion and injection moulding techniques [88,92,93]. This technique is considered as less efficient than the solution mixing because high viscosity of thermoplastic polymers leads to hindrance in achieving uniform dispersion [94].

15

- *In situ* polymerization

  The main difference between this method and the previous two is that this route uses monomers instead of the polymers. The nanoparticle dispersion is mixed with the monomer matrix usually in the presence of a solvent, which is followed by standard methods of polymerisation. This technique may enable the grafting of polymer molecules onto the nanoparticles, which might cause better dispersion and stronger interactions between the nanoparticle and the host matrix. This method is applied mainly in case of insoluble or thermally unstable polymers [77].

To prepare polymer *gel* nanocomposites solution mixing or *in situ* polymerization can be applicable. For PNIPAM *in situ* polymerization is the most widely used [4,79,95–105]. These methods allow the preparation of both chemical and physical nanocomposite systems. In the network, covalent interactions occur between neighbouring polymeric molecules, and it is also possible to form covalent bonds between the surface groups of the filler and polymeric molecules. Non-covalent interactions, physical cross-linking, like hydrogen bonding, electrostatic interactions, coordination bonds and hydrophobic interaction, could also exist in these nanocomposite hydrogels [106]. However, the quantification of these chemical and physical interactions remains difficult [4].

2.2.2. Fillers

Among various reinforcing nano-sized components, clay, carbon nanoparticles, and metal/ceramic nanoparticles are the most common nanofillers employed in the past two decades to fabricate a variety of high-performance nanocomposite materials [107–115]. Clay nanoparticles (e.g., laponite, montmorillonite) possess excellent mechanical strengths and optical transparency, they are relatively cheap and can be pre-treated and dispersed in common solvents, even in an aqueous environment [4,107,109,116]. The 2D geometry of the montmorillonite nanoplatelets is also beneficial for their self-assembly in organized layered (laminated) morphologies, which are important for structural applications with unidirectional mechanical loads. The swelling and mechanical performance of these nanomaterials can show significant improvement compared to traditional composites [95,97,117,118]. However, because montmorillonite is a stiff inorganic platelet filler the flexibility and biodegradability of the laminated nanocomposite can be compromised [73].

Silica-incorporation results in better elasticity and faster swelling [119,120], while metal, metal-oxide [121] and carbon nanoparticle-content provide not only reinforcement but shows special optical properties [122,123] and electrical conductivity [122] as well.

Polymer matrix based, carbon nanofiller containing, multifunctional nanocomposites have sparked a widespread attention in the field of composite industry [77,124–126]. CNPs can have a positive impact on the physical and chemical properties of composites; these fillers have both low density and ease of recycling. Carbon-based nanofillers, e.g., carbon black (CB), carbon nanotubes (CNT), carbon nanofibers and recently, graphene derivatives such as graphene oxide (GO) and reduced graphene oxide (RGO) have been used as fillers in polymer nanocomposites [70].

2.3.   Composite gels with carbon nanoparticles

For many years, CB consisting of almost pure elemental carbon has been the most commonly used carbon filler in industry for the mechanical reinforcement and mechanical damping in synthetic rubbers, and for thermal and electrical modification of polymer materials [127,128]. Carbon blacks are mainly amorphous particulate materials, with moderate physicochemical properties in all major aspects. However, these fillers are abundant, can be readily functionalized, and are inexpensive. The surface-to-volume ratio of carbon black is lower than that of the activated carbon and its mechanical and electrical properties are not comparable to its crystalline carbon cousins, thus novel carbon-based fillers have been intensively studied in the past two decades. Graphite has also been used as a filler in polymer matrices for a long time, mainly to improve the thermal and electrical conductivities of composites [70]. Recently, organized carbon materials such as carbon nanotubes, fullerenes, and the graphene derivates have become much more sophisticated and popular nanostructures. These materials are seen as one of the most promising nanofilling materials because of their low density, extremely high aspect ratio (nanotubes, graphene), minute dimensions, outstanding mechanical and thermal properties, good chemical inertness, and tuneable electrical properties [108,111,129]. In biomedical applications, the possible toxicity of nanocarbons should also be considered. GO was reported to be non-toxic and highly biocompatible, however, CNTs demonstrated both negative and positive toxicological effects [130]. CNPs are also able to absorb specific stimuli (e.g., light) generating a local heating effect [100,131]. Reversible and fast optical response was observed under infrared (IR) laser excitation enabled by the strong light absorption property of nanoparticles in CNT [100,132,133] and

GO [100,131] containing hybrid PNIPAM hydrogels, so CNPs may act not only as reinforcing agents, but also provide new or modified sensitivity to these complex systems.

Besides all these studies done, the progress in nanocomposite development made using CNPs is still continuing and great challenges still remain to be addressed [73,134–136]. The poor aqueous dispersibility, stubborn contaminations, excessive aggregation, high cost, poor control of surface chemistries, and low interfacial interactions with the polymeric matrix are among the most critical unresolved issues. A limiting factor in the composite synthesis and processing is the challenge of obtaining a uniform and homogeneous dispersion of the fillers within the polymer matrix. CNTs entangle and aggregate due to their large aspect ratio and also due to their size. Graphene derivates have also shown the restacking phenomenon caused largely by the van der Waals forces and strong π–π stacking effects [129,137–139]. Apart from this, the host (polymer)-filler interfacial interactions play also a pivotal role in the load transfer between the carbon nanofillers and the host matrix.

The mechanical properties of the nanocomposite systems are widely investigated, but information regarding their effect on the responsive properties is less clear [140–142]. In case of these materials, not only the properties of the polymer matrix but also the character of the incorporated nanoparticle affects the responsive behaviour. Alam and coworkers [141] found that the temperature dependence of the pure and silica containing composite N-isopropylacrylamide-co-(3-methacryloxypropyltrimethoxysilane)] gel systems are not significantly different, but the change in the time dependence is more pronounced. The character of the shrinkage did not differ from that of the original, but the final swelling ratio increased with the silica content. In their systems, the silica filler acted as a cross-linking agent, which may explain the results. Xia and coworkers [140] found that the physical cross-links formed by incorporation of clay into the gel matrix slow down the response. On the other hand, introducing hydrophobic, short side-chains into the polymer facilitated the deswelling process owing to formation of water-release channels.

During my PhD work, I focused on graphene oxide and carbon nanotubes containing systems, which are presented more in details in the following chapters.

2.3.1. Carbon nanotubes

CNTs were first prepared by Radushkevich and Lukyanovich [143] in 1952, however, they got into the focus of scientific interest only after 1991, when Iijima published his famous papers in Nature [144,145] bringing revolutionary changes into the field. Carbon nanotubes

18

are basically graphene sheets (Figure 5) rolled up into cylindrical form either with an open end or capped with a half shape of fullerene structure.
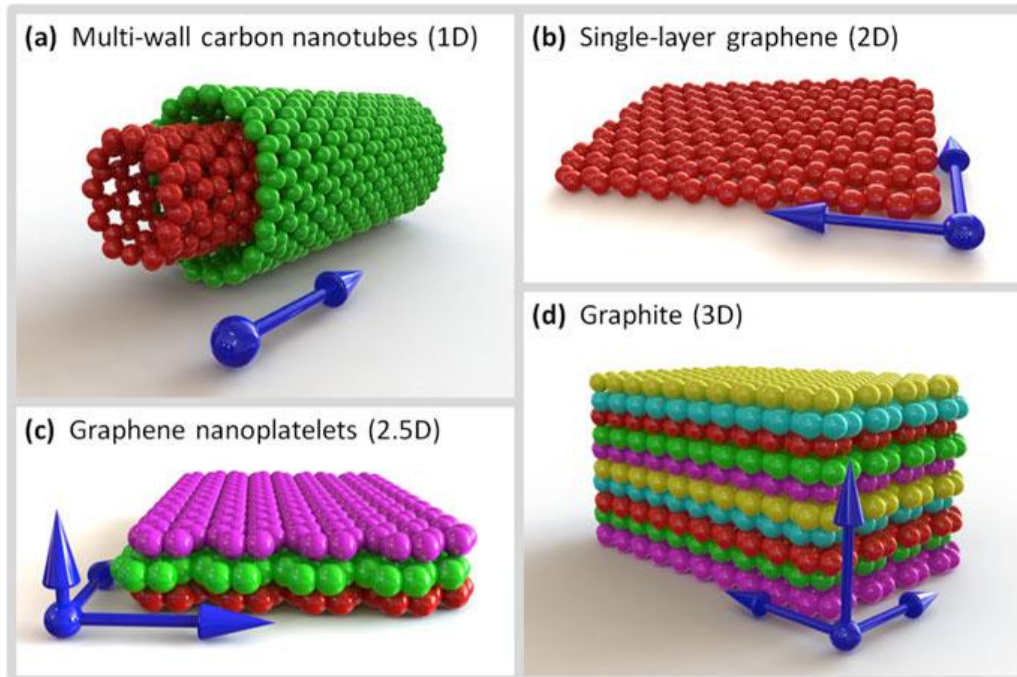
Figure 5. (a) Multi-wall carbon nanotube (MWCNT), (b) graphene,
(c) graphene nanoplatelets and (d) graphite [146].

There are two types of carbon nanotubes: single-walled nanotubes (SWCNTs) consisting of a single graphene layer and multi-walled nanotubes (MWCNTs) which are stacks of concentric tubes of several graphene layers in the form of cylinders with an interspacing of ~0.34 nm [147]. On the basis of atomic arrangement, three types of structures can be distinguished: zigzag, armchair, and chiral structures. Properties of CNTs are highly dependent on their structure, size, and diameter. Owing to their insolubility and hydrophobic character, they tend to aggregate in suspensions [148], however, their dispersibility and compatibility with polymer matrices can be improved by functionalization. The usual specific surface area of SWCNTs and MWCNTs are 400-900 m^2/g and 200-400 m^2/g, respectively [149].

CNTs have highly unique mechanical, electrical and thermal properties. Even though that their very small size makes the direct characterisation challenging [150], various experimental techniques (e.g., scanning electron microscopy – SEM, transmission electron microscopy – TEM, atomic force microscopy – AFM, Raman spectroscopy, nanoindentation) and theoretical models (e.g., ab-initio model, molecular dynamics, continuum model) have been used to describe their mechanical properties [151–153]. Theoretical studies concluded that

depending on the diameter and the chirality of the tube, CNTs may be either metallic or semiconducting [154] and have high thermal conductivity [155,156].

CNTs can be produced via various methods [157,158]. All of them requires a carbon-atom source, most often graphite, hydrocarbons [159] or carbon monoxide [149], a catalyst (typically Fe, Ni, Co, Mo, or a mixture of these), and energy. Arc discharge [144], laser ablation [160] or chemical vapour deposition (CVD) [149] are all widely applied. High-quality CNTs are produced at laboratory scale by the laser ablation method. CVD is the most commonly used method, especially on a large-scale, however, CNTs produced by this method contain structural defects and impurities due to the catalyst and amorphous carbon. Several methods can be used for purification. Non-oxidizing acids can get rid of the left-over catalyst [161−163]. The amorphous carbon, being more reactive in oxidation reactions, can be removed by oxidation. H_2O_2 [163], HNO_3 [164], $KMnO_4$ [165], etc. As these methods are not selective, they may destroy the structure of the nanotubes, resulting in wall defects or even shortening of the nanotubes [166]. The highly fractured outermost wall often remains adsorbed on the carbon nanotube surface. These fractions are similar to fulvic acids and can be removed with basic aqueous solutions [148]. This purification step is based on the electrostatic repulsion of the negatively charged carbon surface and the deprotonated functional groups of fulvic acid.

2.3.1.1. *CNTs in composites*

CNT incorporation into polymer matrix might enhance properties of the resulted materials [77,150,167], which usually depends on the interactions at the interface between the CNT and the surrounding polymer matrix. Mechanical reinforcement can be performed via transferring stress from the matrix to the CNTs. This transfer depends on the strength of the interactions. As perfect CNTs cannot form chemical bonds [168] with the polymer matrix without prior surface modification of the nanotubes, they are only weakly bonded. If one considers the surface of a CNT, essentially an exposed graphene sheet, it is not surprising that interfacial traction is a concern. Numerous researchers have attributed lower-than-predicted mechanical properties to a lack of interfacial bonding [169,170]. On the other hand, significant toughening of polymer matrices through the incorporation of CNTs via different methods has also been reported [171−175] due to strong interactions between the CNTs and the polymer matrix.

A number of studies show that the change in the mechanical properties of the nanocomposites does not scale with the CNT content of the polymer matrix: after a critical concentration, the

mechanical properties deteriorate with increasing critical loading of CNTs, sometimes even below the pure matrix material [176,177].

In hydrogels, in order to conserve the advantageous properties of the polymer matrix, the applicable amount of filler is limited. A low CNT-content was shown to improve the properties of PNIPAM hydrogel, but the resulted nanocomposite gels were found to be more hydrophobic, with lower contact angle and decreased mass swelling degree [178,179]. Chen et al. [178] reported that the MWCNTs can form an interpenetrating network within the gel matrix, resulting in thinner pore walls and increased modulus in the composite. Zhang et al. used SWCNTs for their experiments. Upon NIR-irradiation the composite systems showed ultrafast optical response with a response time that is inversely proportional to the CNT-content [133]. Fujigaya et al. also found a faster response with increasing CNT content. They also determined that the VPTT does not change upon the CNT incorporation [180].

Along with formed interactions and dispersion, aspect ratio, length, and alignment of CNTs also change the various properties of composites [77,90,181,182].

A number of studies revealed [78,81,85,183,184] that the introduction of CNTs into a polymer matrix may result in conducting nanocomposites with new, electrical properties. These conducting nanocomposites follow the principle of percolation theory which explains the transition from insulator to conductor in materials. Accordingly, at low CNT-content the composites exhibit low conductivity, but at the percolation threshold, a small increase in loading will result in a drastic increase in conductivity, owing to the formation of continuous conducting networks. Above this percolation transition range, the conductivity of the composites gets saturated [135,185].

For a statistical distribution of filler particles, the excluded volume concept gives ~0.1 wt% as a percolation threshold for CNTs with the aspect ratio of 1000, however, significantly lower percolation thresholds have been reported experimentally. This is explained by a kinetic percolation phenomenon, which allows for particle movement and reaggregation in the system [135]. The numerical value of the percolation threshold depends strongly on the applied determination method. In many cases, the percolation threshold level is obtained from changes measured in the mechanical properties of the systems since the formed continuous network results in a jump in the mechanical properties as well. Rheological percolation occurs at a lower concentration than electrical percolation because filler particles can interact with each other via polymer chains improving the mechanical properties, whereas direct contact is required for electrical conduction [135].

Allaoui et al. showed that the percolation threshold value for MWNT/epoxy composites is around 0.5–1 wt% [186]. Aguilar et al. [187] found that the conductivity of the agglomerated films was 2–4 orders of magnitude higher than the uniformly dispersed films which can be explained by the increased density of CNT–CNT junctions. However, some studies indicate that electrical conductivity of the matrix significantly decreases by chemical functionalization of the CNTs due, on one hand, to the imbalance in the polarization effect and the occurring physical structure defects [77] on the other. The exact percolation threshold depends also on various factors such as aspect ratio, dispersion, alignment, functionalization, processing, polymer type, etc [156,186–188].

Martin-Gallego et al. [189] compared the percolation network of CNT and graphene fillers in the epoxy nanocomposites. They concluded that the most efficient and promising filler for composite preparation is graphene, which will be discussed in the following section. Important to note that the percolation threshold of the GO containing composites (reported in the range of 0.1 – 5 weight% - Table 1) depends strongly on the properties of the polymer matrix and the used nanoplatelets.

Table 1. Percolation threshold of GO derivates-based composites in the literature.

Polymer matrix	Reported percolation threshold	Reference
poly(vinyl alcohol)	0.7 weight%	[76]
PNIPAM	5% weight ratio of GO/NIPAM	[104]
polystyrene	$\geq$0.1 volume%; 0.9 weight%; 0.09 volume%	[190, 197, 198]
theoretical study	<0.5 weight%	[191]
vinyl chloride/vinyl acetate copolymer	0.15 volume%	[192]
polyurethane	<0.5 volume%	[193]
poly(methyl methacrylate)	0.26 weight%	[193]
epoxy	0.12 volume% 0.88 weight% 1 and 0.3 weight% 0.52 volume%	[194-196, 199]

2.3.2. *Graphene and its derivates*

2.3.2.1. *Graphene*

Graphene is the name given to a flat monolayer of carbon atoms tightly packed into a two-dimensional (2D) honeycomb lattice (Figure 5), and is a basic building block for graphitic materials of all other dimensionalities. It can be wrapped up into 0D fullerenes, rolled into 1D nanotubes or stacked into 3D graphite [200]. Graphene was used in theoretical studies for describing properties of various carbon-based materials. It was known as integral part of 3D materials, like graphite or activated carbons, but was presumed not to exist in the free state [200]. The 'graphene gold rush', as Andre Geim and Konstantin Novoselov called it, reached its peak in 2010 when the Nobel Prize was attributed to them.

The popularity of graphene can be easily explained by its outstanding properties. It has a large theoretical specific surface area (2630 m^2/g), high intrinsic mobility (200 000 cm^2/vs) [201], high Young's modulus ($\sim$ 1.0 TPa) [202] and thermal conductivity ($\sim$ 5000 W/mK) [203], and its optical transmittance ($\sim$ 97.7%) [204] and good electrical conductivity merit attention for many potential applications [205]. In its structure, carbon atoms with sp^2 structure are connected to each other with covalent bonds, while every atom is left with one free electron. These electrons form a delocalized π electron-structure, which is responsible for the unique thermal and electrical properties. The electrons have high mobility, which makes the graphene a zero-gap semiconductor [200].

There are now four primary ways to produce 'pristine' graphene. As a bottom-up method, it can be grown on epitaxially matched metal or SiC surfaces by CVD. This method can be in principle extended to 'endless length, very large width' production simply by exposing appropriate foils to C to achieve surface deposition of either monolayer or multilayer [205,206]. Top-down methods, on the other hand, are still more widely used. Micromechanical exfoliation can be used to generate 'high quality' graphene that is electrically isolated for fundamental studies of transport physics and other properties but does not appear to be scalable to large area yet. It typically produces graphene "particles" with lateral dimensions on the order of tens to hundreds of micrometers [205,206]. Exfoliation of graphite can also be performed in solvents. This is typically done by exposure of graphite powders in organic solvents such as DMF or NMP to high-intensity ultrasound, and while significant progress has been made, the yield is relatively low [205,206]. The last method is to produce graphene by the reduction of graphene oxide (Figure 6). This will be discussed in sections 2.3.2.2.
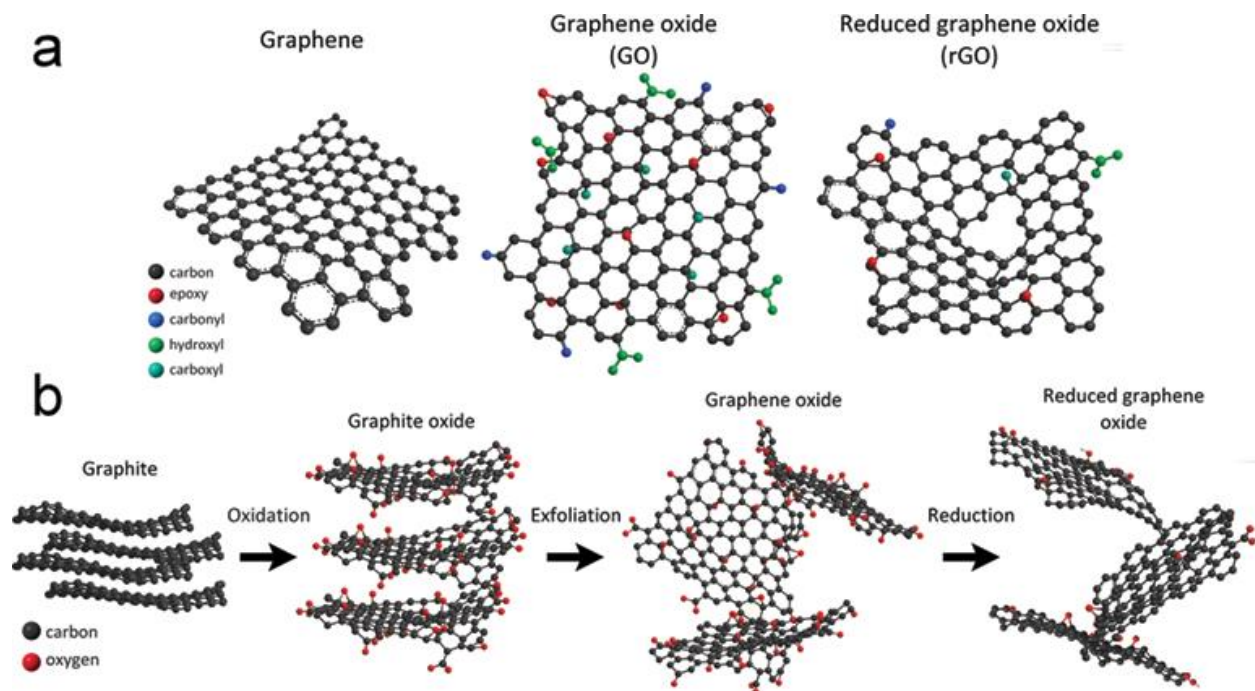
Figure 6. (a) Schematic chemical structures of graphene, graphene oxide, and reduced graphene oxide. (b) Route from graphite to reduced graphene oxide [207].

2.3.2.2. *Graphene oxide*

Graphene has many specific properties (e.g., excellent heat and electrical conductivity or light sensitivity) which would be beneficial, but its hydrophobicity hinders strongly the use in hydrogels. On the contrary, GO, which is a damaged graphene layer, decorated with vacations and oxygen-containing functional groups, forms a stable aqueous suspension. The structure of the GO is still under debate. The two most widely used models are the Dékány- [208] and the Lerf-Klinowski-model [209]. GO is nonstoichiometric with an inhomogeneous structure (Figure 6). The edge of the sheets is usually decorated by carbonyl- or carboxyl groups, while in-plane mostly epoxy- and hydroxyl groups can be found. GO often contains structural defects (single vacancies, Stone-Wales defects, etc.) [210]. The chemical structure affects strongly the physical characteristics as well. The oxygen-containing functional groups hinder the attraction of the separated sheets, the hydroxyl and carboxyl groups allow the formation of H-bonds and facilitate dispersion preparation. On the other hand, due to the corrupted sp^2 structure, its properties are far from those of graphene.

The preparation of GO was first published, unconsciously, by Brodie [211] in 1859. He described a process that involves the addition of $KClO_3$ (in one step) to a slurry of graphite in fuming nitric acid (HNO_3). The overall mass of the resulted material increased and

analytical methods revealed that the obtained material was built up by carbon, hydrogen, and oxygen atoms. Forty years later, Staudenmaier [212] improved Brodie's method by adding the chlorate in multiple aliquots over the course of the reaction and increasing the acidity of the mixture with concentrated H_2SO_4. The main drawback of this process was that it needed four days. In 1957, Hummers and Offeman developed an alternative oxidation method by reacting graphite with a mixture of $KMnO_4$, $NaNO_3$ and concentrated H_2SO_4 [213]. By using $KMnO_4$ instead of $KClO_3$ one can avoid the formation of the explosive ClO_2, moreover, the reaction can be carried out in a couple of hours. However, the formation of poisonous NO_2 and N_2O_4 gases still cannot be avoided completely. This recipe has been improved by Marcano et al. [214,215]. They added H_3PO_4 to the system and excluded $NaNO_3$, which helps the intercalation and causes less structural defects in the product. Importantly, it has been recently demonstrated that the properties of the obtained GO products show strong variance, depending not only on the particular oxidants used but also on the graphite source and reaction conditions [214,216].

2.3.2.3. *Reduced graphene oxide*

RGO (Figure 6) can have great potential in hydrogel nanocomposites as its properties are close to that of the graphene, but its hydrophobicity is decreased [217]. Several chemical and physical routes are available for partially restoring the honeycomb structure and removing the functional groups of graphene oxide in order to prepare RGO [218]:

- Thermal annealing:

    GO can be reduced solely by heat treatment. By using rapid heating (>2000 ºC/min) it is possible to exfoliate and reduce graphite oxide at the same step. Due to the removal of the oxygen-containing functional groups CO, CO_2, and water are produced [218]. The heat treatment is performed in various atmospheres [218] [inert (N_2) or reducing (H_2, NH_3)] or in vacuum. By changing the temperature, the atmosphere and the length of the treatment, the properties of the produced RGO can be tuned in a wide range, however, this procedure is found only to produce small-sized and wrinkled graphene sheets [219]. This is mainly because the decomposition of oxygen-containing groups removes also carbon atoms from the carbon plane, which splits the graphene sheets into small pieces and results in the distortion of the carbon plane [218]. The method is simple but consumes a great amount of energy [218,220], produced via thermal,

microwave or light irradiation, which usually makes the process more expensive and complicated.

- Chemical reduction:

Reduction by chemical reagents is based on their chemical reactions with GO. Usually, the reduction can be realized at room temperature or by moderate heating. As a result, the requirement for equipment and environment is not as critical as that of thermal annealing treatment, which makes chemical reduction a cheaper and easily available way for the mass production of graphene compared with thermal reduction.

The reduction of graphite oxide by hydrazine was used before the discovery of graphene [221], therefore it is not surprising, that hydrazine, along with its derivates, e.g., hydrazine hydrate and dimethylhydrazine [190] is still the most widely used reducing agent. The process is made by adding the liquid reagents to a GO aqueous dispersion, which results in agglomerated graphene-based nanosheets due to the increase of hydrophobicity [218].

Metal hydrides, e.g., sodium hydride, sodium borohydride ($NaBH_4$) and lithium aluminium hydride, have been accepted as strong reducing reagents in organic chemistry, but unfortunately, they are dangerous due to their slight to very strong reactivity with water, which is the main solvent for the exfoliation and dispersion of GO [218].

Ascorbic acid (Vitamin C) is an efficient reducing reagent for GO, which is considered to be an ideal substitute for hydrazine. Fernandez-Merino et al. [222] revealed that GO reduced by Vitamin C can have a C/O ratio of about 12.5 and a conductivity of 77 S/cm, which are comparable to those produced by hydrazine in a parallel experiment. In addition, Vitamin C has the great advantage of its non-toxicity in contrast to hydrazine. It is also stable in water, which makes it much more attractive than the metal hydrides. Furthermore, the reduction in suspension does not result in the aggregation of RGO sheets as produced by hydrazine, which is beneficial for further applications [218].

Recently, Pei et al. [223] and Moon et al. [224] reported the use of another strong reducing reagent, hydroiodic acid (HI). This method can be realized using GO in suspension, powder or film in a gas or solution environment, even at room temperature [224] giving a great advantage to this method, however, the high price of the HI present a significant drawback.

- Further methods:

Different from the photothermal reduction mentioned above, GO can also be reduced by photo-chemical reactions with the assistance of a photocatalyst like TiO_2, ZnO or $BiVO_4$ [218,220]. Before the reduction, the carboxyl groups in GO sheets can interact with the hydroxyl groups on the TiO_2 surface by charge transfer, producing a hybrid between the TiO_2 nanoparticles and the GO sheets, which can be retained after reduction.

Another emerging chemical reduction method is solvothermal reduction [225–227]. A solvothermal process is performed in a sealed container so that the solvent can be brought to a temperature well above its boiling point by the increase of pressure resulting from heating [228]. In a hydrothermal process, overheated supercritical water can play the role of reducing agent and offers a green chemistry alternative to organic solvents. In addition, its physiochemical properties can be widely changed with changes in pressure and temperature, which allows the catalysis of a variety of heterolytic (ionic) bond cleavage reactions in water [218].

2.3.2.4. *Graphene derivates in composites*

Graphene has many specific properties (e.g., the highest possible specific surface area, excellent heat and electrical conductivity or light sensitivity) which would be beneficial, but its hydrophobicity hinders strongly the use in hydrogels [75]. On the contrary, GO forms stable aqueous suspension. GO is considered to be non-toxic and highly biocompatible [130], which favours its use in biomedical applications. Moreover, incorporation of GO gives visible [229] or near infrared light [100,101,131] sensitivity to the composite systems, which extends their potential, for example, as NIR controlled microvalves, artificial muscles or actuators. However, due to the corrupted sp^2 structure, its properties are far from those of graphene. As mentioned above, several chemical and physical routes are available for partially restoring the honeycomb structure and removing the functional groups. The resulted RGO can have great potential in hydrogel nanocomposites as its properties are close to that of the graphene, but its hydrophobicity is decreased. These characteristics make it the perfect candidate as filler in hydrogel nanocomposites. As mentioned previously, the electrical and thermal conductivity of GO is worse than those of graphene, but by applying reduction methods RGO can be manufactured, which makes it possible to regain some of the great physical characteristics.

Incorporation of graphene and graphene-derivates into gel matrix may result in nanocomposites with peculiar properties, owing to the platelet-like form of these nanoparticles. At first glance, these mixed systems may be compared to polymer-clay composites, in which the fillers have similar geometrical shape, and about which numerous studies have been revealed in the recent years. Four different structural arrangement can be distinguished [230] in nanoplatelets containing systems, depending on the distribution and concentration of the nanosheets as well as the degree of layer separation (Figure 7):
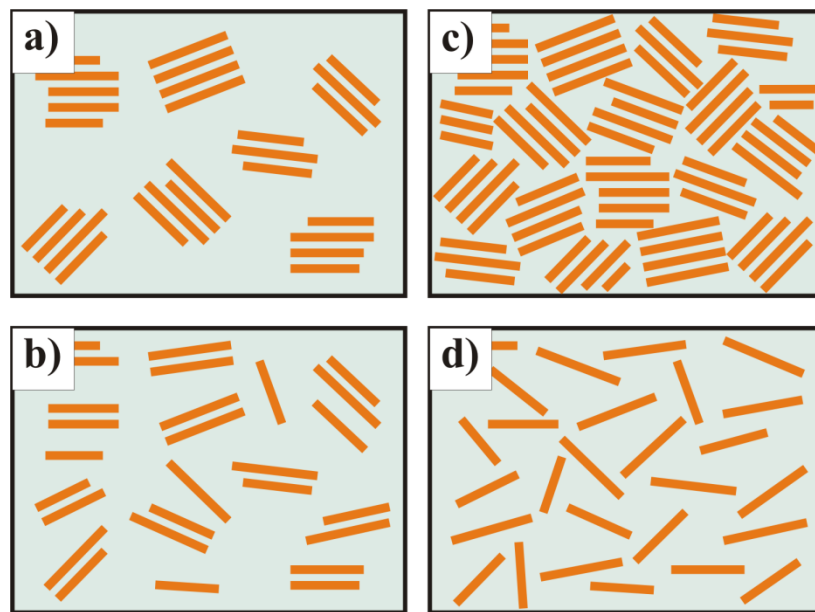
Figure 7. Polymer - nanoplatelet composites: a) conventional miscible, b) partially exfoliated and intercalated, c) intercalated in a crystallographically regular fashion and d) fully exfoliated and dispersed composites [230].

- Conventional miscible composite, where the platelets exist in their original aggregated state with no intercalation of polymer matrix between the layers. In this state, the particles can cause only marginal enhancement of properties to the matrix [230] (Figure 7a).
- Partially intercalated and exfoliated composite, where the exfoliated layers and intercalated clusters are randomly distributed in the matrix. These systems are very common and usually exhibit enhanced thermomechanical behaviour [230] (Figure 7b).
- Intercalated composite, where the polymer is intercalated between the layers in a crystallographically regular fashion [231,232]. The nanocomposite is interlaid by only a few molecular layers of polymer and the properties of the particle resemble those of the host [230] (Figure 7c).

- Exfoliated composite, where the individual layers are separated and dispersed in a continuous polymer matrix with average distances between layers depending on the nanoplatelet concentration. An exfoliated nanocomposite has properties governed primarily by the matrix, but generally, exfoliated nanocomposites exhibit better properties than intercalated ones of the same particle concentration [230] (Figure 7d).

The type of the formed structure depends on the quality of the dispersion of the nanoparticles. Molecular dynamics calculations indicate that graphene is more hydrophobic than CNT or fullerene [233]. For stable dispersions or pastes in water, it was found that an oxygen content of 13-16% by weight was needed [233]. Polymer content may also improve the stability of an aqueous CNP dispersion. The PNIPAM backbone, for example, was presumed to provide anchoring to the RGO surfaces and solubilisation and stabilization came from the solubility of hydrated substituted amide groups in the aqueous phase [233].

2.3.2.5. *Graphene derivates in PNIPAM*

Nowadays GO containing systems are in the focus of attention [101–105,229,234–236], but direct comparison of the results is difficult, as the preparation methods differ significantly. The majority of the studies have addressed PNIPAM systems of relatively high crosslink density ([cross-linker]/[monomer] > 0.1), and functionalized GO nanoparticles are often used to ensure first order bond formation [102,103]. Studies using as-prepared GO as a filler have also been made.

Ma et al. [104] found that the compressive strength of composite hydrogels, unexpectedly, decreases slightly with GO content at first, reaching a minimum at GO/NIPAM ratio around 1.5%, then it increases with GO loading and reaching a maximum at GO/NIPAM weight ratio of 5%. Thereafter the compressive strength decreases with further increase of GO content. At low content, GO sheets are individually intercalated in the hydrogels at intervals, leading to inhomogeneous network structure. The inhomogeneity of the network might be unfavourable to load transfer, leading to poor mechanical performance. With the increase of GO content, the distances between GO sheets become closer and closer since GO sheets are dispersed in the hydrogels more densely. When the amount of GO reaches the percolation threshold (around 5% weight ratio of GO to NIPAM), the edges of GO sheets will join together side by side, whereupon cross-linked PNIPAM and connected GO sheets might form an IPN network structure, resulting a more homogeneous network structure. Upon further increasing the GO content, some parts of the sheets will overlap with each other due to the

van der Waals force and the GO sheets will even stack together when the loading content is high enough, weakening the efficiency of the mechanical improvement. In case of the work of Ma and his coworkers [104], an important factor might be the applied cross-link density, since a rather densely cross-linked system (like theirs) might not be flexible enough to let the GO incorporate to the structure easily, therefore the reinforcing effect prevail only, when the continuous GO network has been formed. This can explain this rather high percolation threshold.

Zhu et al. [131] incorporated unmodified GO into PNIPAM matrix and found a completely reversible shrinkage upon light irradiation, which makes these materials potential candidates for microvalves. Li et al. [102] used functionalised GO in PNIPAM systems. They found that with the increasing GO-content the swelling degree decreased and the compressive strength increased. Upon GO-incorporation the VPTT increased as well. Lo and Jiang [103] used glycidyl-methacrylate functionalized GO, to prepare composites with strong interactions. They reported the decrease of the VPTT and increased NIR sensitivity of the system.

The above-mentioned results prove that the GO-incorporation can improve the properties of the polymer matrix, which suggests that RGO incorporation may be even more promising due to the enhanced properties of the nanoparticle itself. Few attempts have been already made to prepare various RGO containing composite materials [237–241]. In practice, though, the decreased hydrophilicity of RGO (with respect to GO) complicates the preparation of stable aqueous suspensions and consequently causing an inhomogeneous distribution of RGO in the composite [242]. Adhikari et al. [243] prepared RGO using Vitamin C and incorporated it to a polyamine matrix at 90 °C. If the synthesis procedure of the gel is not too sensitive for the environment, *in situ* reduction methods (i.e., reduction agent added to the initial precursor mixture) may be used [244–246]. However, *in situ* aggregation may cause nevertheless problems hindering the reinforcement effect of the nanoparticles. An effective way to make RGO containing gel composites is to reduce the already incorporated GO inside the gel matrix [217,247], however, the circumstances of the reduction (e.g., reducing agent, temperature) should be chosen with great care in order not to affect the physical/chemical properties of the gel. Wu et al. [247] reported that the reduction did not cause a drastic deterioration in the gel network and oriented structure. Kim et al. [217] found that the post-reduction strategy enables the reduction of GO components within the composite hydrogels without severe aggregation of the RGO components. The results of these studies showed that

the reduced hydrogels have high capacities for adsorption of rhodamine B and the degree of reduction could affect the adsorption capacity.

2.4. X-ray and neutron scattering

Scattering techniques are widely used for investigating structural and dynamic properties of complex systems.

2.4.1. *Small-angle scattering (SAS)*

Small-angle X-ray and neutron scattering (SAXS and SANS, respectively) are powerful methods for studying large-scale structures from few Angstroms up to thousands and even several tens of thousands of angstroms. SAS techniques can give information about the size, shape, and orientation of structures in a sample. The most important feature of these methods is their potential for analysing the inner structure of disordered systems, and frequently their application is a unique way to obtain direct structural information on systems with a random arrangement of density inhomogeneities in such large-scales. The techniques are based on the deflection of collimated radiation away from the straight trajectory after it interacts with structures that are much larger than the wavelength of the radiation. The deflection is small (0.1-10°) hence the name small-angle. The applied radiation (beam) can be, for example, X-rays or neutrons.

SAXS is sensitive to inhomogeneities of the electron density whereas SANS detects the variation of the so-called nuclear scattering length-density, but the underlying principles are identical for both techniques. Because SAS investigates distances that are large compared to interatomic distances, the medium is usually treated as a continuum and characterized by an average density. Consequently, the scattering is described as arising from "scattering objects" of some electron (or nuclear scattering length) density embedded in a medium of another density. Scattering objects may be isolated in the sample or distributed with some type of spatial correlations (Figure 8).

The scattered intensity $I(Q)$ is the Fourier transform of the correlation function of the density, which corresponds to the probability of finding a scatterer at a position (r) in the sample if another scatterer is located at position 0. Determination of physical quantities like molecular weight, particle volume, specific surface area, etc. is feasible only if $I(Q)$ is measured on an absolute scale. The experimental intensity is therefore normalized by a standard way to obtain the absolute intensity in absolute units (cm^{-1}).
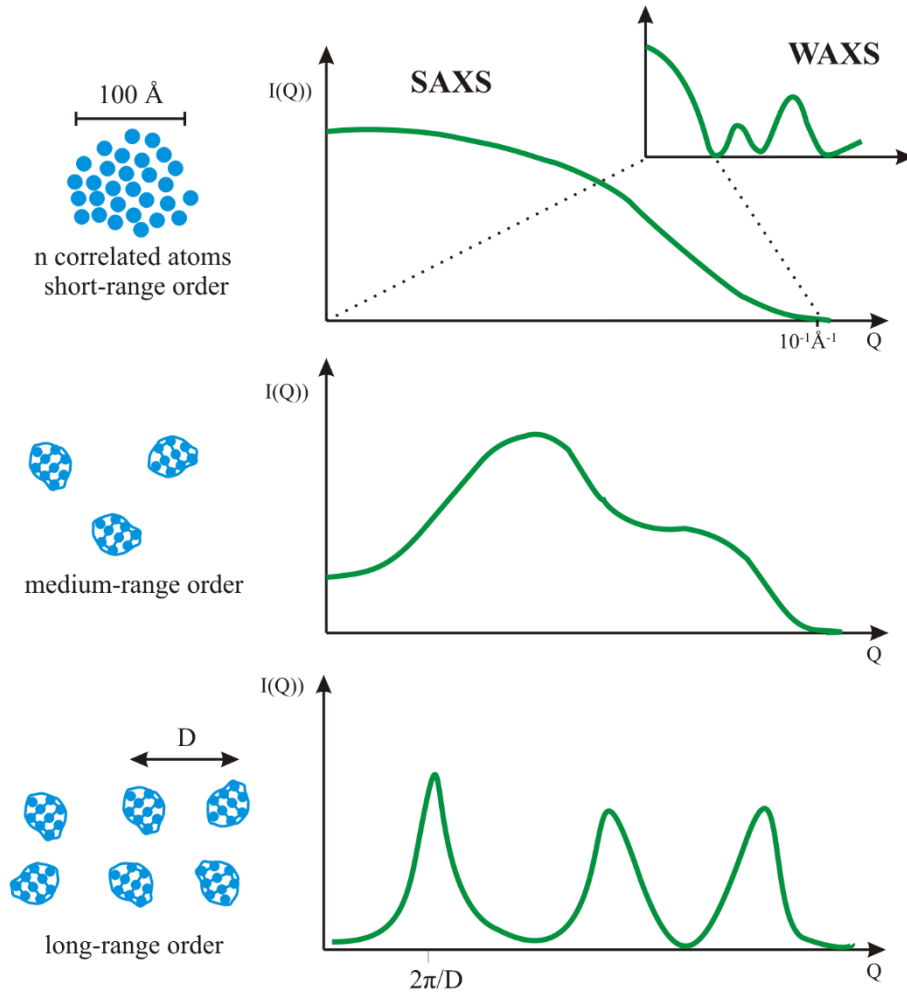
Figure 8. Schematic representation of the type of samples investigated by SAS [248].

Consider a neutron or the X-ray photon with an incident wave vector (k_{in}) that is scattered by a sample such that its outgoing wave vector is k_{out} (Figure 9). The neutron or the photon thus changes direction and loses (or gains) speed. In this scattering process, the neutron transfers momentum $\hbar Q$ and energy $\hbar\omega$ to the sample,

$$Q = k_{in} - k_{out} \tag{5}$$

$$\hbar\omega = E_{in} - E_{out} = \frac{\hbar^2}{2m}(k_{in}^2 - k_{out}^2) \tag{6}$$
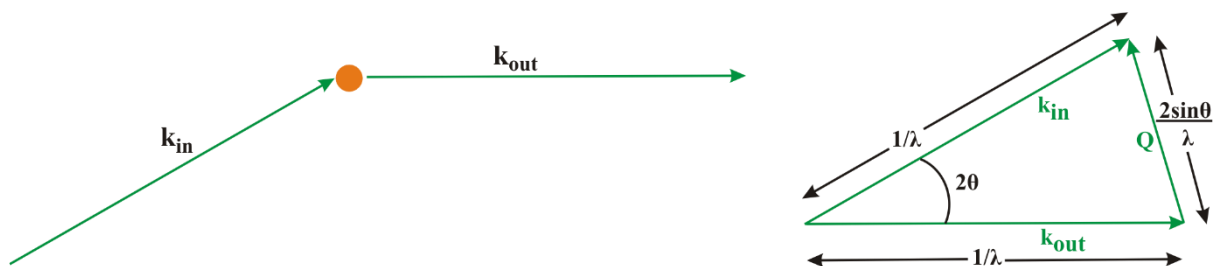
Figure 9. The graphical definition of the scattering wave vector [248].

32

A measurement made at a given Q_0 allows us to investigate the density fluctuations of the sample at a certain distance (D) scale ($D_0=2\pi/Q_0$). It is equivalent to observe the system through a D_0 diameter "window" in real space. To study objects much smaller or much larger than D_0, an other "window", therefore an other Q-value has to be chosen. Scattering signal is observed if the scattering density contrast inside the window is different from zero.

At the high Q domain (~0.1-1 Å^{-1}) the 'observation window' is very small: there is contrast only at the interface between the two media. This is the so-called Porod's region and gives information about surfaces. In the intermediate zone (~0.01-0.1 Å^{-1}) the 'window' is of the order of the elementary bricks in the system. This region provides information about the size, shape and internal structure of one particle. At the low q domain, the 'window' is very large; therefore the structural order can be obtained here.

In spite of the similarities of the two mentioned SAS techniques, some important differences have to be considered. Neutrons can penetrate matter far better than charged particles. (The penetration depth of neutrons in most materials is typically of the order of centimetres.) X-rays probe the electronic cloud surrounding the nucleus, while neutrons interact with atomic nuclei via very short range (~fm) forces (neutrons 'see' the positions of the nuclei) or with unpaired electrons via a magnetic dipole interaction [248]. Since the size of a nucleus is typically 100 000 times smaller than the distance between centres, neutrons can travel large distances through most materials without being scattered or absorbed. The available neutron beam flux is much lower than X-ray. This results a weak scattering signal, which is why neutron scattering is a signal limited technique.

The scattering of a neutron by a free nucleus can be described in terms of a cross section (σ), which is widely used in particle physics. It is measured in barns (1 barn = 10^{-28} m^2), that is equivalent to the effective area presented by the nucleus to the passing neutron. σ is given by $\sigma = 4\pi b^2$, as if the scattering length (b) were half the radius of the nucleus as seen by the neutron. b is not correlated with atomic number in any obvious systematic way (Figure 10) and varies even from isotope to isotope of the same element!

	H	B	C	O	Al	Si	P	Ti	Fe
X-Rays	1	3	4	8	13	14	15	22	26

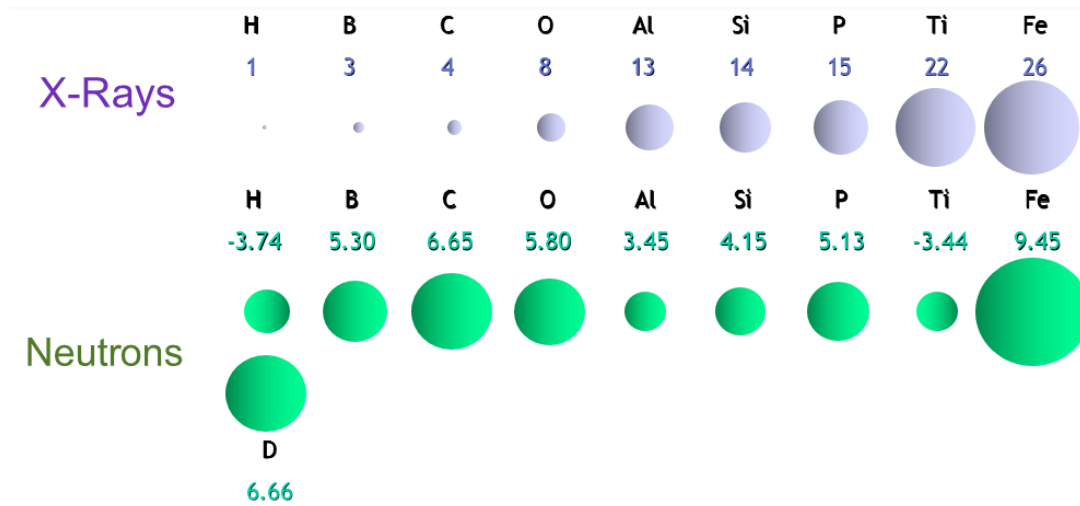|	H	B	C	O	Al	Si	P	Ti	Fe
Neutrons	-3.74	5.30	6.65	5.80	3.45	4.15	5.13	-3.44	9.45

D
6.66

Figure 10. X-ray and neutron scattering length values of different elements.

The neutron is scattered isotropically, with equal probability in any direction, because the nucleus essentially looks like a point scatterer. If the scattering occurs without any change in the probe's (neutron or photon) energy is said to be elastic. The opposite case is called inelastic scattering.

Even for a sample made up of a single isotope, not all of the scattering lengths of the nuclei will be equal, because the interaction between the neutron and the nucleus depends on the nuclear spin, and most isotopes have several nuclear spin states. Generally, there is no correlation between the spin of a nucleus and its position in a sample of matter, therefore the scattering lengths can be averaged without interfering with the thermodynamic average, but we have to distinguish between coherent and incoherent scattering.

In case of coherent scattering, neutron waves scattered from different nuclei interfere with each other. It depends on the distances between atoms and on Q. It provides information about the structure of a material.

On the other hand, in case of incoherent scattering, there is no interference between waves scattered by different nuclei. The intensities scattered from each nucleus just add up independently. The elastic incoherent scattering is the same in all directions; therefore it usually appears as an unwanted background.

2.4.2. Neutron spin-echo (NSE) spectroscopy

NSE spectroscopy [249] first introduced by Ferenc Mezei in 1972, is an inelastic neutron scattering technique that measures directly the intermediate scattering function $I(Q,t)$ as a function of wave vector (=momentum transfer) (Q) (Figure 9) and time (t). The NSE technique is well suited for measuring nanosecond time scale dynamics in soft matter

34

systems, with the highest energy resolution among all types of neutron spectrometers. It has proved to be an excellent tool for investigating dynamics in polymer gels [250–254].

The fundamental idea of NSE is to follow the energy change of each individual neutron in the scattering process. The neutron spin allows us to trace the neutron itself by using spin manipulations which can be shown to take place in a manner of conserving energy over the whole process, i.e., neutron energies are not perturbed by the measuring procedure [255]. The typical NSE setup can be seen in Figure 11.
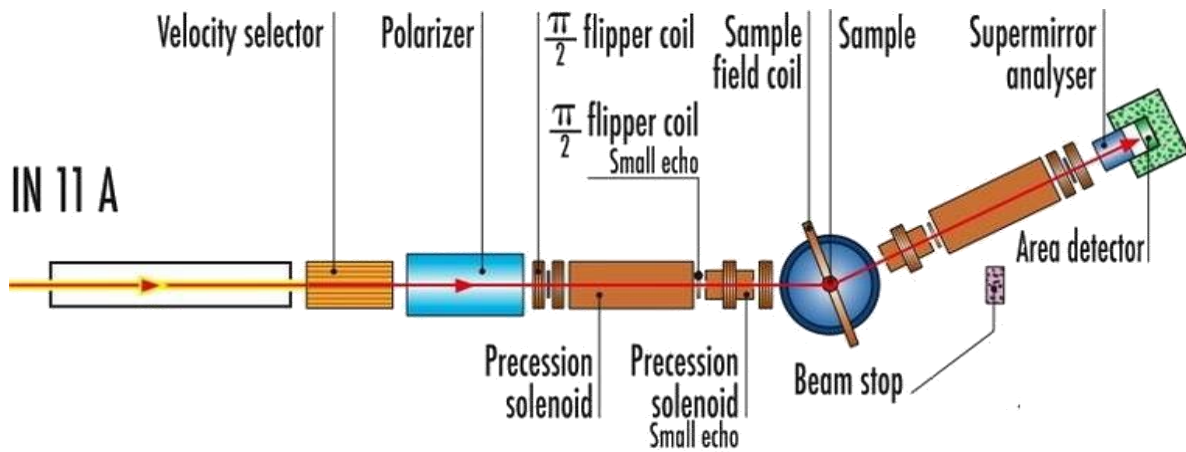
Figure 11. Setup of IN11A NSE Spectrometer at the Institut Laue-Langevin in Grenoble, France.

The NSE scan is performed in the time domain by varying magnetic field (*H*). The effect of field integral inhomogeneities can easily be taken into account by calibration measurements. The correction of the results involves a simple division instead of the deconvolution in usual neutron spectroscopy. This way, the resolution corrections can be performed exactly in NSE, independently of any model assumption on the scattering function and without using a fitting procedure [255]. The Fourier time (the studied time) range is proportional to, (therefore it can be tuned by) the cube of the used wavelength (*λ*) and the magnetic field integral. The longest achievable Fourier time is limited by field inhomogeneities. For a typical NSE instrument like IN11 or IN15 at Institut Laue-Langevin in Grenoble, the dynamical range [255] is in the order of $t_{max}/t_{min} \approx 100$.

If the field integrals in the two precession regions (before and after the sample) are equal, we have the echo condition. On one of the precession solenoids, we have a small number of extra turns wound, in which we can scan the phase current (Figure 12). This changes the symmetry of the field integrals, thus we can scan around the exact echo condition and measure the familiar echo group [255].

Figure 12. Typical 4 point echo measurement [255].

The information we are interested in the intermediate scattering function [*I(Q,t)*] is given by the echo amplitude. The most common way of determining it is the following: first, the scattered beam polarization is measured by counting for a given time spin up (π flipper on) and spin down (π f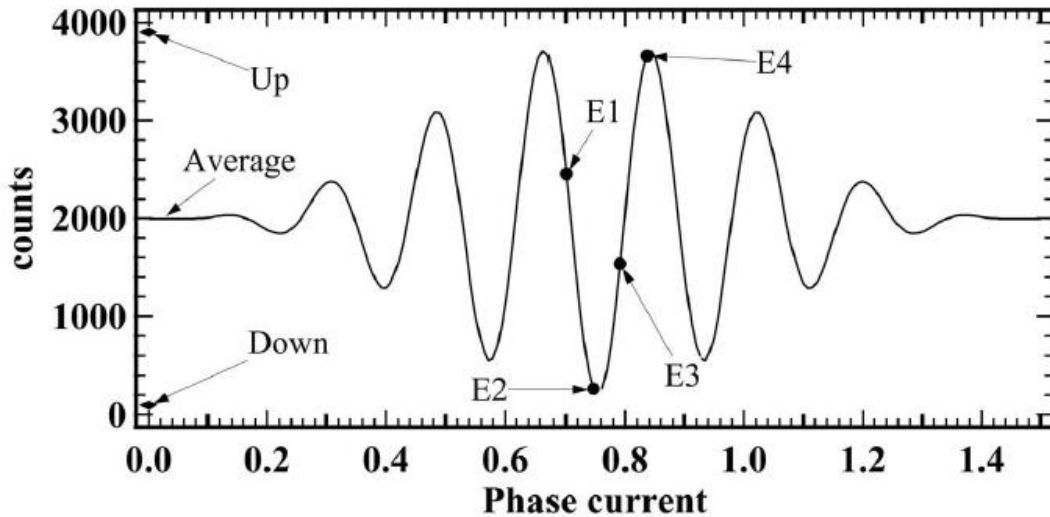lipper off). Once we measured the periodicity in terms of 'phase current' (e.g., on the straight beam), we can measure four points on the echo group placed by 90° steps around the centre: E1, E2, E3, and E4: Based on these values the average intensity, the echo amplitude and the phase can be determined. The final step is to divide echo amplitude with the initial polarization [(Up-Down)/2], thus giving *I(Q, t)* in a normalized form [255].

If the neutrons are scattered inelastically (or quasi elastically) from the sample, the amplitude of the echo is reduced. The reduction of the echo amplitude for different magnitudes of the magnetic field, neutron wavelengths, and scattering angles is, what is measured in an NSE experiment.

The scattering intensity at small angles (low *Q* values) usually is dominated by coherent scattering, which is favourable for the conventional NSE techniques. A typical sample should contain a majority of deuterated constituents (80-90%) allowing for a thickness between 2-4 mm. The resulting contrast of scattering length density compared to the hydrogenated objects to be observed gives rise to a considerable coherent SANS intensity. For larger momentum transfers ($Q > 0.2$–0.5 Å^{-1}) incoherent scattering becomes more and more important.

Considering the coherent scattering only, the NSE intensity *I(Q,t=0)* directly relates to the SANS intensity *I(Q)*. In a coarse analogy the SANS intensity corresponds to the scattering of

36

a frozen configuration of the scattering objects (flashlight photo) whereas after a time (t) some objects have moved, causing – on average – a more and more blurred configuration (scenery), the scattering of which corresponds to $I(Q,t)$. Since sharp edges and fine structures are blurred first, the high Q parts of $I(Q,t)$ decay faster. Confinements and permanent constraints cause some (average) structures to be persistent, the respective scattering intensity yields a t-independent constant level of $I(Q,t)$. For a more complicated composite system, the SANS intensity in a given Q-interval may stem from different structures with different relaxations [255].

3.   Aim of the PhD work

Responsive hydrogels have a wide range of potential applications (e.g., sensors, actuators, microfluidics, drug delivery vehicles, etc.), which can even be extended by composite preparation. CNPs are widely used for strengthening in polymer nanocomposites. In responsive systems, CNPs may act not only as reinforcing agents but due to their special structure, IR sensitivity, and tuneable conductivity; they can also provide new or modified sensitivity to these complex systems. As the nanoparticles may interact differently with the polymer matrix, the final properties of the composites are expected to be tuneable. This may provide a mean to further expand their applicability.

In the literature, PNIPAM based composite systems were investigated with a variety of cross-link densities and/or with different co-monomers, as well as with diverse synthesis conditions. Due to the huge variety of different parameters, it is not possible to directly evaluate the individual effects of incorporated nanoparticles.

The goal of my PhD work was to investigate systematically the effect of shape and surface chemistry of CNP incorporated to PNIPAM hydrogel systems. I studied two main groups: the rather hydrophobic, oxidized CNTs and the hydrophilic GO. Due to its high oxygen content, the physical properties of GO are worse than those of graphene. I investigated the effect of ascorbic acid reduction with mild conditions on the properties of the RGO and the RGO containing composites prepared by two different procedures.

The shape, size, surface chemistry, concentration and the preparation method, all can influence the final character of the resulted material. In my thesis, one of the aims was to identify the most important parameters with a significant effect on the structure and responsiveness of the composites and explore the relation between them. The composite materials were studied on both macroscopic and microscopic length scales to study their structure as well as their dynamic properties. I studied how the temperature gradient influences the kinetics of the phase transitions. Last, but not least, finding connections between the observations on the different length scales was also an important objective.

4. Materials and methods

4.1. Preparation

4.1.1. Nanoparticles

4.1.1.1. Graphene oxide

GO was obtained by the improved Hummers' method [214] from two natural graphite i) Graphite Tyn, GK, China ii) Madagascar - Chinese (CGO) and "Malagasy" graphene oxide (MGO). The GO suspension was purified and mildly exfoliated by centrifuging 5 times (7000 g) from 1 M HCl and 6–9 times (15100 g) from doubly distilled water, in order to remove unreacted graphite and inorganic salts. After the final washing and centrifugation step, a light brown suspension with a GO nanoparticle content of ~1 w/w% was obtained.

4.1.1.2. Reduced graphene oxide

To prepare RGO we modified the method of Fernandez-Merino et al. [222]. The dried MGO nanoparticles were suspended in ascorbic acid (AA) solution in the presence of NH_3 at 20 °C. In the reaction mixture the concentration of the MGO, AA, and NH_3 was 1 mg/ml; 20 mmol/l and 1.1 mol/l, respectively. The pH of the mixture was ~13-14. After 1 week the nanoparticles were purified by multiple washing and filtering steps. The resulted RGO was then dried and later stored in a desiccator at ambient temperature. For nanocomposite gel preparation RGO nanoparticles were re-suspended in water by ultrasonication (Branson B1200R-4) for 15 min with 40 kHz in sweep mode.

4.1.1.3. Carbon nanotubes

The dispersibility of the CNTs in aqueous medium was improved by oxidizing commercial MWCNT (external diameter: 10-20 nm; length: 10-30 μm according to the supplier) in concentrated HNO_3 (65%) (3 hours, 110 °C) in accordance with the procedure (including purification) of ref [148]. For nanocomposite gel preparation CNT nanoparticles were suspended in water by ultrasonication (Branson B1200R-4) for 4h with 40 kHz in sweep mode.

4.1.2. Gel synthesis

4.1.2.1. Pure PNIPAM gels

The PNIPAM polymer gel was synthesised from the *N*-isopropylacrylamide (NIPAM) monomer and the *N,N'*-methylenebisacrylamide (BA) cross-linker in an aqueous medium at

20 °C by free radical polymerization. The reaction was initiated by ammonium persulphate (APS) and *N,N,N',N'*-tetramethylethylenediamine (TEMED). The cross-link ratio (R) of the PNIPAM gel (1/150, 1/100 or 1/50) was determined as [BA]/[NIPAM]. For the synthesis of a pure PNIPAM gel with a cross-link ratio R=[BA]/[NIPAM] = 1/150, 18.75 ml of a 1 M aqueous solution of NIPAM and 1.225 ml of a 0.1 M solution of BA were mixed with 4.9 ml of water and 25 μl of TEMED. Finally, 1.25 ml of a 10 w/w% solution of APS was added to the mixture, and polymerization took place at 20 °C for 24 h. Films of thickness 2 and 4 mm and 10 x 10 mm isometric cylinders were prepared. All chemicals were used as received, except NIPAM, which was recrystallized from a toluene–hexane mixture. Doubly distilled water was used for the synthesis, purification, and measurements.

4.1.2.2.   *Composite gels*

To obtain CNT, GO and RGO containing nanocomposite gels (CNT@PNIPAM, GO@PNIPAM, and RGO@PNIPAM, respectively) the aqueous CNP suspension of the required concentration was mixed with the precursor solution. For the CNT and RGO containing composites, ultrasonication was used to ensure homogeneity of the dispersion. Gels with ≥20 mg GO/(g NIPAM) content (~ 2 weight% GO) were prepared by adding in succession solid NIPAM and BA to the GO suspension. The reaction medium was stirred in an ice-bath for 15 min after addition of each component. The total volume of the precursor solution, including the GO suspension, was kept constant by adding the appropriate complement of water. The precursor suspensions were polymerized and purified in the same way as the nanoparticle-free PNIPAM gel. No external field was applied. The films were stored in the swollen state for later use unless mentioned otherwise. The cross-link density of the polymer matrix was kept constant in all the composite systems: [BA]/[NIPAM]= 1/150. The CNT and GO loading was varied between 0 and 20 mg CNT/(g monomer) and 0 and 25 mg GO/(g monomer), respectively, whereas the highest reachable concentration of RGO was only 11 mg/(g monomer) due to its poor dispersibility. The CNP content is indicated at the beginning of the sample name.

The post-reduction treatment of GO@PNIPAM gels was made by soaking dried samples in the AA media (composition is identical as used for GO nanoparticle reduction, described above) for 1 week at 20 °C. The ratio of the solid (S) and liquid (L) phases was kept constant (S/L=0.012).

The abbreviation of the samples is summarised in Table 2.

Table 2. Nomenclature of the samples.

Sample name	R	CNP type	Reduction of GO
PNIPAM50	1/50	-	-
PNIPAM100	1/100	-	-
PNIPAM150	1/150	-	-
(PNIPAM150)R	1/150	-	-
GO@PNIPAM	1/150	GO	-
(GO@PNIPAM)R	1/150	RGO	within the gel
CNT@PNIPAM	1/150	CNT	-
RGO@PNIPAM	1/150	RGO	prior to synthesis

4.2. Characterization of the nanoparticles

For the microscopy observations, air dried CNPs were suspended in ethanol then dropped on the respective sample holder.

4.2.1. Atomic force microscopy (AFM)

For the AFM measurements, mica sample holders were used to study GO and RGO platelets. The AFM images were taken at the Toyo University Bio-Nano Research Center (Kawagoe, Japan) on an Oxford Instrument (ASYLUM Research Cypher) equipment, using AC mode, 4.88 Hz with a Micro Cantilever (Omega Lever OMCL-AC55TS-R3) needle.

4.2.2. Scanning electron microscopy (SEM)

For the SEM observation, the GO and RGO suspensions were dropped on a Si substrate. The SEM images were taken in a SEM (SU8030) (Hitachi) equipment.

4.2.3. High-resolution transmission electron microscopy (HRTEM)

The HRTEM images were taken in the Jülich Research Centre on a FEI Technai F20 equipment. Carbon films on copper grid sample holders were used on 120 kV. The ImageJ program was used to determine the inner and outer diameter and the number of walls of carbon nanotubes. 5-5 values on each tube were measured.

4.2.4. Thermal analysis

Thermal analysis (TA) was carried out on an STA6000 instrument (Perkin Elmer) in high-purity (99.9995%) nitrogen with the flow rate of 20 ml/min. Samples of about 10 mg were

heated from 30 to 300 °C with a scanning rate of 1.5 °C/min and then to 650 °C with a scanning rate of 10 °C/min in nitrogen atmosphere. The thermogravimetric (TG) curves were recorded.

4.2.5. X-ray photoelectron spectroscopy (XPS)

The surface chemical composition of the CNPs was determined by XPS, using an XR3E2 twin anode X-ray source (300W, VG Micro- tech) and a Clam2 hemispherical electron energy analyser. The base pressure of the analysis chamber was about $5 \cdot 10^{-6}$ Pa. Samples were analysed using an Mg Ka (1253.6 eV) anode, without monochromation. Wide scan spectra in the binding energy range 1100–0 eV were measured with an energy band-pass of 50 eV for all samples. High-resolution spectra of the C1s signals were recorded in 0.05 eV steps with energy band-pass 20 eV. The peak fitting procedure was performed with the CasaXPS program (Version 2.19).

4.3. Characterization of the gel systems

4.3.1. Equilibrium swelling degree (ESD)

Gel disks with a diameter of 7 mm were cut from the film and dried. 0.03 g dry gel was swollen in 2.5 ml water. The equilibrium swelling degree of the samples was measured using the dry gel disks. After 1 week in pure water at 20 °C the equilibrium swelling degree was determined as m/m_0, where m and m_0 are the mass of the swollen and dry samples, respectively. The equilibrium swelling degrees at various temperatures (T) were determined by gradually increasing the temperature of the water bath to 25, 30, 35, 40, 45 and 50 °C. 1 week of equilibration time was left between each step. The relative swelling degree was defined as the percentage ratio of the equilibrium swelling degree at temperature T with respect to that at 20 °C.

4.3.2. Mechanical tests

The elastic modulus was measured on fully swollen isometric (10×10 mm) gel cylinders using an INSTRON 5543 mechanical testing instrument at ambient temperature. Samples were compressed by 10% of their initial height in steps of 0.1 mm with a relaxation time of 4×2 s and a force threshold of 300 N. No barrel distortion was observed. The obtained data were evaluated following the method of Horkay and Zrínyi was used [256]. Repetitive uniaxial compression measurements on one cylinder of selected samples were performed, using the

same parameters as well. Between the measurements, 5 minutes of relaxation was provided to the samples in water.

Samples were also compressed until fracture in steps of 0.5 mm. The relaxation time and force threshold was the same as in the previous paragraph.

4.3.3. Thermal analysis

TA was carried out on the instrument described in 4.2.4. Prior to the experiments the gel samples were air-dried, ground in an agate mortar and stored in a desiccator over silica gel. Samples of about 10 mg were heated from 30 to 650 °C in nitrogen atmosphere with a scanning rate of 10 °C/min.

4.3.4. Solid-state magic angle spinning NMR spectroscopy

Solid-state magic angle spinning (MAS) spectra of samples were recorded on a Varian NMR system operating at a ^{1}H frequency of 400 MHz with a Chemagnetics 3.2 mm narrow-bore double resonance T3 probe. The spinning rate of the rotor was 8 kHz in all cases. For the one-dimensional ^{13}C cross-polarization magic angle (CP MAS) and direct excitation (DE) spectra SPINAL-64 decoupling with 83 kHz of strength was used. The CP MAS build-up curves were recorded in the range of 0-4 ms with a recycle delay of 5 s, which is 5 times larger than T_1H.

4.3.5. Differential scanning microcalorimetry (DSC)

Scanning microcalorimetry measurements were made on finely ground samples in a MicroDSCIII apparatus (SETARAM). About 10 mg of dry gel was placed in contact with 500 µL of Millipore water and kept at 20 °C for 2 h to allow the gels to equilibrate in the swollen state and to obtain a stable baseline. The samples were then heated to 50 °C with a scanning rate of 0.03 °C/min. The instrument software was used to determine the peak position, and calculate the specific enthalpy of the volume phase transition (ΔH_{VPT}).

4.3.6. Temperature jump induced shrinkage kinetics

The kinetics of the temperature responsivity of the samples were studied on gel disks of 10, 14 or 20 mm diameter and 2 mm of thickness (initial weight m_i). The samples were first swollen in water at 20±0.2 °C to reach equilibrium, then plunged into a water bath of 40±1 or 50±1 °C. The thermal shock induced shrinkage was followed by measuring regularly the weight $m(t)$ of the disks until they reached the equilibrium. Three parallel samples were

measured in each case. Results are reported as $100 \times m(t)/m_i$. An exponential function with one or two steps (Eq 7) was fitted.

$$\frac{m(t)}{m_i} \cdot 100 = \left(\frac{m_\infty}{m_i}\right) \cdot 100 + A_1 e^{-\left(\frac{t}{t_1}\right)^{p_1}} + A_2 e^{-\left(\frac{t}{t_2}\right)^{p_2}} \qquad (7)$$

where

m(t)	measured weight at time t [g]
m_i	weight of the initial gel fully swollen at 20 °C [g]
m_∞	weight of the deswollen gel at the end of the experiment [g]
t	time [min]
t_1, t_2	fitted time constants [min]
p_1, p_2	fitted exponents [-]
A_1, A_2	pre-exponential constants [-]

4.3.7. Small-angle X-ray scattering

SAXS data were collected at the European Synchrotron Radiation Facility (ESRF, Grenoble, France) on the beam-line ID02, with a wavelength of 12.46 keV and two samples-to-detector distances of 0.8 and 30.7 m giving an observed Q-range of 2×10^{-4} Å$^{-1} \leq Q \leq 0.8$ Å^{-1}.

2D data were radially averaged and standard reduction procedures (subtraction of empty cell and solvent contribution) were applied. For equilibrium measurements, the samples were swollen in water and then kept at the desired temperature (25, 40 or 50 °C) for 10 days prior to the experiment.

Primary data reduction was performed by SAXSUtilites developed by M. Sztucki [257], whereas the Irena package [258] was used to fit the obtained experimental curves.

4.3.8. Small-angle neutron scattering

SANS measurements [259] were performed on the D22 small-angle instrument at the Institut Laue-Langevin. The gels were swollen in D_2O in order to enhance the scattering contrast between the polymer and the matrix and to minimize the incoherent background scattering. Previous measurements [260] had shown that the swelling properties of the PNIPAM gel are not affected by the H_2O/D_2O isotopic substitution. For equilibrium measurements, the samples were swollen in heavy water and then kept at the desired temperature (25, 40 or 50 °C) for 10 days prior to the experiment. In addition, kinetic measurements have been performed as well on selected samples, when the temperature of the thermostatic bath of the SANS sample holder was rapidly increased from 25 °C to 50 °C. The VPT induced structural changes were followed by collecting the scattered signal in every 18 minutes overnight. The

incident neutron beam wavelength was 6 Å. Two sample-detector distances (17 m and 2 m) were used to cover a Q-range of $0.004 - 0.5$ Å^{-1}. Raw SANS data were corrected for the empty cell, dark counts, sample thickness and detector efficiency. The corrected scattering data were normalized by the incident beam flux to obtain the scattered intensity in absolute units. Data reduction was done with the GRASansP v.7.04 program. In case of nanocomposite samples, the weak signal from the corresponding nanoparticle suspensions has been subtracted in order to obtain the pure polymer signal.

4.3.9. NSE measurements

NSE measurements [261−264] were made on the IN11 and IN15 spectrometers at the Institut Laue-Langevin. For these experiments, gel films of 4 mm nominal thickness and 3 x 4 cm cross-section were used. Prior to the measurements, the gel samples were swollen in heavy water and then kept for at least 3 days at 10.0, 25.0 or 30.0 ± 0.1 °C. The swollen samples were placed in 5 mm thick sandwich-type cells with quartz windows. To exclude air and avoid undesirable deswelling, the remaining space in the sample holder was filled with D_2O. For high temperature (40.0 and 50.0 °C) measurements, the samples already swollen in D_2O below the VPTT were placed into a water bath of the desired temperature for 1 day or for ~42 days before the measurement.

On IN11 the IN11A high-resolution set-up was used. Measurements were performed in the transfer vector Q-range of 0.042 Å^{-1} $\leq Q \leq 0.209$ Å^{-1} and the incident wavelength of the neutron beam was 7.83 Å and 10 Å for IN11 and IN15, respectively. These parameters resulted a Fourier-time range of 0.1–30 ns on IN11 and 0.02–500 ns on IN15. The resolution functions of the instruments were determined for each experimental setup using the elastic scattering of graphite. The resulting intermediate scattering functions were corrected for the D_2O background dynamics.

5.   Results

5.1.   Characterisation of the CNPs

Before studying the characteristics of the synthesized nanocomposites, learning about the properties of the prepared nanoparticles is essential.

First of all, the morphology (structure, size, etc.) of the CNPs, needed to be studied. Neither the GO nor the RGO platelets have a regular shape, as can be seen in Figure 13. The lateral size of the GO platelets is in a rather wide 10-50 μm range, while the RGO particles are significantly smaller (~2-12 μm). The decrease in size was not the only change in structure upon reduction, as the number of wrinkles and folds also considerably increased.

a)

b)
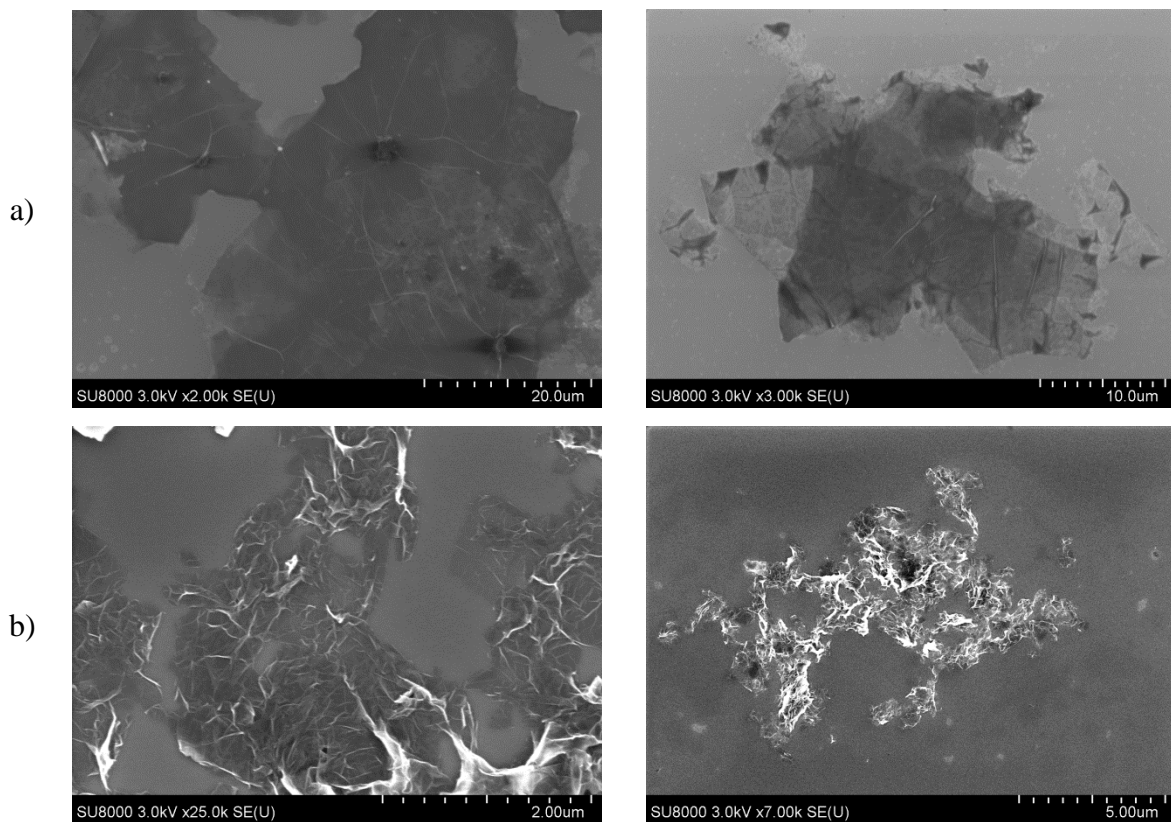
Figure 13. SEM images of a) GO and b) RGO platelets. The scales of the figures are different.

Besides their lateral sizes, the thickness of the platelets also influences strongly their properties. The thickness was studied by AFM (Figure 14). Due to the numerous wrinkles, more than one step can be seen on the AFM images. 1-5 nm thick layers were found in the case of GO, while lower values were expected for the RGO platelets because of the decreased amount of functional groups. Due to the wrinkles, however, even thicker layers were observed

by this method. For appropriate RGO observations, a different solvent should be used, which can prevent the folding.
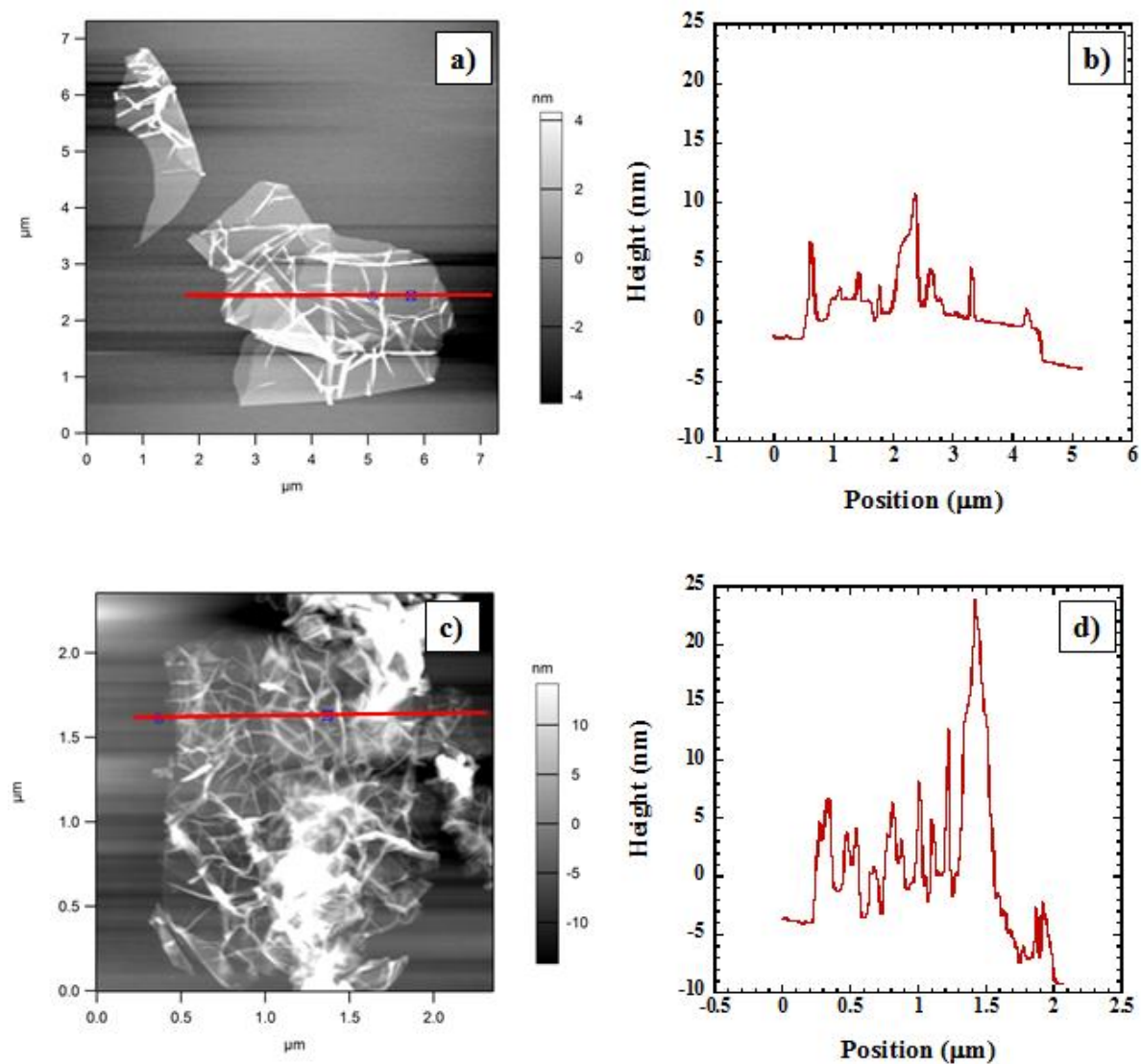
Figure 14. AFM images and the corresponding height values of a-b) GO and c-d) RGO platelets. The scales of the figures are different.

In case of the used CNTs, TEM analysis was used. In comparison to the values given by the supplier, the sizes of the nanotubes changed slightly upon the applied oxidation process. The inner and outer diameters were in the range of 1.8 – 6.2 and 9.2 – 19.7 nm, respectively. A great amount of structural defect was introduced into their structure (Figure 15). The eroded tubes structure occurred due to the introduction of the oxygen-containing functional groups.
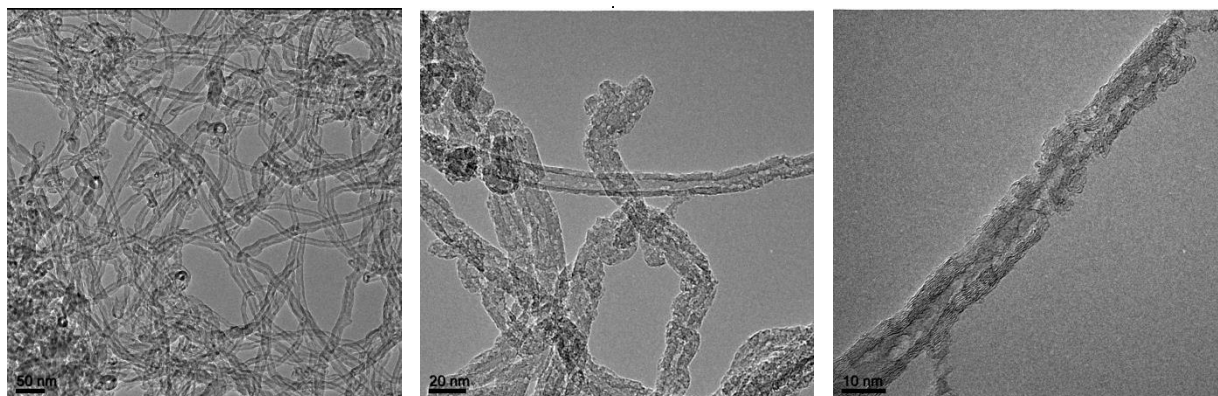
Figure 15. TEM images of the studied, oxidized CNT. The scales of the figures are different.

To characterize the functional groups present on the CNPs, X-ray photoelectron spectroscopy (XPS) was used. The C/O atomic ratio are shown in Table 3.

Table 3. C/O ratios determined by XPS of the studied CNPs.

CNP	CGO	MGO	RGO	CNT
C/O ratio	2.2	1.8	3.6	11.2

The surface chemistry of the GO samples prepared from two different natural graphites was similar. The decrease in the oxygen-content upon the reduction process can be clearly seen for the RGO, while the applied oxidation on the CNT resulted in only a mildly oxidised surface. The prepared CNPs have different parameters; therefore they can be used for studying the effect of the shape and surface chemistry on the composite samples.

5.2. Macroscopic characterization

5.2.1. Visual observations

During my work, pure hydrogels and composite systems with various CNP/polymer ratios were studied systematically. The first, straightforward comparison of the systems could be done by the naked eye (Figure 16).

The pure polymer matrix in the studied cross-link ratio range swollen in water was almost transparent. No difference was visible between the pure gels by the naked eye. Due to the high water content, the refractive index of the swollen gels was close to that of the pure water. The reduction process did not influence its appearance either.
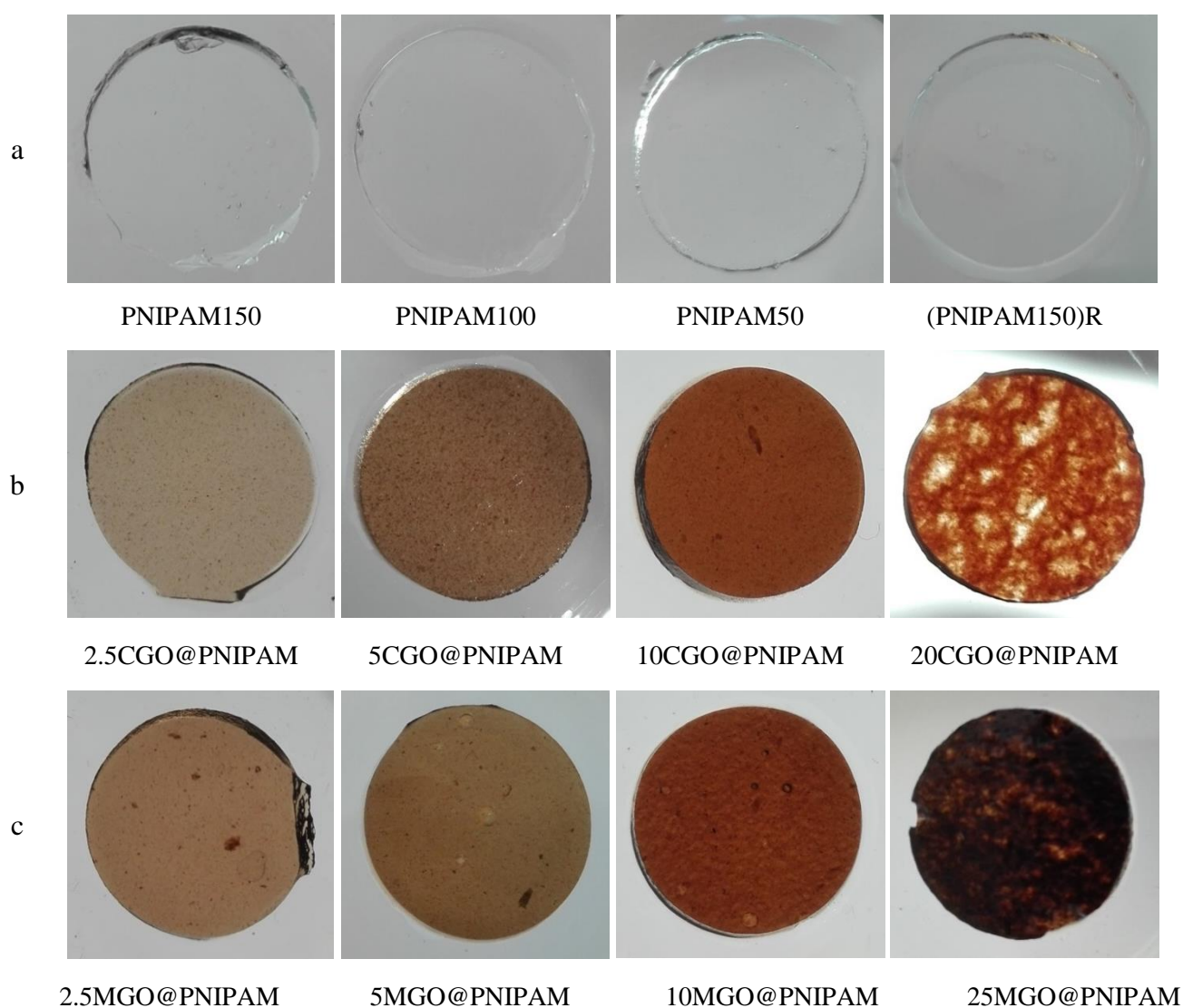

Figure 16. Images of the a) pure gel systems, b) CGO@PNIPAM composite family and c) MGO@PNIPAM composite family.

d

(2.5GO@PNIPAM)R   (5GO@PNIPAM)R   (10GO@PNIPAM)R   (25GO@PNIPAM)R

e

3RGO@PNIPAM   11RGO@PNIPAM

f

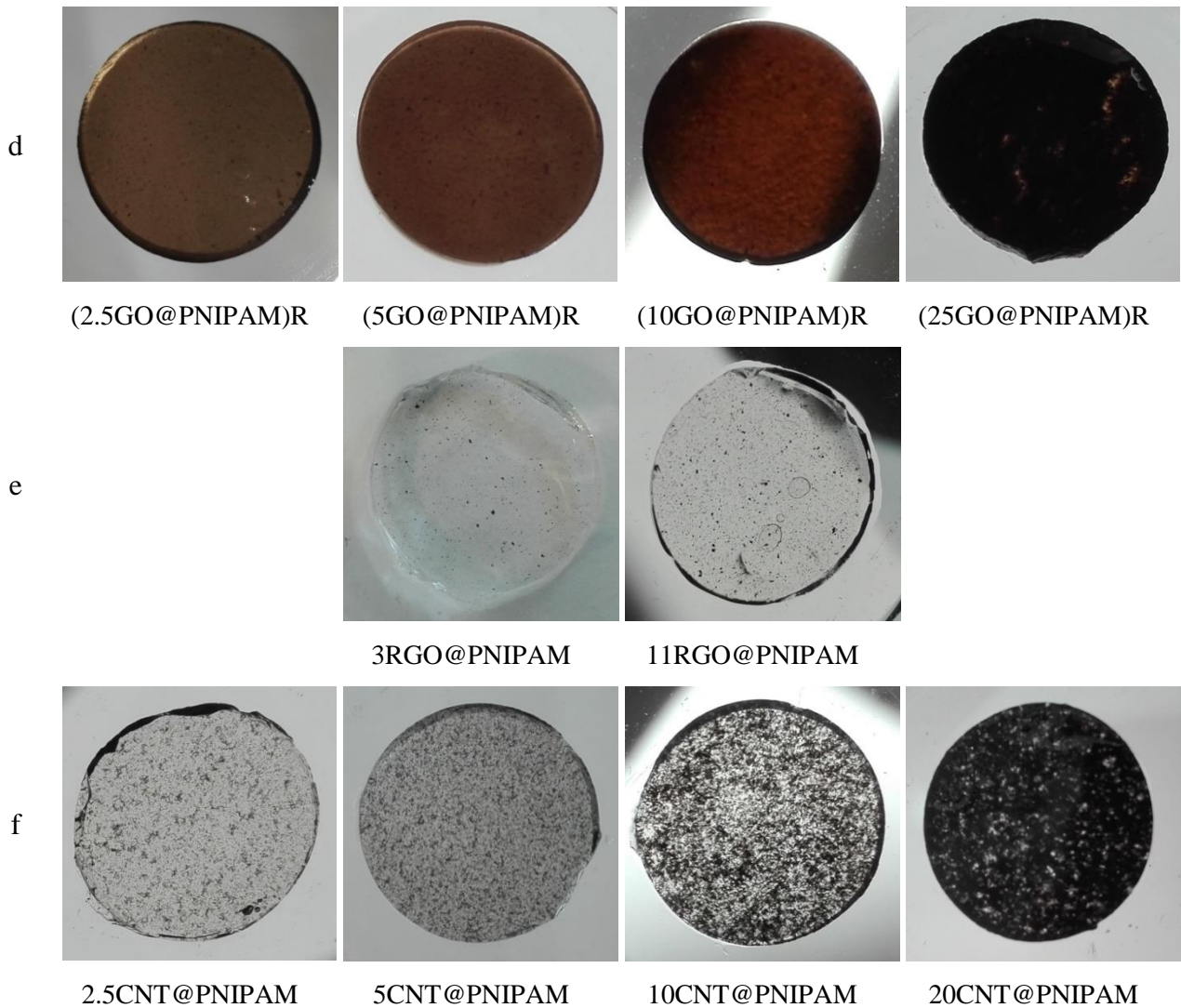2.5CNT@PNIPAM   5CNT@PNIPAM   10CNT@PNIPAM   20CNT@PNIPAM

Figure 16. Images of the d) (GO@PNIPAM)R composite family, e) RGO@PNIPAM composite family and f) CNT@PNIPAM composite family.

Nanoparticle incorporation changed the colour of the systems. GO containing gels were brown, whereas the CNT and RGO content provided grey or even black colour. The colour was getting deeper with the increasing amount of CNP for all types of systems. In case of GO containing composites and the post-reduced systems, at low concentration, a rather homogeneous CNP-distribution could be observed, aggregation occurs only at high concentrations. On the contrary, in the RGO and CNT incorporated gels, aggregates could be seen already at low concentrations, resulting in an inhomogeneous CNP distribution in the whole concentration range.

5.2.2. *Equilibrium swelling and mechanical properties*

The influence of the composition on the ESD in pure water at 20 °C and on the elastic modulus of the gels is shown in Figure 17.
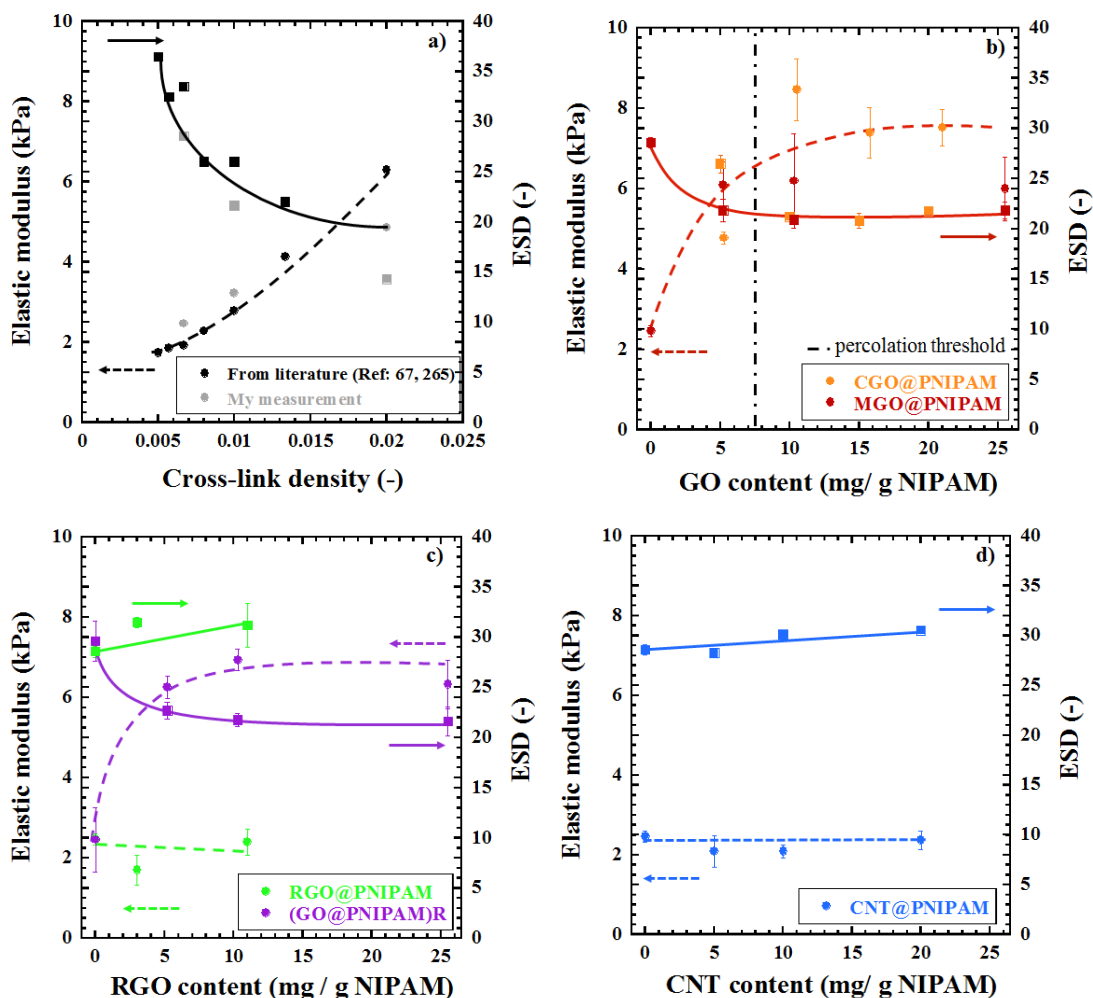
Figure 17. Elastic moduli (squares) and ESD values (circles) at 20 °C of the studied gel system: a) pure PNIPAM systems with different cross-link density values b-d) GO, RGO and CNT containing composites, respectively. The solid and dashed lines are guides for the eye.

Figure 17a shows that the increasing cross-link density resulted a more rigid gel system: the elastic modulus increased, while the ESD decreased. Our results were in accordance with data from the literature [67,265]. The direction of the changes was the same in the GO containing samples, however, the shapes of the response curves were different. Increasing CGO and MGO content drastically decreased the ESD and increased the elastic modulus (Figure 17b). Contrary to the pure gel systems, the changes were not monotonous, a plateau was observed in both quantities. These differences suggest that the role of the GO was more complex than a simple chemical cross-linker in the polymer matrix.

Li and co-workers reported an increase in modulus when chemically modified GO is used as a co-monomer [102]. This preparation method suggested the formation of covalent bonds. On the other hand, in gels with higher cross-link density (molar ratio of [BA]/[NIPAM] = 1/35 instead of 1/150), the addition of unmodified GO to the precursor solution resulted in an

opposite tendency in both the swelling ratio and elastic modulus [103]. It suggests that the properties of the original polymer matrix have a great impact on the concentration dependence of the reinforcing effect.

The two types of GO@PNIPAM systems showed similar results. The preparation route of the CGO and MGO containing composites were the same, therefore the difference in the numerical values comes from the slightly different properties of the CGO and MGO. According to the literature, the GO-properties depend strongly on the initial graphite [216], which would explain even higher differences. In the next chapters, I am not going to make any distinction between the two types of GO.

According to the literature GO platelets in aqueous phase above a certain concentration can form a continuous network [266,267]. In case of the composite systems, at the percolation threshold, the GO particles form an interpenetrating network inside the matrix. Figure 17b suggests that the percolation threshold of the GO occurs between a concentration of 5 and 10 mg GO/g dry NIPAM, i.e., roughly 0.25 - 0.5 mg/g of the swollen gel. These values correspond to ~ 0.5-1 weight% of GO content of the composite systems, which is in accordance with the values from the literature (percolation threshold in the range of 0.1 – 5 weight% [76,104,190–199]).

After the post-reduction treatment of the GO@PNIPAM systems, the concentration effect trends remained almost unaffected (Figure 17c). This can be explained by either the reinforcement is due to a simple mechanical effect (where surface chemistry and chemical interactions play no significant role); or, if there are chemical interactions between the GO and the polymer matrix, those interactions that determine the mechanical properties are unaffected by the applied treatment. On the contrary to GO, when RGO (Figure 17c) or CNT (Figure 17d) nanoparticles are incorporated directly into the pure PNIPAM gel the mechanical and swelling properties of the nanocomposites remained practically unchanged. As these nanoparticles are less hydrophilic, they tend to form aggregates in aqueous media, their effective concentration within the gel matrix was much lower than the theoretical one. In addition to that, as seen in Figure 16, they distributed inhomogenously, which can explain their very different behaviour.

During the elastic modulus measurements, we noticed that the repetitive compression of the same sample may have a clear impact on the measured elastic modulus on some of the samples while it did not cause clearly noticeable deformation of the compressed cylinders. From a future application point of view, the change in the mechanical properties upon

repetitive usage might be crucial; this is why we decided to perform a detailed study on the effect of repetitive compression. As shown in Figure 18 and Table 4, the elastic modulus of the pure PNIPAM and the RGO- or CNT-incorporated systems remained practically unaffected after 40-times repetitive compression: the difference between the first and last measurements was smaller than the standard deviation of the measurements (± 0.4). This means that the gel system was able to relax fully and reversibly. The behaviour of RGO- or CNT containing samples was not surprising though if we take into account that the incorporation of these nanoparticles did not affect significantly the obtained swelling and elastic properties of the composites either.
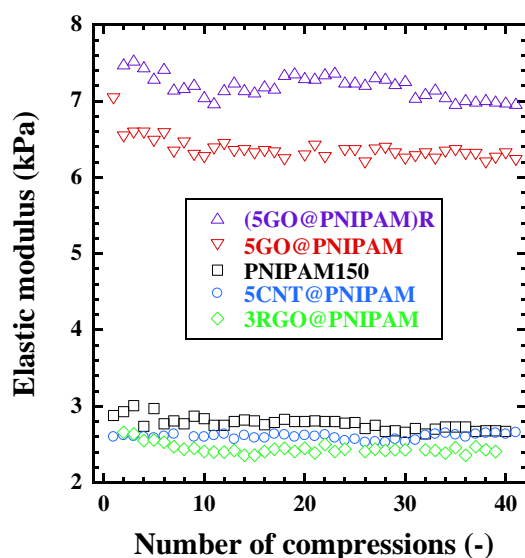

Figure 18. Results of repetitive uniaxial mechanical tests.

On the contrary, GO and post-reduced GO containing composites showed a non-reversible-behaviour upon uniaxial compression. The decrease in the elastic modulus after 40-times compression exceeded the statistical error (Table 4), which suggests that there is some sort of internal structural change upon compression or the reorganisation is much slower than the waiting time (maximum 1 day) between the modulus measurements. This phenomenon occurred only in case of incorporated, non-aggregated nanoplatelets, which might suggest, that the shape of the incorporated CNPs is related to the issue. The nanotube aggregates did not show a significant change, therefore, the experienced structural change might be, for example, orientation or even restacking of the nanoplatelets. Regardless of the shape of the

53

Table 4. Difference between the first and the 40th measured modulus values for the selected samples.

Sample	Modulus difference (kPa)
PNIPAM150	0.2
5CNT@PNIPAM	0.1
3RGO@PNIPAM	0.2
5GO@PNIPAM	0.8
(5GO@PNIPAM)R	0.5

CNPs, there is a second, important factor. The modulus of these gels was higher than that of the pure polymer or the RGO and CNT incorporated samples, which means, that even for the 10% of compression required relatively high forces. The irreversible deformation might have been caused because of the used higher forces. However, this option can be excluded, because, at the small deformation region (strain < 0.1), the difference between the applied stresses to the different samples are not outstanding (Figure 19).

Beside the moderate compressions applied for the elastic modulus measurements, the total stress-strain curves were measured (Figure 19a,c,e,g). The increase of the cross-link density did not influence significantly the strain what the gel can withstand, but the fracture strength increased slightly with it (Figure 19a,b). Incorporation of the GO substantially improved the compressive strength of the gels but showed no dependence on the concentration (Figure 19c,d). The withstood strain values varied in a certain region, but the correlation between the concentration and resulted value was unclear. The post-reduction process did not influence significantly the strain values; however, the fracture strength (especially, beyond the percolation threshold) was diminished (Figure 19e,f). Important to note, that even after the reduction treatment the strength of the (GO@PNIPAM)R samples was two times higher than that of the pure gel. This change in the fracture strength was the first observed negative effect of the reduction method. This can be explained as upon the functional group removal, there was a change in the interactions in the matrix; therefore the stress propagation was less efficient. Therefore, it was possible to perform the reduction process inside the gel matrix, while keeping the advantageous properties of the initial GO@PNIPAM composites.
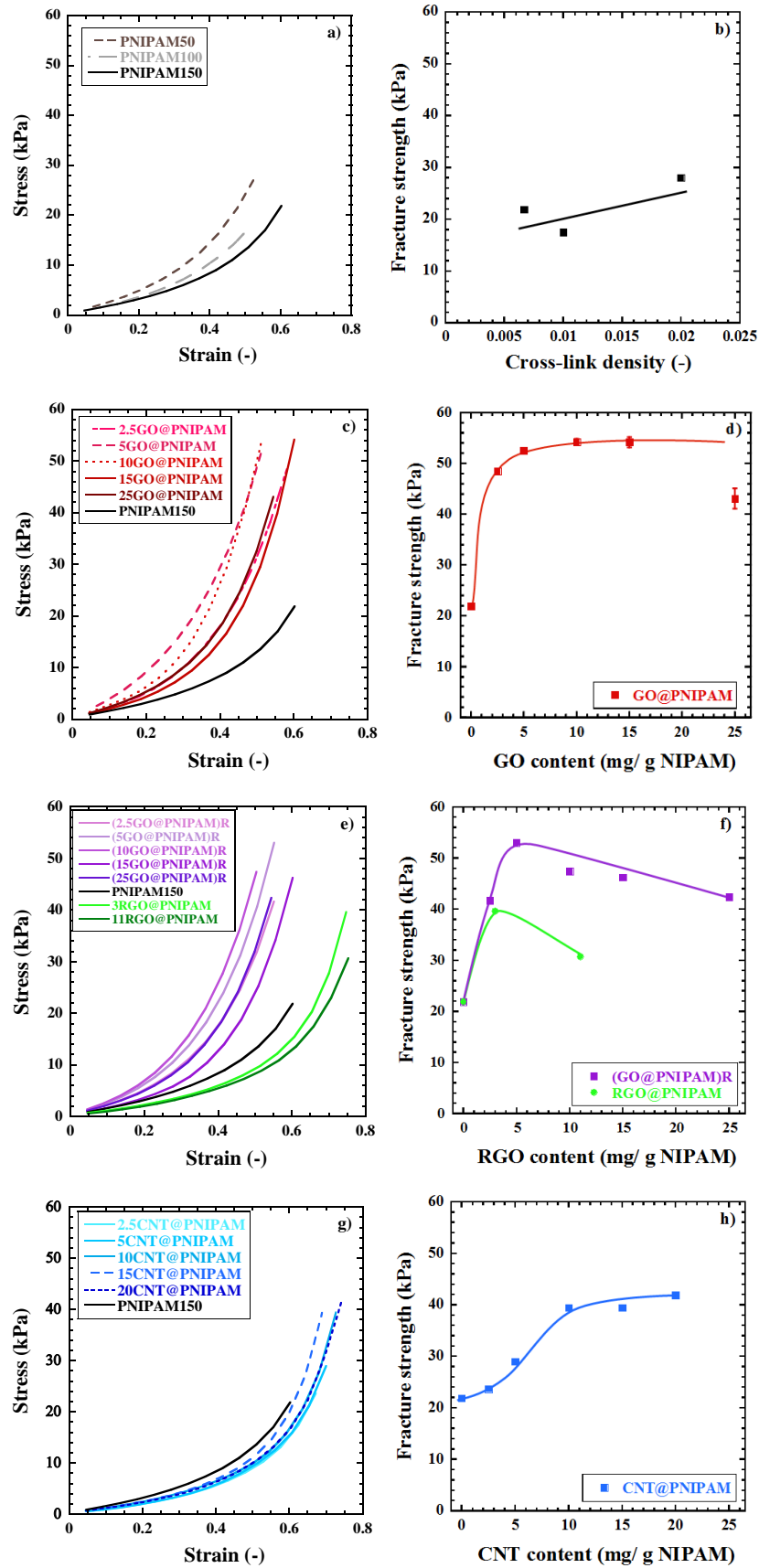
Figure 19. Stress-strain curves and fracture strength values of different gel systems: a-b) pure PNIPAM systems with different cross-link density values c-h) GO, RGO and CNT containing composites, respectively, where the solid lines are guides for the eye.

55

GO reduced prior to the gel synthesis did not modify the elastic modulus values of the formed composites, but improved the withstood strain and the fracture strength as well. The effect of the concentration, on the other hand, seemed to be inversely proportional, which might be caused by the inhomogeneity of the RGO. However, clear concentration effect could not be concluded owing to the small number of points investigated. CNT@PNIPAM gels (Figure 19g,h) tolerated also greater deformation before they break and withstood higher stress than the pure PNIPAM, but the increment was less pronounced than in case of the GO platelets.

5.3. Structural comparison on microscale

5.3.1. Below VPTT

To explore the structural differences caused by incorporating CNP into the polymer matrix SAXS and SANS measurements were performed. The neutron scattering length density value of the PNIPAM matrix was significantly different from that of the swelling medium, namely D_2O (Table 5), resulting in a strong scattering signal.

Table 5. Neutron scattering length densities of the components of the gels.

Component	Composition	Neutron scattering length density $(10^{-6}/Å^2)$
PNIPAM	$(C_6H_{11}NO)_m$	0.825
GO	$C_{65}O_{35}$*	5.993
CNT	$C_{92}O_8$*	6.750
D_2O	D_2O	6.364

* CNP compositions were estimated by XPS

In the composite samples, which were ternary systems, the signal was still dominated by the PNIPAM signal. As seen in Table 5 the neutron scattering contrast between the CNPs and D_2O was weak, and the overall signal, therefore, originated almost exclusively from the polymer, even in the composite systems. The corrected SANS response curves obtained at 25 °C (typical examples are shown in Figure 20) were fitted to the modified Ornstein-Zernike (OZ) expression [57,268,269] in the range of $Q > 0.01$ Å$^{-1.}$

$$I(Q) = \frac{I(0)}{1+(Q\xi)^m} + B \qquad (8)$$

where *I(0)* and *B* are *Q*-independent constants, ξ is the static polymer–polymer correlation length and *m* is the Porod exponent. This empirical model is widely used for highly correlated systems like polymer solutions and gels.

The deviation in the $Q < 0.01$ Å^{-1} region stemmed from the well-known concentration inhomogeneities due to cross-linking in gel networks [270].
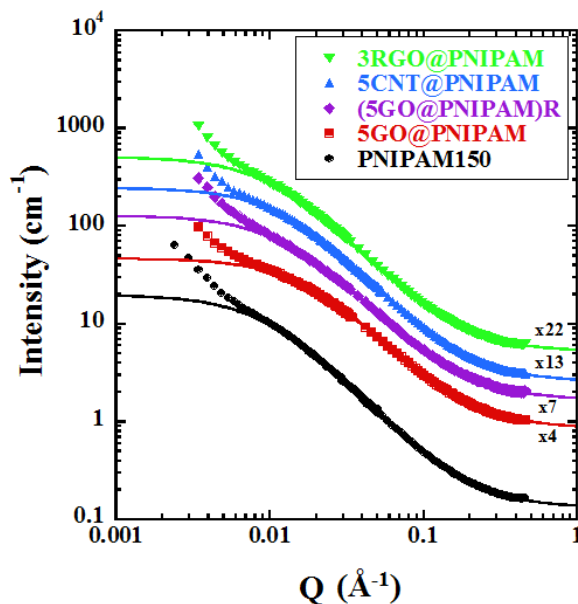
Figure 20. SANS response curves of selected samples at 25 °C after subtraction of the corresponding backgrounds with the OZ-fits.
The curves are shifted vertically for clarity. The used factors are shown on the figure.

From the OZ model, the static correlation length could be determined (ξ). The increase in the cross-link density resulted in a reduction in ξ (Figure 21a), which is in agreement with the literature [271]. In chemical gels, ξ is usually interpreted as the size of cross-linked nods and is inversely proportional to the cross-link density. Concerning the composites, it is easy to see that both the type and the concentration of the CNPs have pronounced effect on the correlation length of the polymer matrix. Even the smallest amount of CNP present in the nanocomposites results in a significant decrease of ξ. In case of GO@PNIPAM systems (Figure 21b), a U-shaped curve was observed: a drop of ξ was followed by an increase upon GO concentration increment. Nevertheless, even at the highest GO concentration ξ remained significantly smaller than in the pure PNIPAM. The increasing trend of ξ upon increasing GO loading may indicate that at higher concentrations the GO nanoparticles come into contact with each other and/or stick together, resulting in a smaller effective concentration, which was in agreement with the percolation theory as well. In case

57

of the continuous GO network, less surface was available for forming interactions with the polymer chains, so the formed structure in the high amount of GO containing systems was looser, which explains the higher ξ value. On the other hand, the total amount of hypernodes might not decrease in the whole systems, since the mechanical and swelling properties showed no change at the same concentration regime. Presumably, the maximum number of available interactions was reached around the percolation threshold.
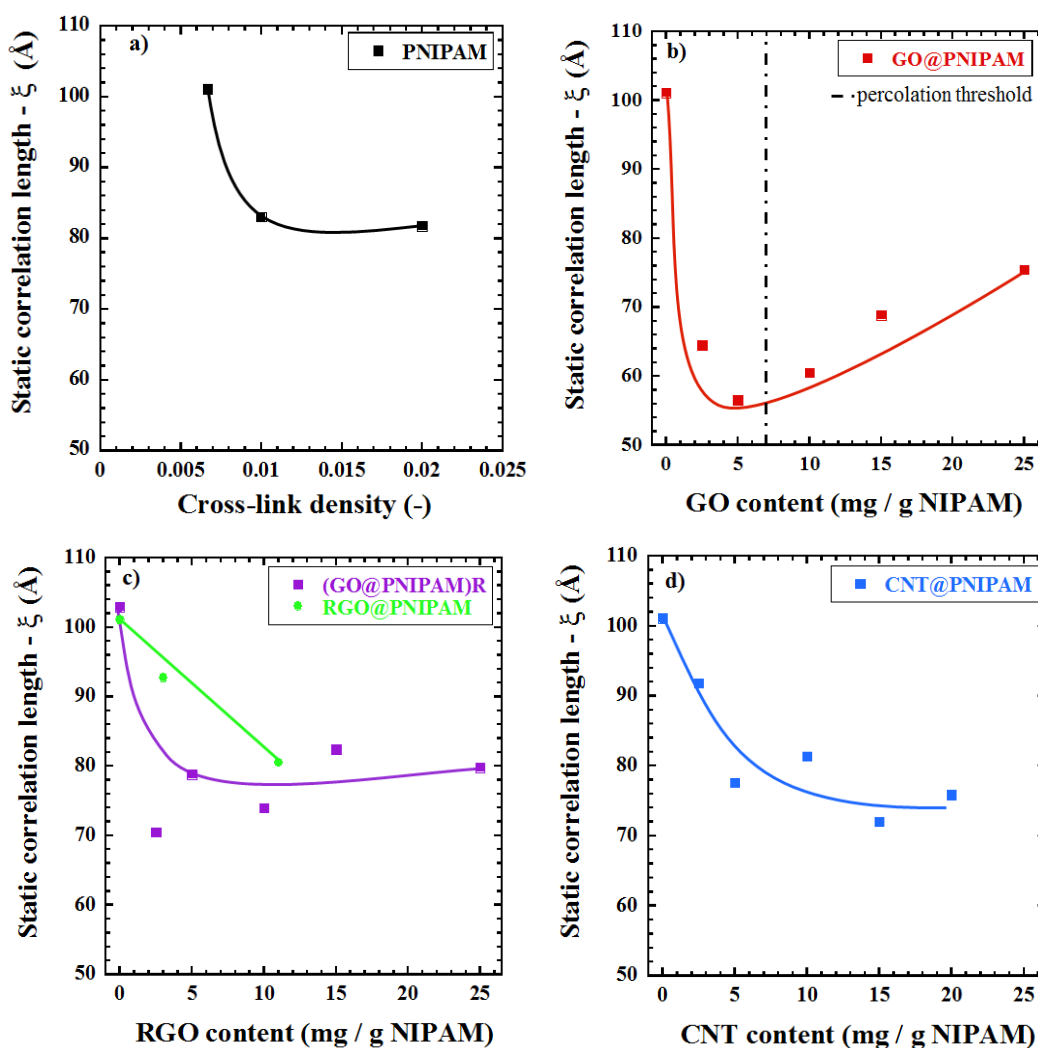
Figure 21. Static correlation length values of the different samples determined by the OZ model, fitted on the SANS curves: a) pure PNIPAM systems with different cross-link density values b-d) GO, RGO and CNT containing composites, respectively. The solid lines are guides for the eye.

After the post-reduction treatment ξ increased at all CNP concentrations in comparison to the original GO@PNIPAM systems (Figure 21c). On the other hand, no significant effect was observed in the pure CNP-free gel after the same treatment (PNIPAM150 and (PNIPAM150)R, 101.1 and 102.9 Å, respectively). The latter suggests that the pure polymer

matrix was not affected by the reduction procedure, i.e., the chemical cross-links were untouched. It was in accordance with the elastic modulus and swelling degree observations (Figure 17). However, the change in ξ in the nanocomposite systems after the post-reduction treatment indicated that the hypernode structure of GO@PNIPAM system was partially disrupted, possibly by breaking bonds between the nanoparticles and the polymer matrix. Interesting to note, that this observation was partially in contradiction with the mechanical and swelling properties, where the reduction treatment influenced only the fracture strength.

On the contrary to the previously described two cases, when RGO or CNT was directly incorporated into the polymer matrix ξ continuously decreased upon concentration increase. The structure modification effect at low concentrations was much less pronounced than in the other cases (Table 6), which was possibly related to aggregation of RGO and CNT even at low concentrations.

Table 6. Static correlation length values of pure PNIPAM150 and composites with low CNP-content at 25 °C.

Sample	Static correlation length (Å)
PNIPAM150	101.1
2.5GO@PNIPAM	64.5
(2.5GO@PNIPAM)R	70.5
3RGO@PNIPAM	92.7
2.5CNT@PNIPAM	91.8

SAXS is a complementary technique to SANS since in case of SANS the nanoparticles are practically invisible and the scattering of the polymer matrix dominates the signal, whereas with SAXS, the scattering signal of the polymer is relatively weak, therefore we can get structural information about the incorporated CNPs. This was confirmed by that the absolute intensity of the composites measured by SANS was very close to that of the pure gel, however, it was significantly higher by SAXS (Figure 22).

To get the contribution of the CNPs, the corresponding scattered SANS and SAXS signals were compared. Due to contrast differences in the techniques and the incoherent scattering of the SANS, the SANS signal was shifted to the SAXS curves. The contrast differences of the polymer matrix and the nanoparticles were calculated and in the overlapping Q-region, the

proportional part of the SANS curves was subtracted from the SAXS signal. The difference of the signals corresponded to the nanoparticles.
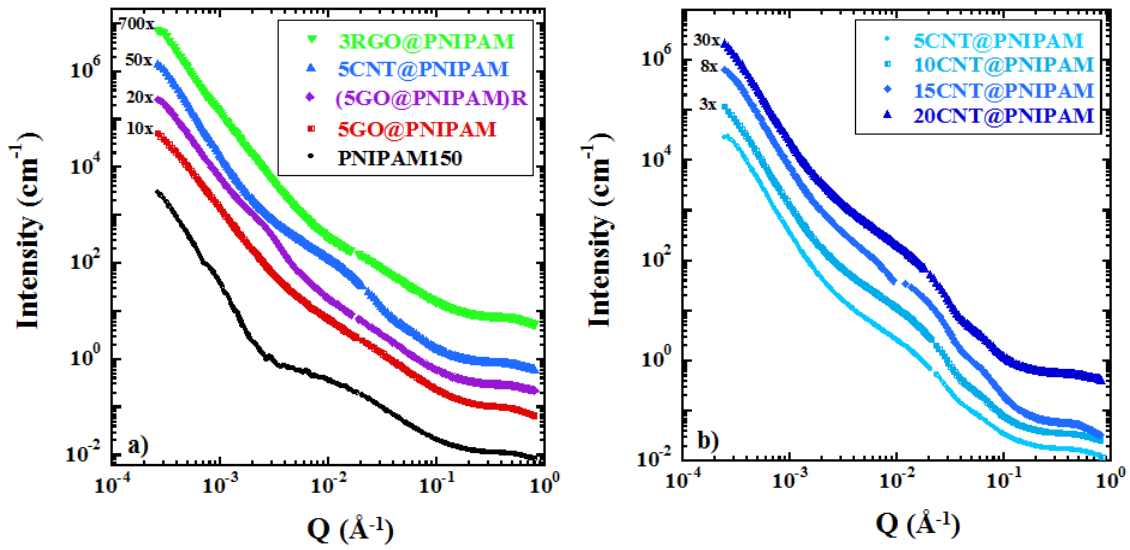

Figure 22. a) SAXS response curves of selected samples and b) CNT@PNIPAM composites at 25 °C after subtraction of the water backgrounds.
The curves are shifted vertically for clarity. The used factors are shown in the figures.

Figure 23 shows the scattering intensity of selected samples measured by SAXS (black symbols) together with the SANS signal of the same sample (red symbols). In the figure, the SANS response was multiplied by a scaling factor and a constant has been subtracted such that at high Q the two data sets coincide. In case of the pure gel system, a fairly wide overlapping region was found, the slight shortfall in the SANS intensity visible at low Q in Figure 23a was an artefact of the background subtraction and could be corrected manually.

In case of the composite samples, a greater difference was obtained between the SANS and SAXS responses, which originated from the extra scattering of the CNPs visible only by SAXS (Figure 23b,c).

The thickness of a single GO platelet was ~ 10 Å, while the lateral dimensions were in a micrometre size range (see Chapter 5.1.). These values correspond to a scattering vector of $Q=2\pi/D=0.6$ and ~ 6.3×10^{-5} Å^{-1}, respectively. These values are outside of the investigated Q regime, therefore we could not see them. The stacking of the platelets is an ordered structure (which usually has a characteristic distance of 10 Å, with the corresponding Q value
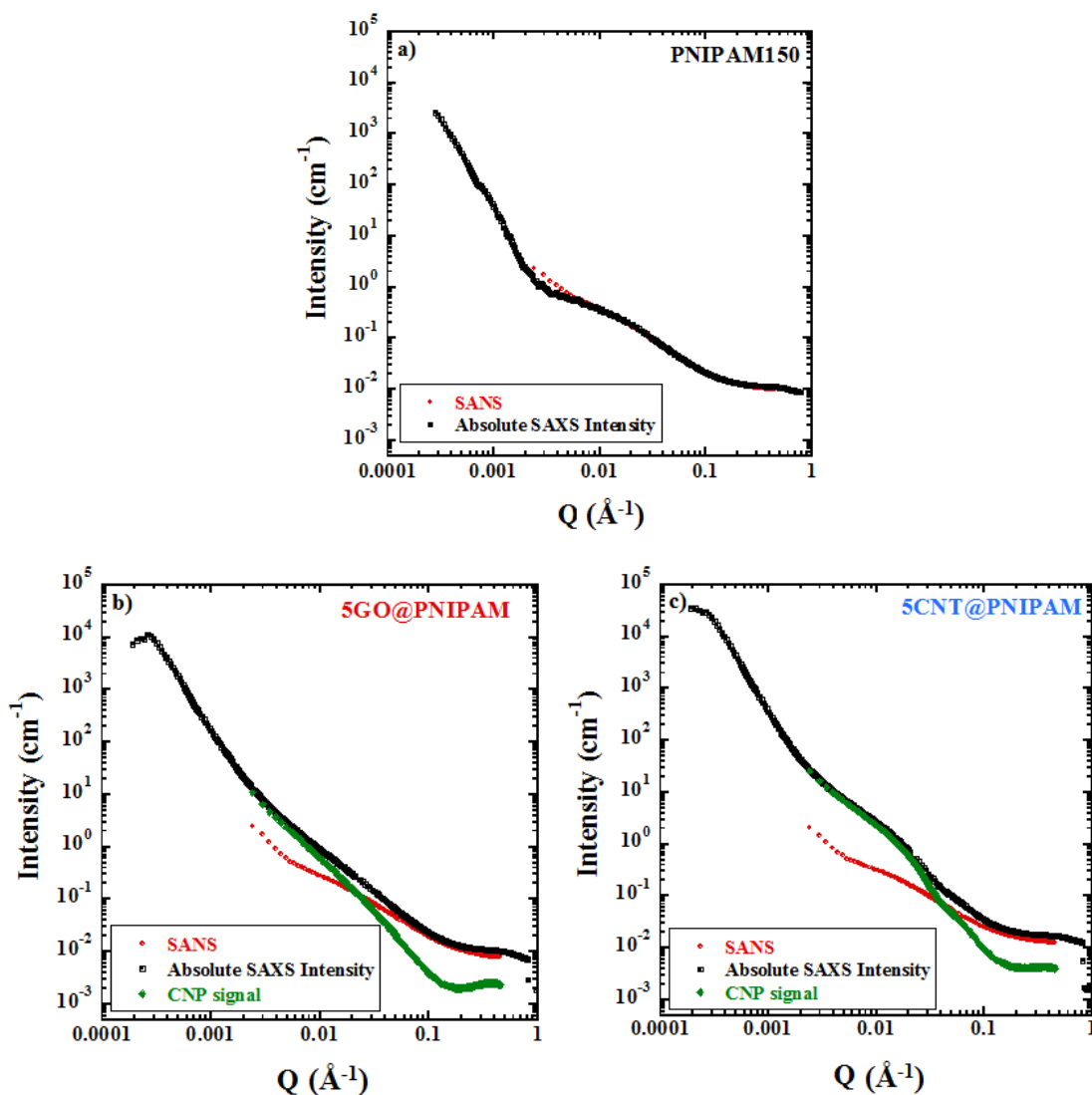
Figure 23. SANS and SAXS responses curves of selected samples at 25 °C.
The CNP signal is the difference between the SAXS and SANS signals.

of 0.6 Å^{-1}) would have resulted in a peak in the SAXS curve. This was not observed. The small bump in case of lower concentrations in Figure 24a was attributed to an artefact due to the subtraction of low absolute values. The obtained difference curves (Figure 24), which were the signal attributed to the CNPs in the composite matrix was fitted to the so-called Unified model in case of GO. The GO platelets are able to fold or wrinkle, which excluded the applicability of any well-described structure factors. This fit model is based on the unified exponential/power-law approach to small-angle scattering. The model developed by Beaucage and co-workers [272–274] is applicable to complex systems with multiple structural levels. Scattering from each level is considered to be composed of a Guinier-type exponential form and a structurally limited power law.

The used MWCNT had several characteristic lengths: the outer diameter could vary between 20-200 Å (see Chapter 5.1.) - corresponding Q values: ~0.0314-0.314 Å^{-1}, while its length was on the micrometre scale. However, as clearly visible on the macroscopic scale (Figure 16) it formed aggregates in aqueous media, owing to its hydrophobicity. Fitting the SAXS response curves using cylindrical structure factors did not give satisfactory results. On the other hand, using a size distribution function which assumes spherical nanoparticles with interfacial interactions satisfactory fits were obtained (Figure 24). This suggests that the CNT cylinders were forming spherical aggregates on the nanometric length scale.
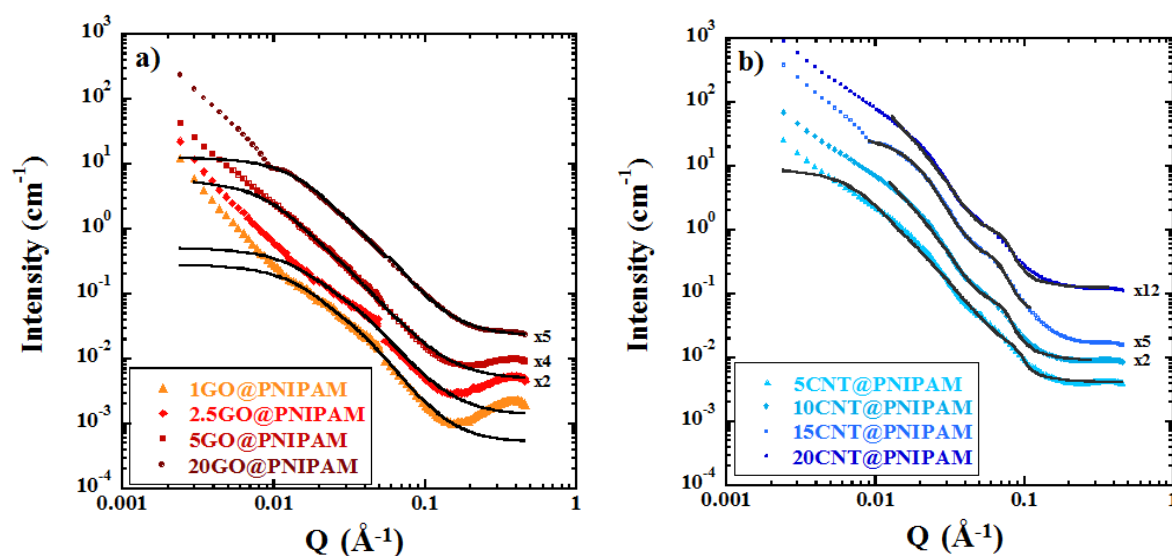

Figure 24. Difference curves of composite gels calculated from the corresponding SANS at SAXS curves at 25 °C: a) GO@PNIPAM and b) CNT@PNIPAM. The solid black lines are the used fits. The curves are shifted vertically for clarity. The used factors are shown in the figures.

The resulted characteristic length values from the Unified fit and the size distribution model can be seen in Figure 25. These were found to be around 100 Å in the GO@PNIPAM composites and showed very little variation with the GO concentration (Figure 25a). As was described before, this length scale cannot be attributed to none of the primary dimensions of the GO platelets. The GO particles are not rigid objects, which can be folded forming wrinkles as can be seen in Figure 13 and 14. Therefore, the obtained characteristic size was associated with the internal morphology. The fact that this size showed a rather random variation with the GO concentration suggest that the morphology of the GO nanoparticles was approximately the same already in the suspension state, prior gelation, and this morphology depended probably on the physicochemical properties of GO, i.e., its interaction with the solvent.
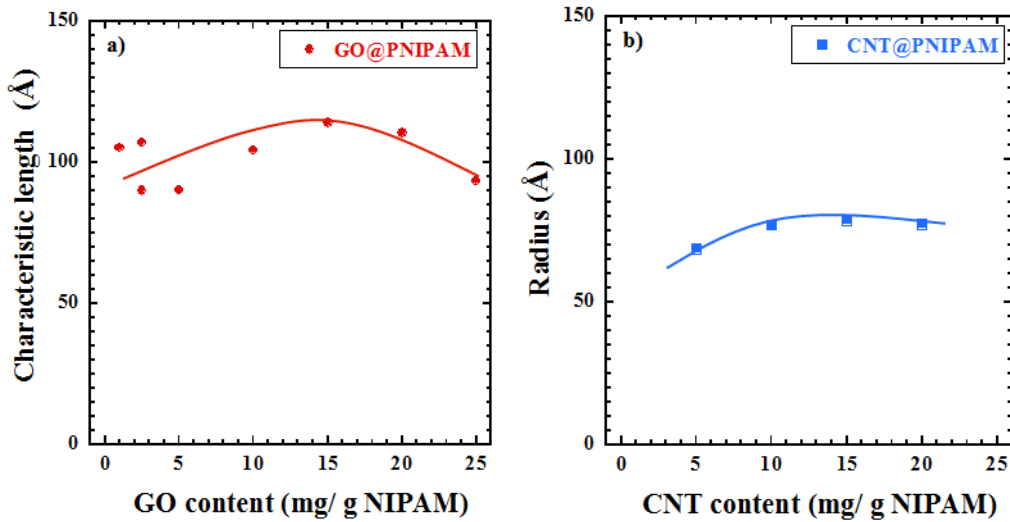
Figure 25. Characteristic values of the difference curves of a) GO@PNIPAM and b) CNT@PNIPAM at 25 °C. The solid lines are guides for the eye.

The case of CNT the spherical size distribution was fitted. The obtained diameter values were found to be practically independent on the CNT concentration, suggesting, similarly to the GO case, that the morphology of the CNT aggregates was determined already in the aqueous suspension, prior to gelation. In agreement with this observation, the fitted aspect ratio (~0,2 – 0.25) and the volume fraction (~3.6 - 3.9) showed also only a very little dependence on the CNT content.

5.3.2. Above VPTT

The structural properties of the composites might depend on the temperature above the VPTT as well. To learn whether there is a difference in their characteristics upon the used temperature gradient during the shrinkage I studied the systems at 40 and 50 °C as well. These temperatures are slightly above the VPTT, therefore, the experiments are robust and can be repeated reliably. The scattered intensity obtained from SANS measurements increased by orders of magnitude upon gel collapse at both temperatures (Figure 26). The slope of the curves dramatically increased at the low Q region, while at high Qs a constant, increased background can be seen due to the enhanced amount of incoherent scattering. The experimental curves were fitted by a combined OZ+Porod model, which implies that the amount of intensity arising from surfaces or interfaces is more pronounced:

$$I(Q) = \frac{I(0)}{1+(Q\theta)^m} + \frac{1}{Q^m} + B \tag{9}$$

where *I(0)* and *B* are *Q*-independent constants, Θ is the correlation length describing the structure inhomogeneities [275] and *m* is the Porod exponent. As it was shown before, ξ, the polymer-polymer correlation length decreases upon VPT, whereas Θ increases [276].
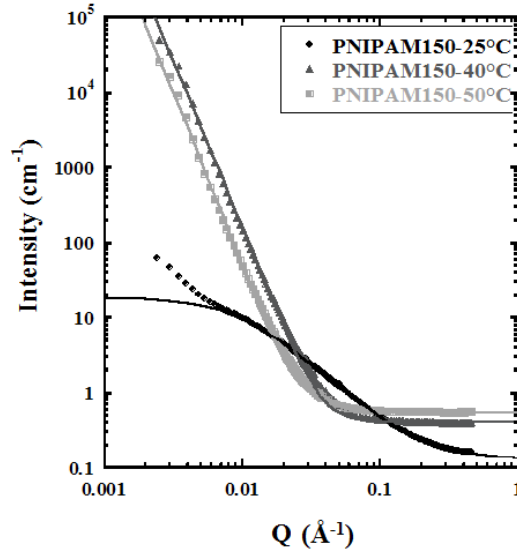

Figure 26. SANS curves of PNIPAM150 below and above the VPTT with their corresponding fits.

The obtained fits revealed that the VPT increases significantly the values of Θ in all cases (Figure 27). Θ is usually interpreted as the size of the cross-linked nods [271] in polymer gels, and can also indicate the mesh-size or blob composed of polymer chains entangled with each other [277]. This interpretation can be used in case of a collapse. The increase of Θ can be explained by the clumping of the polymer chains. As these measurements were done 10 days after plunging the samples into warm water, they might not have reached the thermodynamic equilibrium yet. Interesting to note that $\Theta_{50} > \Theta_{40}$ for all the samples. This can be a consequence of a more sudden change provoked by the higher temperature difference (i.e., stronger driving force), in which case, a more pronounced jamming is expected, resulting larger polymer blobs. On the contrary, when the driving force is smaller the phase transition is less abrupt, jamming is less likely.

The dependence of the correlation length on the cross-link density remained similar below and above the VPTT, but Θ of the less densely cross-linked systems increased by a much higher extent. Interesting to note that the difference between Θ_{50} and Θ_{40} was almost negligible for the PNIPAM50 gel. In case of the more densely cross-linked gels, shorter polymer chains could move together in a more rigid system, therefore fewer possibilities were available for the structural changes during the volume phase transition.
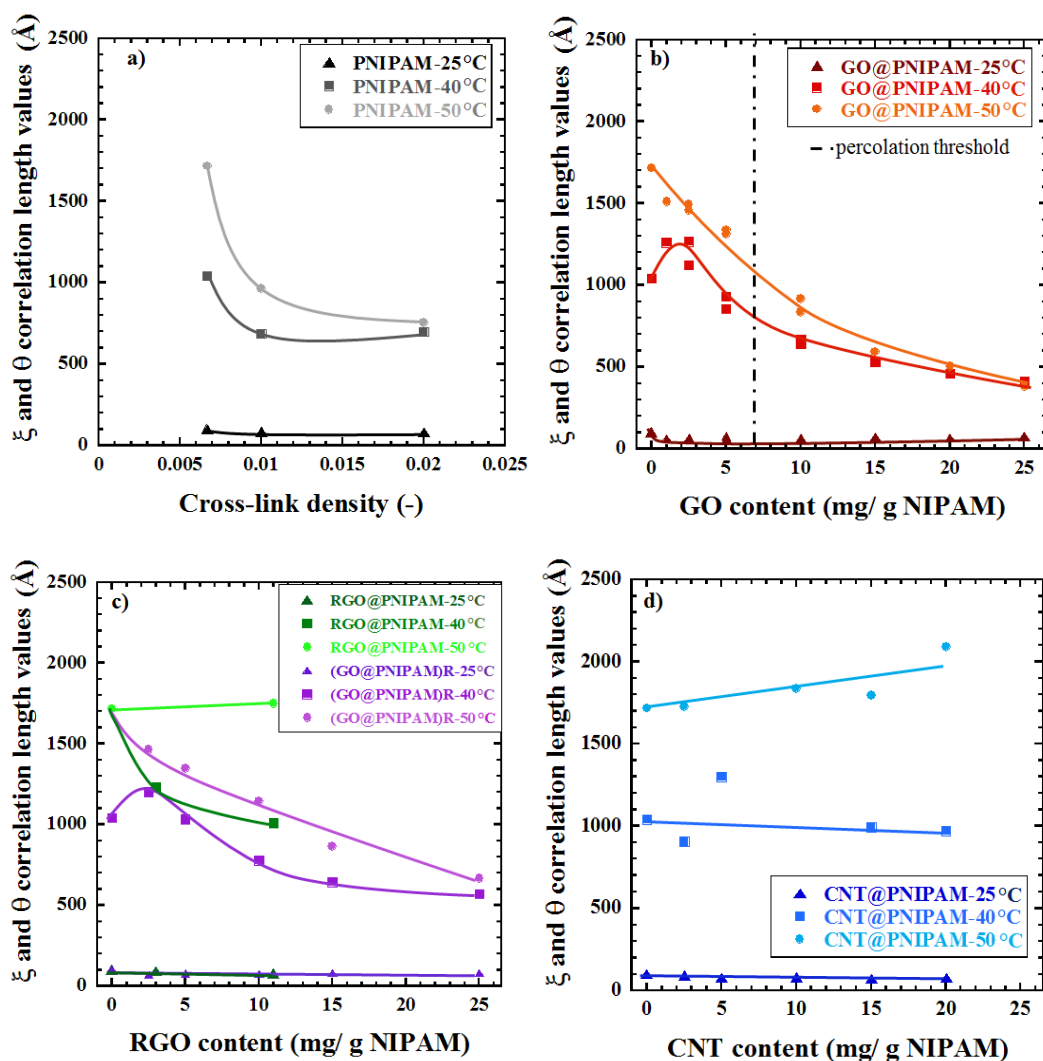
Figure 27. Static correlation length (ξ) at 25°C and network inhomogeneity correlation lengths (Θ) values at 40 and 50 °C of the different samples determined by the OZ and the combined OZ+Porod model, fitted on the SANS response curves at the respective temperatures: a) pure PNIPAM systems with different cross-link density values b-d) GO, RGO and CNT containing composites, respectively. The solid lines are guides for the eye.

Θ appeared to be strongly dependent on the GO concentration, but instead of the U-shaped curve which is observed below the VPTT for ξ values, a monotonous decrease could be seen above the VPTT (Figure 27b). At higher GO-concentrations, above the percolation threshold, the difference between the Θ_{50} and Θ_{40} was very small. Above the percolation threshold, where a continuous GO-network was assumed, the mobility of the polymer chains was lower, similarly to the highly-cross-linked systems. The incorporated GO could also be considered as a 'spacer' between the polymer blobs, this way a higher amount hindered strongly the stacking of the polymer chains, resulting in a smaller Θ value.

(GO@PNIPAM)R systems showed a very similar trend, however, the Θ values remained higher than that of the original GO@PNIPAM systems (Figure 27c). The concentration dependence could be explained by the same reasons seen at the GO containing gels, while the increment of the values upon the post-reduction process could be justified by the reduced hydrophilicity of the incorporated CNPs. Due to the hydrophobicity of the CNPs, the polymer chains were more likely to stick to their surface, to avoid the water inside the system, this way they could form more densely occupied central hubs, e.g., hypernodes. This dense structure could cause higher measured correlation length.

RGO and CNT incorporation showed a different trend again. Θ_{50} showed a slight increment in case of CNT-incorporation and remained practically independent of the RGO concentration (Figure 27c, d). Regarding Θ_{40} a slight decrease could be seen as a function of the CNP concentration for RGO nanoparticles but seemingly, the CNT-content had no effect on it.

The SAXS response curves, similarly to the SANS, showed significantly increased intensity at higher temperatures (Figure 28), however, the difference between the curves measured at 40 and 50 °C was even smaller than it was for the SANS. A structure peak could be observed at $Q=0.56075$ Å^{-1} in all cases. This value corresponds to an interchain distance in the collapsed state of $D=2\pi/Q=11.2$ Å [278].

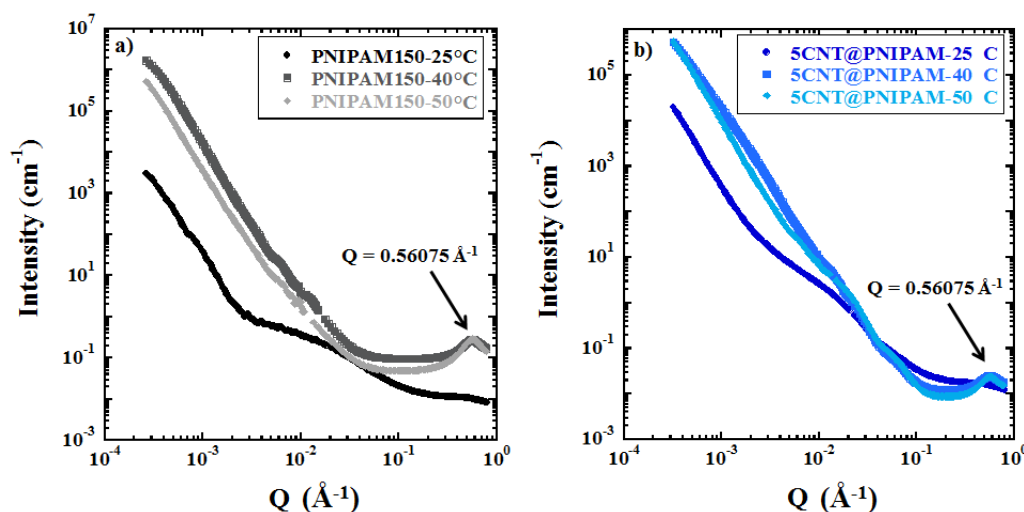

Figure 28. SAXS curves of a) PNIPAM150 and b) 5CNT@PNIPAM samples after water background subtraction at 25, 40 and 50 °C after 10 days. A structure peak could be observed at Q=0.56075 Å^{-1} in the 40 and 50 °C cases.

The calculation of the CNP signal was performed in the same way above the VPTT as it was shown in case of the low-temperature data (Figure 29) to separate the signal of the

nanoparticles from that of the polymer matrix. The increasing intensity in the low Q region is an artefact due to the subtraction.
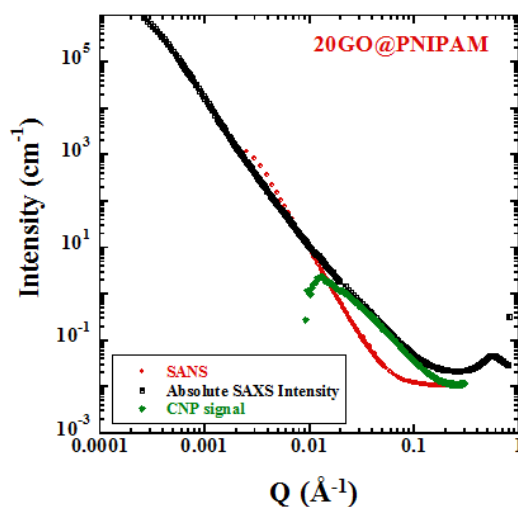
Figure 29. Comparison of SANS and SAXS intensities for 20GO@PNIPAM 50 °C after 10 days. The CNP signal is the difference between the SAXS and SANS signals.

At 50 °C, owing to the collapsed state the concentration of the polymer was higher, which resulted in that its scattering signal strength became comparable to that of GO particles. As a consequence in case of low GO concentration, no usable signal could be extracted with this method (Figure 30a). On the other hand, in case of CNT@PNIPAM samples, the string scattering of the CNT aggregates still dominated the overall signal of the nanocomposites. As a result, the obtained nanoparticle signals were satisfactory, even for low CNT concentration (Figure 30b).

Figure 30. Scattering signal of the nanoparticles derived from the (SAXS-SANS) difference of the corresponding nanocomposite samples at 50 °C after 10 days of heat treatment. The solid lines are the used fits. The curves are shifted vertically for clarity. The used factors are shown in the figures.

67

The fitting procedure was identical to the one used at low temperatures. The characteristic length of the GO@PNIPAM systems was lower than below the VPTT, which could be explained by the deswelling process. As the polymer cha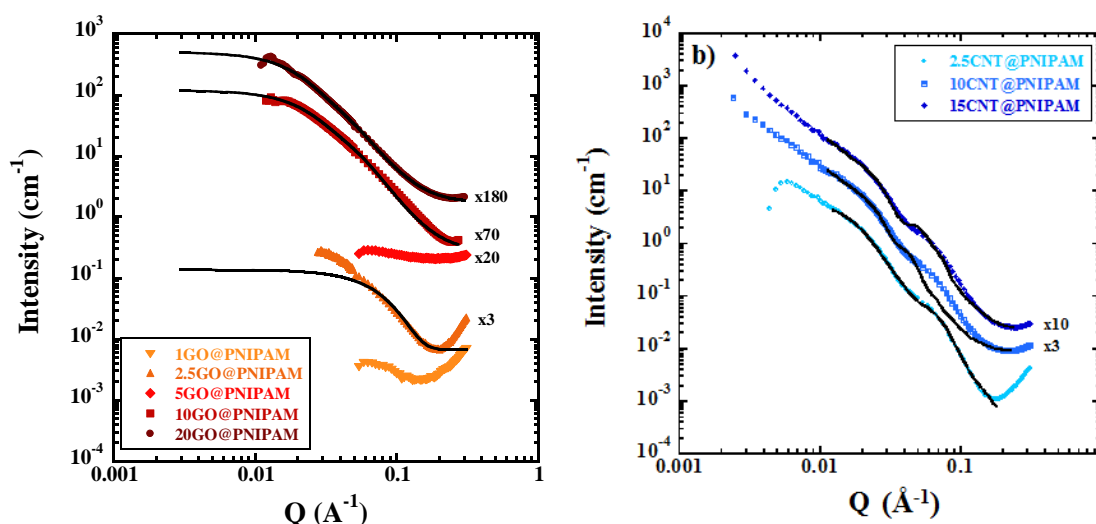ins were getting closer to each other, they forced the GO platelets to do the same. The characteristic length slightly increased with the GO-concentration (Figure 31a). The difference between the low- and high-temperature characteristic length values decreased with increasing GO concentration, and in case of the 25GO@PNIPAM, the value below and above the VPTT is practically unchanged.

This can be explained by the more pronounced interpenetrating character of the network that is formed by GO. At the highest concentration, where the platelets already form a complete network, the 10-day incubation time was not enough to affect the characteristic length.
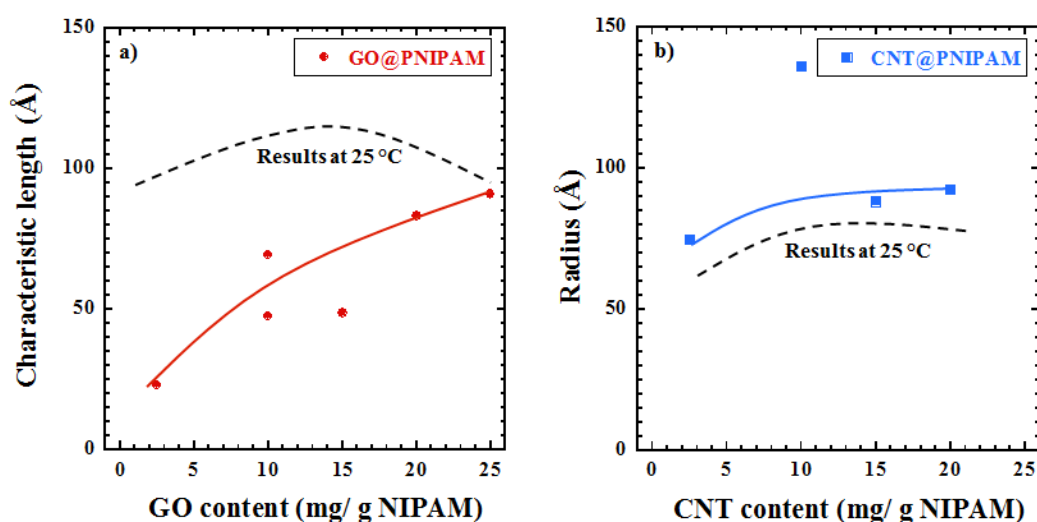
Figure 31. Fitted characteristic values of the difference curves of a) GO@PNIPAM and b) CNT@PNIPAM at 50 °C after 10 days. The solid lines are guides for the eye. The dashed lines represent the data from Figure 25.

In case of the CNT@PNIPAM systems, the observed change was the opposite (Figure 31b). A slight increase was seen in the radius of the CNT aggregates upon the collapse, which suggest that the nanotube-aggregates were getting closer to each other forming apparently bigger clusters. The aspect ratio increased (~0,5 – 0.6), while the volume fraction decreased (~2.7 - 3.0) in comparison to the fitted values below the VPTT, which also confirmed a slightly larger, more spherical shape.

Summary of structural observations

As a conclusion of the previously presented structural investigations, I propose the internal structure of the composites in the following way:

The experienced complex effect of the GO implies that during the polymerisation the GO particles might not only act as fillers in the network but also contribute to nucleating the reaction at their surfaces forming second and/or first order bonds. With increasing GO content, the gel is reinforced by the filler and the architecture of the network is increasingly dominated by cross-link hypernodes, at the expense of the simple tetrafunctional cross-link structure that prevails with the BA cross-linker alone (Figure 32). By the post-reduction treatment, not the structure, but only the interactions between the polymer matrix and the CNPs were influenced, which proves the efficiency of the method.

The incorporation of the RGO and the CNT occurs in aggregates which do not modify the character of the gel structure; their effect is limited to the characteristic distances inside the matrix.

PNIPAM cross-links   PNIPAM cross-links with   PNIPAM cross-links
                            CNT aggregates   with GO-hypernodes
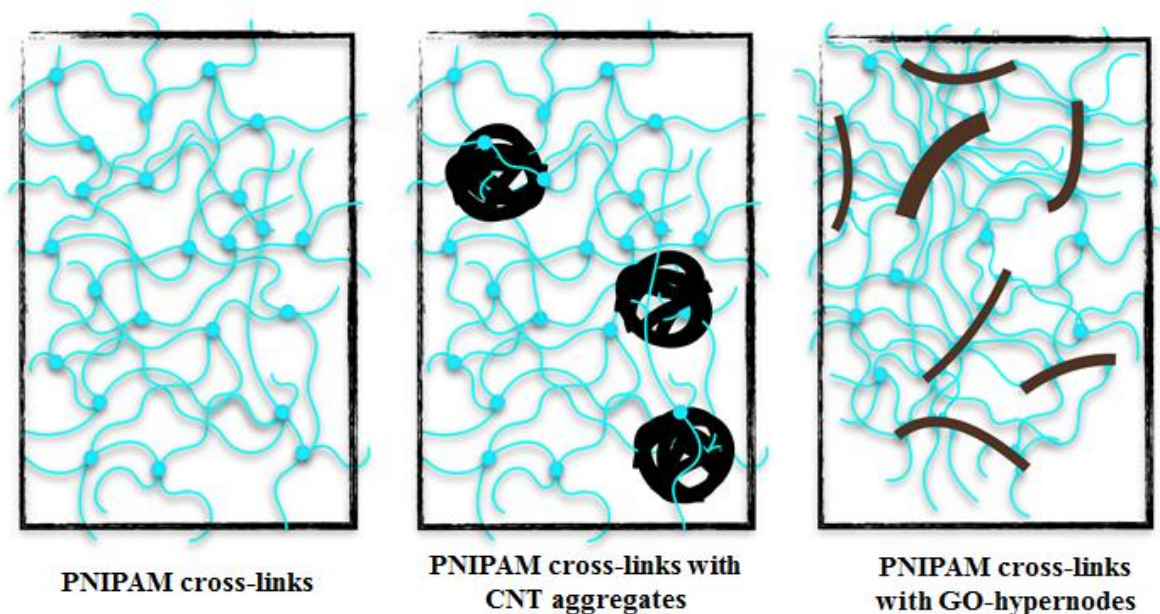
Figure 32. Proposed internal structure of pure gels and CNP containing composites.

5.4. Nanoparticle – polymer interactions in the composites

As it was described above, both the microscopic and macroscopic measurements suggested a strong interaction between the GOs and the polymer matrix and a weak interaction between the CNT or RGO and the polymer matrix. Similar suggestions have been proposed earlier [101,240,279], however, the nature of these interactions is still unrevealed. The possibilities are numerous, e.g., first-order bonds with the oxygen-containing functional

groups or with the carbon lattice, secondary bonds (H-bonding) or entanglement of the polymer chains on the platelets [101,240,279].

To gain further knowledge, thermogravimetric measurements were performed to shed light on this question. Although the shape of the TA curves was very similar for the different type of nanocomposite samples (Figure 33), the obtained residual masses varied with the CNP type.
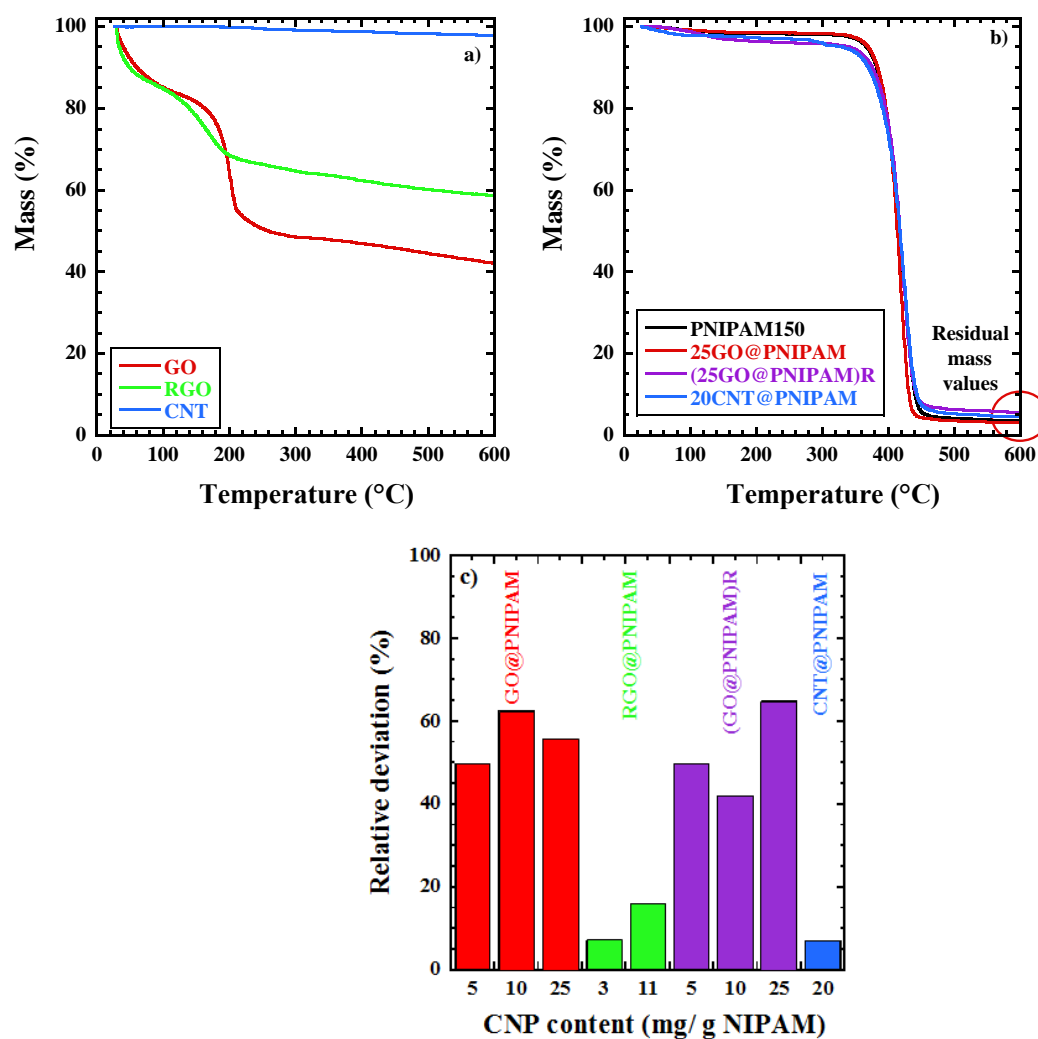
Figure 33. Thermograms of a) nanoparticles and b) the pure PNIPAM gel and nanocomposites in N₂ atmosphere. c) Calculated difference between the theoretical (TRM) and experimental (ERM) values of the residual masses.

The thermogravimetric responses of the CNT@PNIPAM, GO@PNIPAM, (GO@PNIPAM)R and RGO@PNIPAM composite systems were compared to reveal their differences.

To quantify these differences, the theoretical residual mass (TRM) for independent decomposition was calculated from

$$TRM(\%) = c_{CNP} \cdot m_{CNP} + (100 - c_{CNP}) \cdot m_{PNIPAM} \qquad (10)$$

where c_{CNP} is the nanoparticle concentration in m/m%, m_{CNP} and m_{PNIPAM} are the residual masses at 600 °C for the nanoparticle and the pure PNIPAM, respectively. TRM implies an independent decomposition, i.e., no interaction between CNP and the polymer matrix. The relative deviation of the experimental values (experimental residual mass, ERM) from TRM was calculated by

$$Relative\ deviation\ (\%) = \frac{ERM - TRM}{TRM} \cdot 100 \tag{11}$$

Comparing this relative deviation for the different CNPs significant differences could be observed (Figure 33). The discrepancy in the case of GO containing gels was more than 50%. This suggests strong, possibly even covalent bonds or secondary bonds with similar strength between the GO sheets and the polymer chains. Post reduction had no significant effect on the deviation of ERM, suggesting that majority of the formed interactions between GO and the polymer matrix was not affected by the treatment. This is in line with the macroscopic observations, i.e., elastic moduli and equilibrium swelling degree values. On the contrary, in CNT and RGO@PNIPAM samples the relative deviation was significantly smaller (ERM was close to the theoretical value) indicating that the interactions between the RGO sheets or the CNT aggregates and the polymer were much weaker.

Thermogravimetric measurements were able to quantify the difference between the strength of the interactions but did not provide information about the nature of the bond.

Solid-state NMR studies were carried out to get this information. NMR spectroscopy is an effective technique that is widely used to characterize macromolecular, especially amorphous and mixed systems. Cross-polarization ^{13}C MAS spectra of the pure, the GO-, CNT- and RGO containing gel samples were found to be identical, no new signal was observed. Based on this, we can practically exclude the formation of large number of new chemical bonds. Signals from GO or RGO could not be identified because of their small amount in the samples and their very broad signals. Varying the contact time (*t*), in which the magnetization transfer occurs between the excited hydrogen atoms to the carbon atoms resulted in the cross-polarization build-up curves (Figure 34).
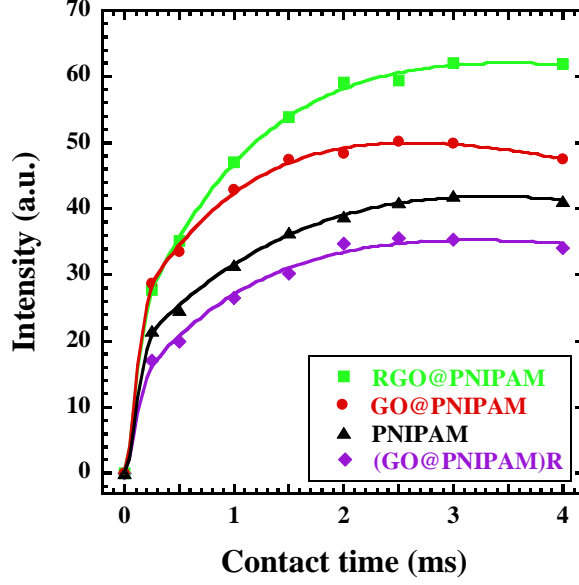
Figure 34. Solid-state NMR cross-polarization build-up curves of carbonyl ^{13}C atoms. Solid lines are fits to Eq. 12.

The shapes of the peak intensity (*I(t)*) vs *t* curves gives information about the proton environment of the carbon atoms and their mobility. The build-up curves were fitted to the I-I*- S model (Eq. 12) [280], which is typically used in case of less mobile organic molecules like polymer gels:

$$I(t) = I_0 \exp\left(-t/T_{1\rho}^H\right) [1 - \lambda \exp\left(-t/T_{df}\right) - (1-\lambda) \exp\left(-\frac{3}{2}t/T_{df}\right) \exp\left(-\frac{1}{2}t^2/T_2^2\right)]$$

(12)

where I_0 corresponds to the absolute amplitude, $T_{1\rho}^H$ is the relaxation time constant of the ^1H in contact with the lattice in the rotating frame, T_{df} is the proton spin-diffusion constant, T_2 is the spin-spin relaxation time and $\lambda = 1/(n+1)$, where n is the number of ^1H in the spin system. The build-up curves and the fitted parameters were found to be the same for the isopropyl carbons, which suggests that the hydrophobic interactions between the isopropyl groups and the CNPs were negligible. The build-up curves of the carbonyl carbons were nevertheless different in shape, as Figure 34 shows. Results of the fitting to I-I*-S model (Eq 12.) are summarized in Table 7. The obtained $T_{1\rho}^H$ of GO@PNIPAM and (GO@PNIPAM)R decreased in the same extent. This indicated that the environment of the carbonyl group was more rigid here than in the pure PNIPAM gel, implying a strong interactions between PNIPAM and GO nanoparticles. These interactions seemed to be not affected by the post-reduction treatment.

On the contrary, the increase of $T_{1\rho}^H$ in the RGO@PNIPAM sample suggested an increased mobility in the neighbourhood of the carbonyl groups. Change of the T_{df} indicated modification also in the moieties of ^{1}H atoms around the carbonyl atoms.

Table 7. Fitted parameters of the I-I*-S model to the cross-polarization build-up curves of the carbonyl carbon.*

Sample	λ	T_{df} (ms)	$T_{1\rho}^H$ (ms)	T_2 (ms)	I_0 (a.u.)
PNIPAM150	0.75±0.05	2.0±0.1	13.9±0.1	0.1±0.01	62
GO@PNIPAM	0.75±0.05	1.6±0.4	10.1±0.7	0.1±0.01	75
RGO@PNIPAM	0.75±0.05	1.3±0.4	23.2±2.0	0.1±0.01	76
(GO@PNIPAM)R	0.75±0.05	1.7±0.2	10.4±0.6	0.1±0.01	55

*λ: = $1/(n+1)$, where n is the number of ^{1}H in the spin system; T_{df}: proton spin-diffusion constant; $T_{1\rho}^H$: relaxation time constant of the ^{1}H in contact with the lattice in the rotating frame; T_2: spin-spin relaxation time; I_0: plateau level

Thermogravimetric and NMR observations revealed strong interactions between GO and the polymer matrix, which were practically retained during the post-reduction treatment. These results, however, provided no clear evidence of covalent bonds. Further evidence is needed to reveal the real reason of the enhanced interactions. A possible explanation of the strong interaction is that the damaged graphene structure may offer a niche for the polymer segments growing during the polymerisation in the confinement created by the carbon sheets [281].

5.5. Effect of temperature

5.5.1. *Local dynamics below the VPTT by Neutron Spin-Echo Spectroscopy*

The dynamic behaviour of the PNIPAM matrix on the microscopic length scale was explored by NSE. Due to the fact that the NSE is a rather time-consuming and hard-to-reach method only some selected samples were measured. The intermediate scattering function *I(Q,t)* curves obtained for the pure PNIPAM gel, as well as for samples 5GO@PNIPAM, 20GO@PNIPAM, 5CNT@PNIPAM and 20CNT@PNIPAM at 25 °C normalized by the signal (*I(Q,0)*) of a fully elastic scatterer (graphite), are displayed in Figure 35. As already noted, the scattering contrast between the CNPs and pure D_2O is small. In the *Q*-range covered by the NSE measurements, CNPs are in contrast matched condition, the observed

dynamics can therefore be attributed exclusively to the motion of the chains in the polymer gel. In all cases, the curves $I(Q,t)/I(Q,0)$ can be fitted by a single exponential function.

$$\frac{I(Q,\tau)}{I(Q,0)} \propto \exp(-\Gamma\tau)$$

(13)

The measured relaxation rates ($\Gamma=1/\tau$) were proportional to Q^2, characteristic of diffusive motion. The diffusion coefficient (D_{diff}) was obtained directly from the linear fit $\Gamma=D_{diff}\cdot Q^2$. The hydrodynamic correlation length of the samples (ξ_H) was determined from the Stokes-Einstein relation.

$$D_{diff} = \frac{k_B T}{6\pi\eta\xi_H}$$

(14)

where k_B is the Boltzmann constant, T is the absolute temperature and η is the viscosity of the medium (Table 8).

Table 8. Viscosity of D_2O [282,283].

Temperature (°C)	Viscosity (Ns/m^2)
10	1.6794e-3
25	1.095e-3
30	9.686e-4
40	7.872e-4
50	6.e4870e-4

In the pure PNIPAM150 gel (Figure 35a) the curves decayed to zero, indicative of practically ergodic behaviour, i.e., there was no frozen-in component [270]. GO affected the elastic properties of the composite systems on the macroscopic scale, but at the microscopic level, by contrast, the NSE results indicate that the motion of the polymer chains was only partially affected. Similar results were found in case of the CNT@PNIPAM samples as well. The NSE curves appeared to decay to zero as in the pure PNIPAM150 gel.

Below VPTT in addition to the measurements at 25 °C NSE measurements were performed at 10 and 30 °C. The obtained diffusion constant showed strong temperature dependence (Table 9), however, these variations practically followed the temperature dependence of the solvent viscosity.
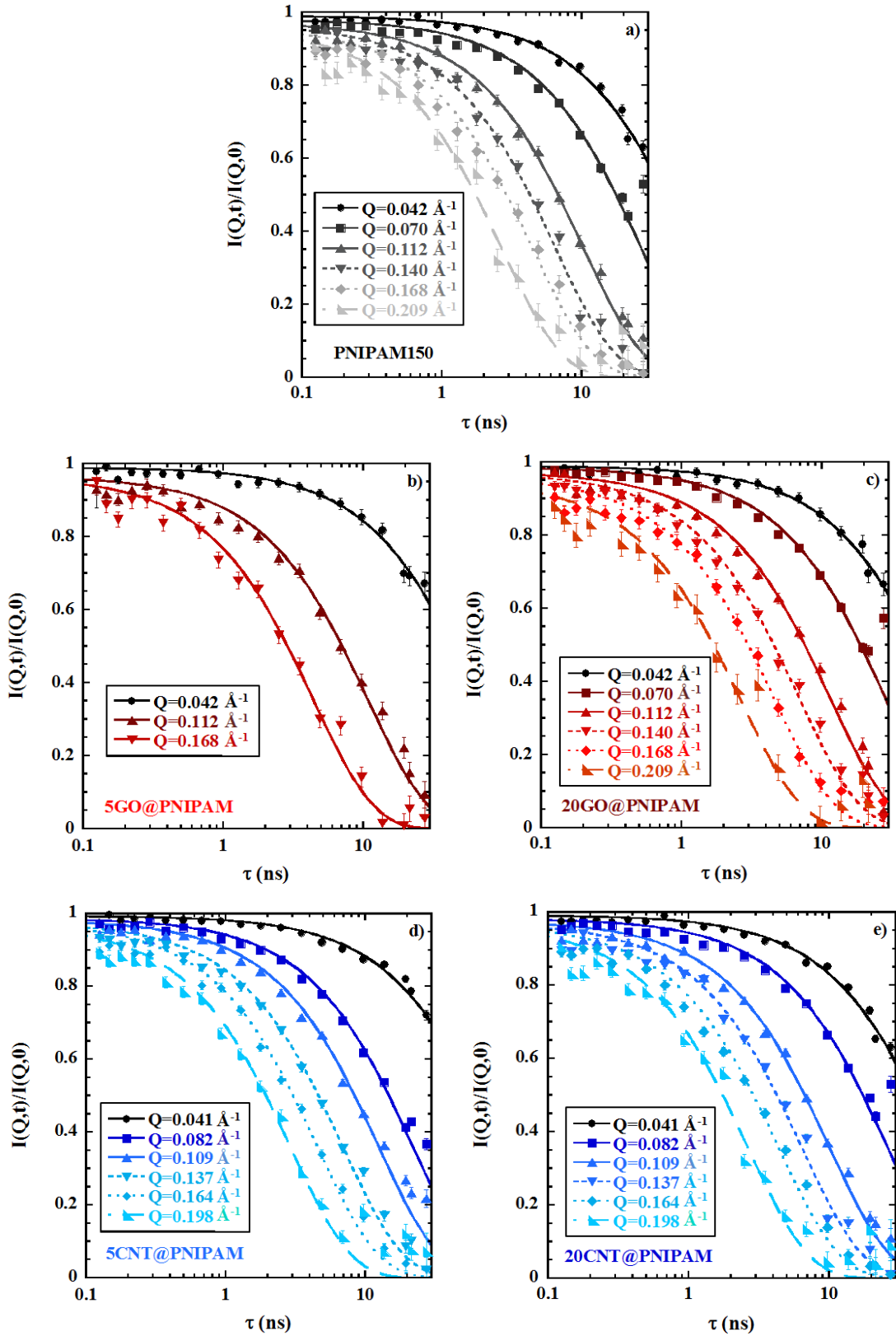
Figure 35. Measured intermediate scattering functions (ISFs) of a) PNIPAM150, b) 5GO@PNIPAM, c) 20GO@PNIPAM, d) 5CNT@PNIPAM) and 20CNT@PNIPAM at 25 ˚C.

Table 9. Diffusion coefficients measured by NSE below the VPTT.

Sample	Diffusion coefficient (x 10^{-11} m^2/s)		
	10 °C	25 °C	30 °C
PNIPAM150	5.80	7,86	8.96
5GO@PNIPAM	-	8.08	8.42
20GO@PNIPAM	5.17	7.69	8.62
5CNT@PNIPAM	-	7.45	9.14
20CNT@PNIPAM	-	8.27	8.94

As a result, the obtained ξ_H values were only slightly affected by the temperature (Figure 36).
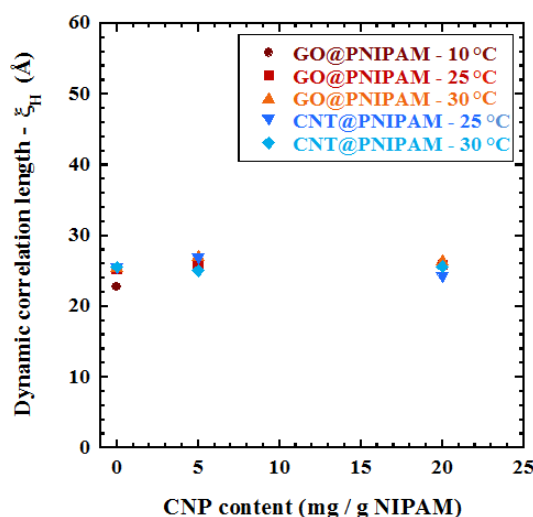
Figure 36. Dynamic correlation lengths of pure PNIPAM150, GO@PNIPAM and CNT@PNIPAM composites at 10, 25 and 30˚C.

ξ_H is generally interpreted as the size of the elementary unit within the sample that is able to move together. The measurements revealed that the CNP incorporation did not modify the size of this unit, and in both the pure PNIPAM and the investigated nanocomposites these units were not affected by the temperature (i.e., the swelling degree of the system).

Measurements above the VPTT have also been performed. The preliminary results are shown in the Appendix (Chapter 8.).

5.5.2. Static studies

The relative equilibrium swelling degree was compared at different temperatures for the various systems in order to gain information about the temperature-dependent behaviour of the systems (Figure 37). No difference was found in the temperature dependence of the

PNIPAM100 and PNIPAM150 systems. Similarly to the filler-free PNIPAM, the swelling of the nanocomposite systems showed a strong temperature dependence: the relative swelling degree nonlinearly decreases up to the VPTT and remained constant above it. While the swelling curves of the CNT@PNIPAM and RGO@PNIPAM systems practically overlapped with pure PNIPAM, the GO containing systems were less ready to deswell up to 35 °C. This may partly originate from the hydrophilicity of the GO platelets, which may compensate the strengthening hydrophobic interactions within the polymer matrix with increasing temperature.
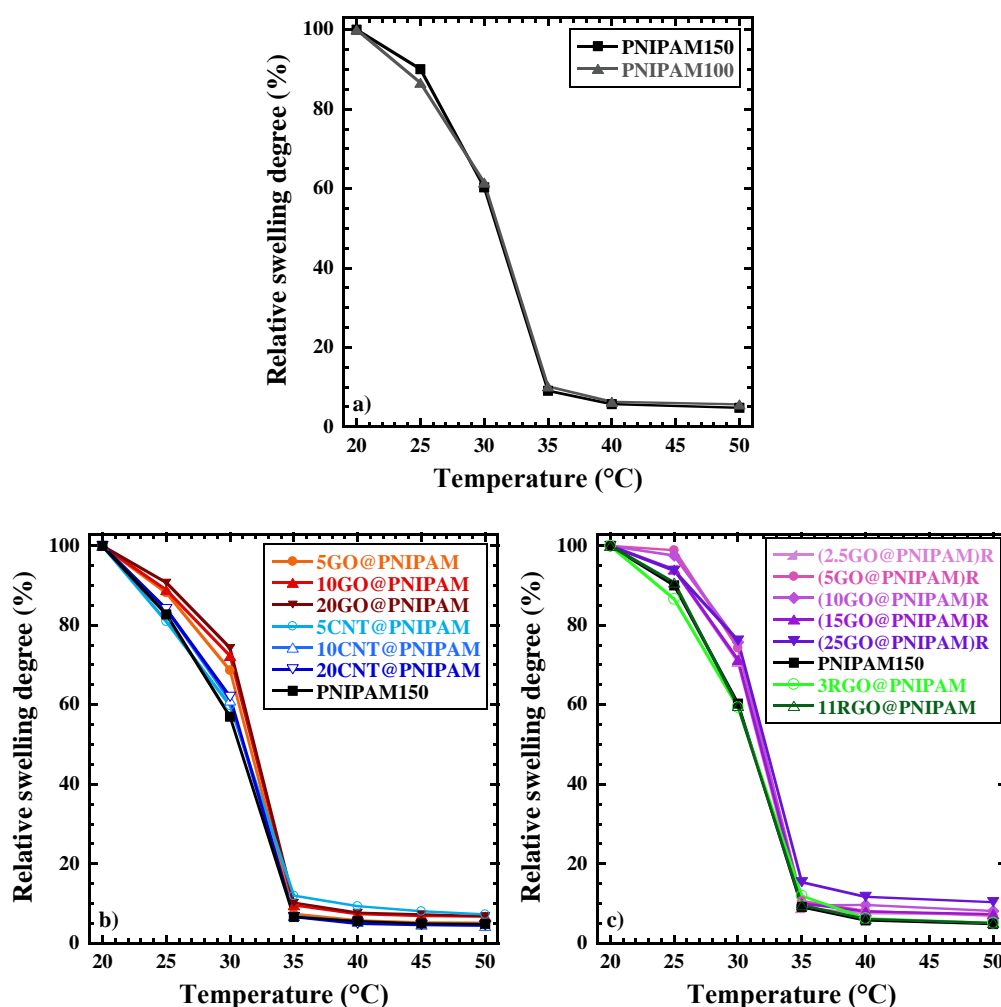
Figure 37. Temperature dependent relative equilibrium swelling degree values of the pure PNIPAM and composite systems.

The post-reduction had practically no influence on the swelling characteristics of the composite gel (Figure 37b, c). The decreased hydrophilicity due to the reduction process did not influence strongly the measured values. It suggests that the formed hypernode-structure was not affected by the reduction treatment, which is in accordance with the data presented in

77

the previous chapters. It can also be assumed that this structure was responsible for the different deswelling upon temperature-increment below the VPTT. Above the VPTT, the absolute equilibrium swelling degree was very similar for all the systems (1.7±0.4). The differences in the relative values originate from the differences at 20 °C. There was no significant concentration effect for any of the CNP families. The temperature-dependent swelling was, therefore, only determined by the quality of the nanoparticles.

The results of the above described macroscopic measurements clearly show that the temperature-sensitivity was conserved during the incorporation of the CNPs. To investigate in details the process and reveal eventual, very fine differences differential scanning microcalorimetry (DSC) measurements were performed. The DSC curves of pure gels of various cross-link density can be seen in Figure 38a. The VPTT (33.9±0.1 °C) did not change
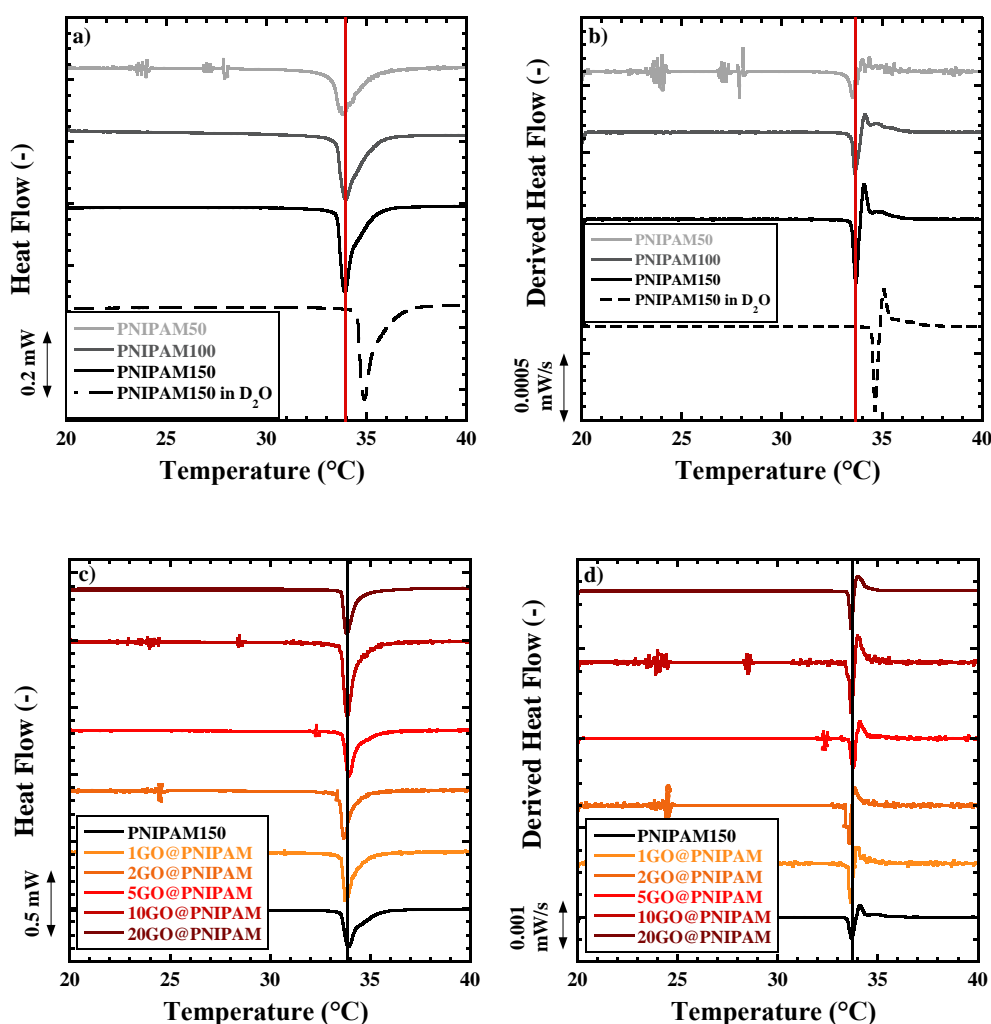

Figure 38. DSC curves of selected samples: a-b) pure PNIPAM systems with different cross-link density values and c-d) GO@PNIPAM composites.
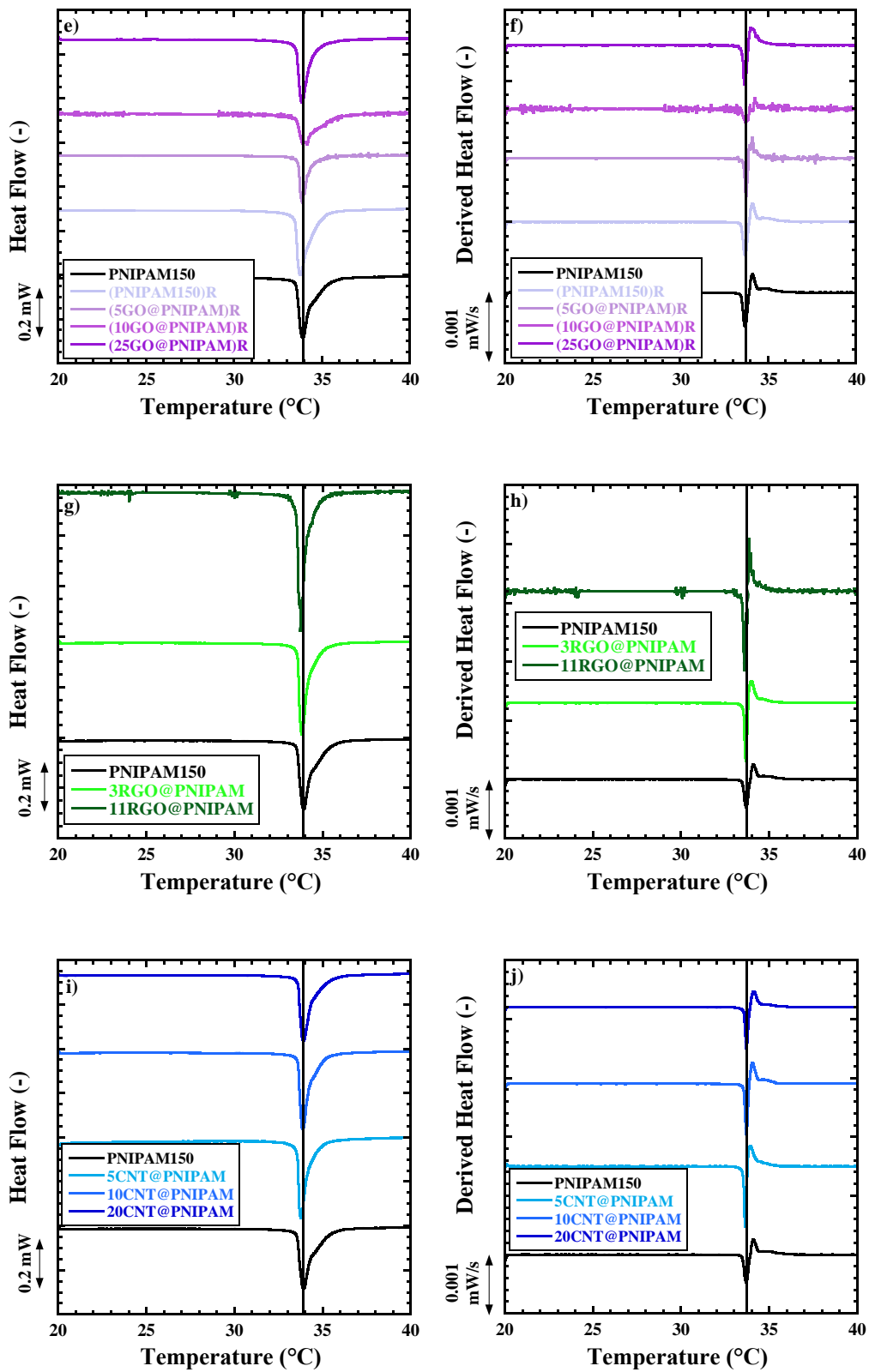
Figure 38. DSC curves of selected samples: e-f) (GO@PNIPAM)R, g-h) RGO@PNIPAM and i-j) CNT@PNIPAM composites.

79

only the peaks widened with increasing cross-link density. As the neutron scattering experiments were performed in heavy water, the PNIPAM150, PNIPAM100, GO@PNIPAM and CNT@PNIPAM samples were measured in D_2O as well. It was found that the shape of the signals did not change, however, a shift of +1 °C the VPTT was observed in all cases. The curve of the pure PNIPAM150 in D_2O is shown in Figure 38a,b as a representative example. Figure 38c,d reveals that VPTT was unaffected by the presence of GO, which implies that although part of the polymer chains is tightly bound to the GO surface, the rest remained freely surrounded by the solvent and was subjected to excluded volume conditions. The post-reduction process, CNT or RGO incorporation did not affect the responsivity either (Figure 38e-j).

In general, the VPTT of the PNIPAM-based gels could be tuned by changing their hydrophilic/ hydrophobic balance, e.g., by co-polymerization [284,285]. Strong interactions, for example covalent bonds between the CNPs and the polymer network would be able to influence this balance as well. The lack of the change in the VPTT could be explained by the low CNP concentration or the lack of the covalent bonds. The DSC measurements showed no difference in the VPTT and the corresponding specific enthalpy (33.9±0.1 °C and 52±2 J/g, respectively) in the systems (Figure 39).

According to the literature, the enthalpy of the phase transition and the VPTT do not depend on the cross-link density [286]. Based on the presented DSC measurements the CNP content has no significant effect either. The unchanged specific enthalpy values suggest that the VPT is completed during the DSC conditions.
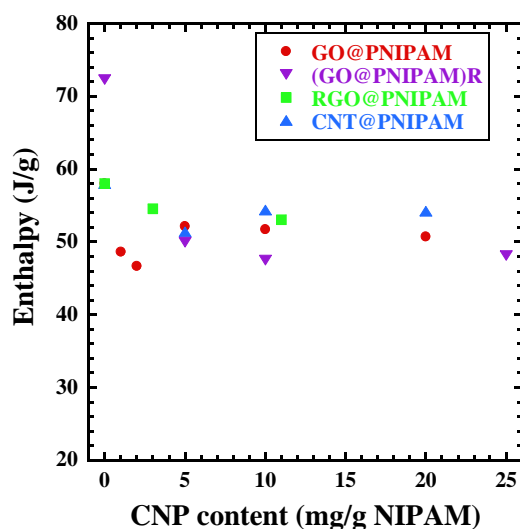

Figure 39. Effect of the CNP content on the enthalpy of deswelling of the various filled systems.

5.5.3. Dynamic properties

5.5.3.1. Temperature-jump induced deswelling kinetics

While the equilibrium swelling properties, the VPTT and the enthalpy of phase transition of the different nanocomposites were only slightly influenced by the composition; the kinetics of the response following an abrupt increase in temperature of the swelling medium revealed significant differences and a more complex behaviour. Two temperatures were used above the VPTT to investigate the effect of the temperature gradient on the phase transition.

Pure PNIPAM gels at 40 °C and 50 °C

The pure PNIPAM gels responded to the temperature jump with an immediate colour change, as reported previously [9,287]. Monitoring the weight loss of the gel disks in time showed that the swelling degree of the gels changes according to a different scheme (Figure 40). When the PNIPAM150 was plunged to water at 40 °C, a two-step shrinking process could be seen. In the beginning of the shrinkage, part of the water content was trapped inside the gel, which was then slowly expulsed during the second step. When the cross-link density was increased (PNIPAM100 or PNIPAM50), the response became slower and a stretched quasi-one step process could be seen. When a higher temperature-difference was used (20 → 50 °C) a completely different behaviour was experienced. PNIPAM150 reached its final value in a quasi-single-step process in about 30 minutes, while in case of the higher cross-link densities, two, well-pronounced steps could be seen. Interesting to note, that there was only a slight difference in the shrinkage of PNIPAM100 and PNIPAM50.
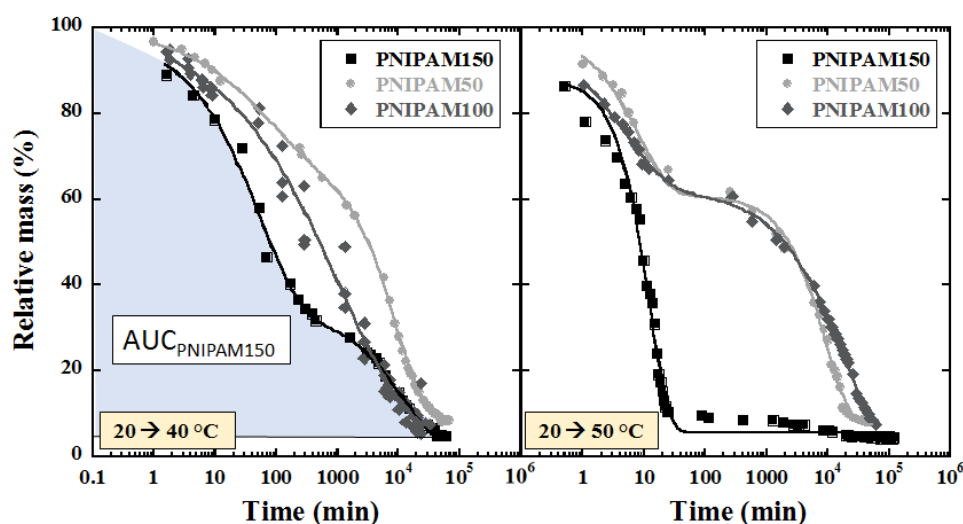
Figure 40. Semi-logarithmic plot of temperature shock (20→ 40 °C and 20→ 50 °C) induced shrinkage kinetics of pure PNIPAM gel.

Figure 41 visualizes the discrepancy between the mass change of the PNIPAM gel with different cross-link densities in the course of deswelling at 40 and 50 °C. PNIPAM100 and PNIPAM50 were compared to the PNIPAM150 as a reference. Both shrunk much slower in the beginning of the process, at 40 and 50 °C as well. After PNIPAM100 (i.e., the less densely cross-linked) practically finished the respective deswelling step, slight differences could be seen between the gels with higher cross-link density.
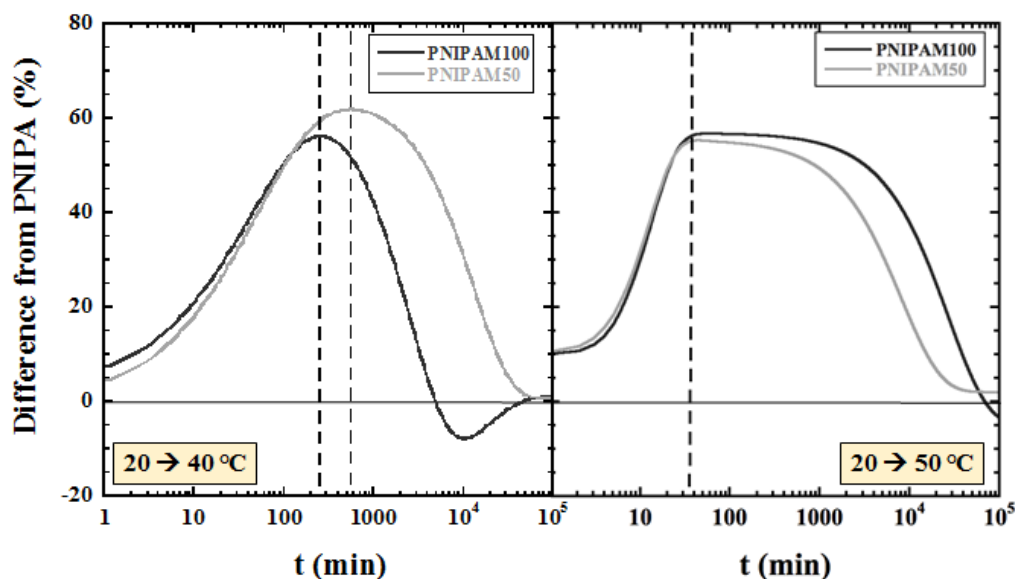
Figure 41. Shrinkage difference obtained at 40 and 50 °C as a function of time with respect to pure PNIPAM150. Vertical dashed line shows the position of the maxima.

To quantify the observed differences, the curves were fitted to an exponential function (Eq. 7, Page 43). The fact that a non-linear decay function was found to satisfactorily describe the experimental data implies the velocity of the expulsion of the solvent is not constant during the process. To account for the two, distinct kinetic steps a combination of two exponential decay functions were used. It was found that single exponential functions did not give a proper fit to the experimental data; therefore, stretching/compressing exponents (p_1 and p_2 in Eq 7) were introduced. The resulted exponents are shown in Figure 42. Tabular data of all the obtained fitting parameters are given in Table 10.

Table 10. Fitted parameters of the kinetic curves at different temperature jumps according to Eq. 7.

Final temperature	Sample	$\left(\dfrac{m_\infty}{m_i}\right)$	A_1	t_1 (min)	p_1	A_2	t_2 (min)	p_2
40 °C	PNIPAM150	3.3	64.7	51.9	0.64	30.0	11094	0.79
	PNIPAM100	4.6	95.7	1092	0.39	0	0	0
	PNIPAM50	8.6	32.6	68.0	0.50	59.1	9262	0.97
50 °C	PNIPAM150	5.5	82.6	12.0	1.33	0	0	0
	PNIPAM100	0.6	37.5	4.8	0.61	61.7	18319	0.67
	PNIPAM50	7.5	38.7	8.1	0.83	53.4	8958	1.09
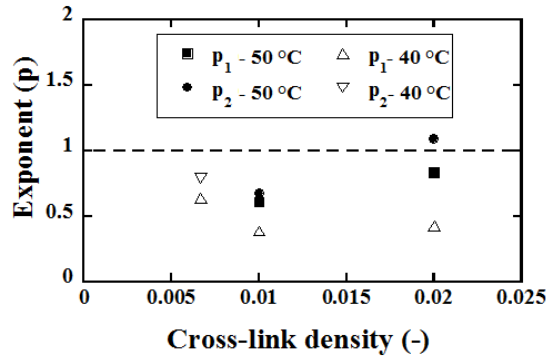
Figure 42. Exponents of the fitted deswelling curves.

The nature of the exponent, p_i (i.e., stretched, single, or compressed) can reveal further information on the kinetics [254,287–289]. Generally, in complex dynamical processes the observation of stretched exponentials ($p<1$) reflects the simultaneous presence of several processes, while an exponent $p >1$ (i.e., compressed exponential function) is a signature of hyperdiffusive motion and jamming. The jamming behaviour of unloaded PNIPAM gels was revealed earlier [287]. In the pure PNIPAM gel samples during the 20 → 40 °C transition the p value was found <1 in all cases revealing a non-jamming behaviour. At higher temperature, PNIPAM 150 and PNIPAM50 showed jamming during the first step.

Owing to the highly-stretched nature of the exponential curves and the different number of steps observed in the different systems the comparison of the numerical value of these data may be misleading. To overcome this problem and characterise globally the deswelling process the integral (area under curve, AUC) has been calculated for each deswelling curve (Figure 43), whose value can be related to the inverse of the average velocity of the water

expulsion. If the AUC is high, the system requires more time for total deswelling. Figure 40 shows an example on how the integration was performed. The AUC values of the deswelling at 40 °C showed no significant dependence on the cross-link density, on the other hand, at 50 °C, as was expected based in Figure 40, the PNIPAM150 deswelled very quickly, its AUC was orders of magnitudes lower than for the other samples. In case of higher cross-link densities, their fast response in the first step was followed by an extremely slow structural rearrangement, which resulted in a higher AUC value than at 40 °C.
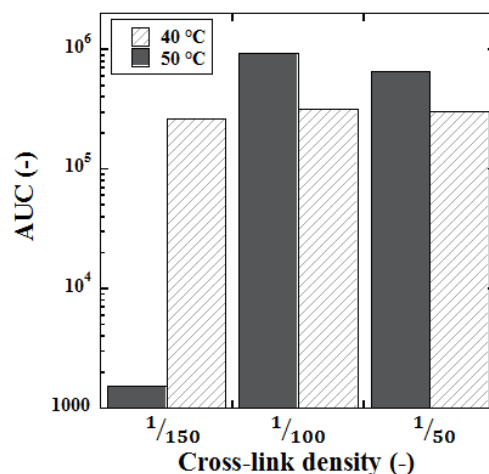
Figure 43. AUC values of the deswelling curves in Figure 40.

Composite gels at 40 °C

In the composite systems, the immediate colour change was also observed upon immersing into warm water, but the kinetics of the deswelling was different from that of the pure gels (Figure 44). CNT@PNIPAM systems conserved the two-step character of the deswelling, while GO incorporation resulted in a one-step, stretched shrinking curve.

Compared to the pure PNIPAM150, the practically hydrophobic CNTs resulted in a slightly faster response in the first ~50 minutes (Figure 45), but afterwards, the deswelling became slower than that of the pure PNIPAM. The p values were found <1 for practically all concentrations and for both steps revealing that the non-jamming behaviour of PNIPAM is not affected by the presence of CNTs. Meanwhile, the obtained time constants decreased with increasing CNT concentration. The effect of GO was inverse compared to the CNT: the GO@PNIPAM samples deswelled much faster than the pure gel and in a single step.

Figure 44. Semi-logarithmic plot of temperature shock (20 → 40 °C) induced shrinkage kinetics of pure PNIPAM gel (■), and CNT@PNIPAM (blue symbols) and GO@PNIPAM (red symbols) nanocomposite samples.

The 5-15 mg/g GO@PNIPAM samples behaved similarly to the pure PNIPAM in the first ~10 min (Figure 45). After this period the water was expelled faster by the pure PNIPAM but significantly slowed down at ~300 min. GO@PNIPAM continued to deswell steadily throughout the end of the observation. At 40 °C, only slightly above the VPTT of PNIPAM its hydrophilic - hydrophobic transition was slow and particularly at the beginning of the deswelling the hydrophilic GO facilitated the syneresis.
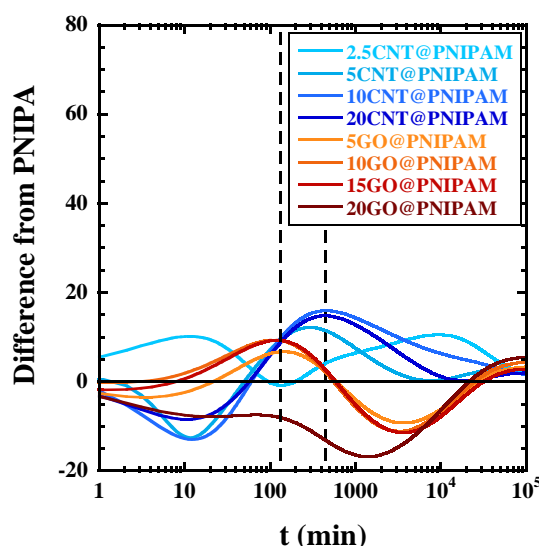
Figure 45. Shrinkage difference of CNT@PNIPAM (blue symbols) and GO@PNIPAM (red symbols): (Relative mass(nanocomposite)-Relative mass(PNIPAM)) obtained at 40°C as a function of time with respect to pure PNIPAM. Vertical dashed lines show the position of the maxima.

85

After fitting to Eq. 7, the *p* values of the pure PNIPAM gel and the CNT@PNIPAM samples were found <1 in all cases as well (all concentrations and for both steps), except 5CNT@PNIPAM, revealing that the non-jamming behaviour of PNIPAM was not affected by the presence of CNTs (Figure 46). Meanwhile, the obtained time constants decreased with increasing CNT concentration. For GO@PNIPAM systems the obtained time constants showed only a slight concentration dependence.

Figure 46. a) Time constants of the rate determining step and b) exponents of the fitted deswelling curves of CNT@PNIPAM and GO@PNIPAM systems at 40 °C.

However, the direct comparison of these time scales for the different systems is not straight forward. According to Figure 47, the total deswelling of the samples after the GO incorporation did not affect significantly the overall shrinkage-velocity, increasing GO-content caused only a slight slowing down, while the presence of small amount of CNTs hindered significantly the deswelling, which is in accordance with the assumed trend based on the time constant values.
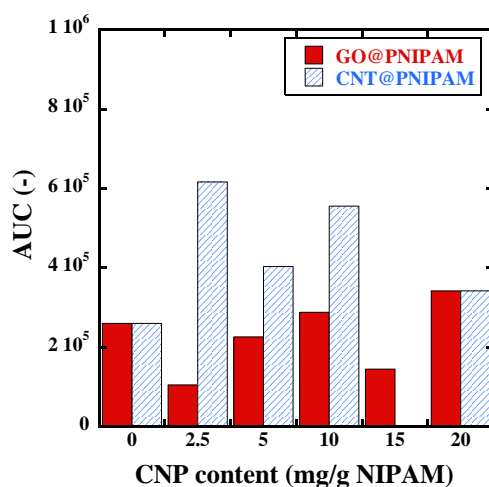
Figure 47. AUC values of the deswelling curves in Figure 44.

86

To obtain more information on the effect of hydrophilicity, shape and concentration, the RGO and post-reduced GO containing systems were studied as well (Figure 48, Figure 49).
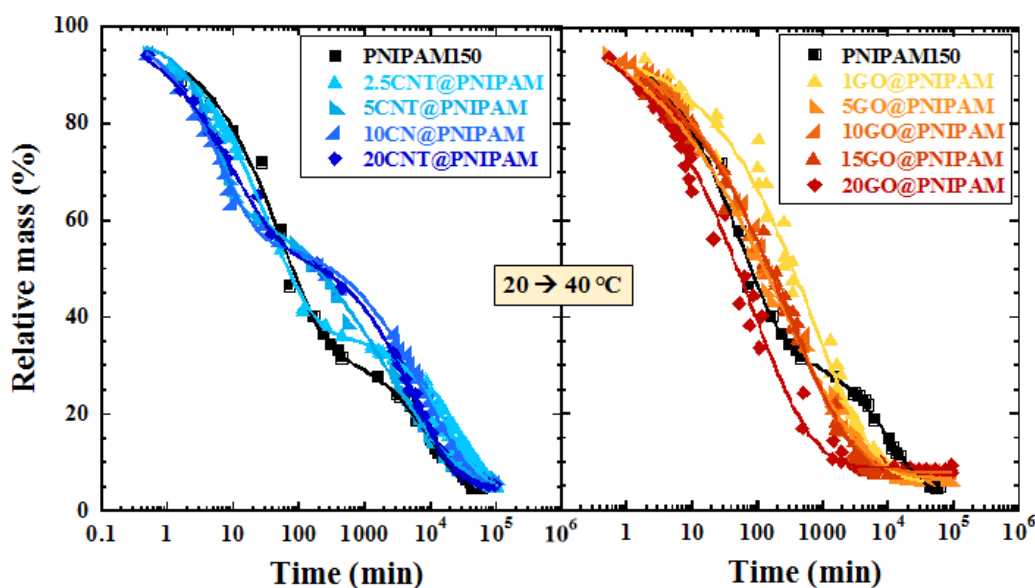

Figure 48. Semi-logarithmic plot of temperature shock (20➔ 40 °C) induced shrinkage kinetics of pure PNIPAM gel (■), and RGO@PNIPAM (green symbols) and (GO@PNIPAM)R (purple symbols) nanocomposite samples.

The 3RGO@PNIPAM showed a similar behaviour to the CNT@PNIPAM gels. Due to the hydrophobicity of the incorporated aggregates in the beginning of the shrinking process, the water expulsion was faster than in case of the pure PNIPAM, but it slowed down very suddenly. In case of the 11RGO@PNIPAM, the deswelling slowed down from the beginning of the process.

Figure 49. Shrinkage difference of RGO@PNIPAM (green symbols) and (GO@PNIPAM)R (purple symbols): (Relative mass(nanocomposite)-Relative mass(PNIPAM)) obtained at 40°C as a function of time with respect to pure PNIPAM.

The behaviour of the post-reduced systems looked very similar. At lower concentrations, the gels shrunk similarly to the pure gel, which was followed by a significant slowing down (Figure 48, Figure 49). At higher concentrations, the whole process was decelerated, a very stretched curve was observed.

The obtained time constants (Figure 50) decreased with increasing post-reduced GO concentration, similarly to the CNT@PNIPAM gels, however, the RGO@PNIPAM systems showed an opposite trend. Most of the fitted exponents were <1, which implies the lack of jamming and shows the complexity of the deswelling curve.
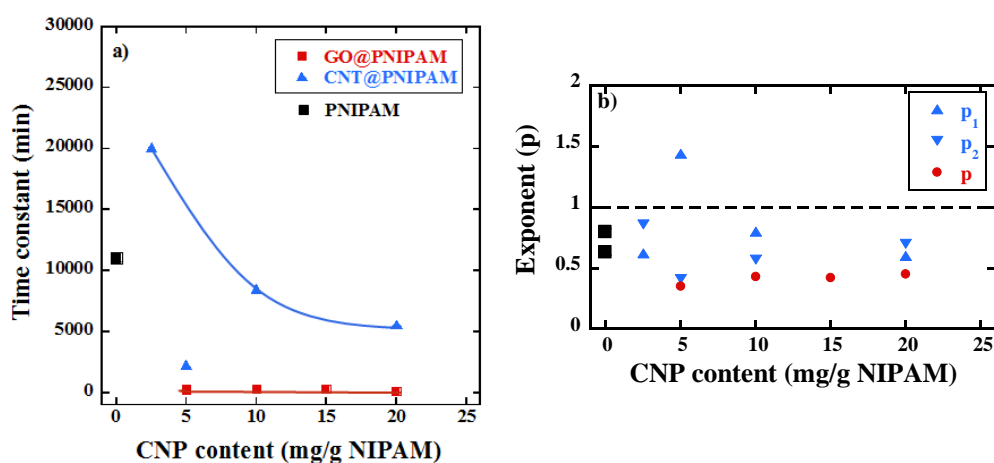

Figure 50. a) Time constants of the rate determining step and b) exponents of the fitted deswelling curves of RGO@PNIPAM and (GO@PNIPAM)R system at 40 °C.

The AUC values revealed (Figure 51) that the shrinkage velocity of the (GO@PNIPAM)R was proportional to the obtained time-constants. However, despite the experienced strong concentration dependence of the time constants of the RGO@PNIPAM systems, there was no significant difference in the integrated values, so the overall shrinkage velocity stayed similar.
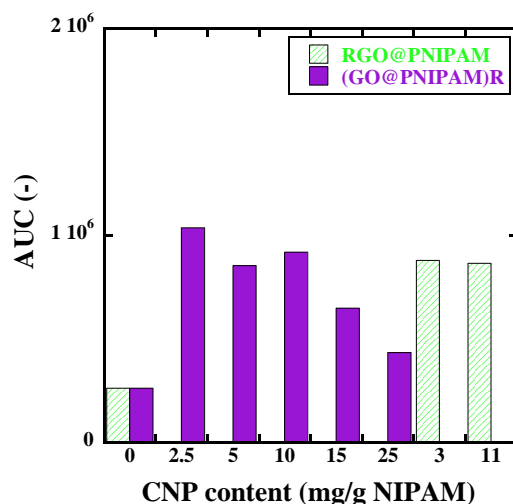
Figure 51. AUC values of the deswelling curves in Figure 48.

Composite gels at 50 °C

The thermal response of the systems changed remarkably when the temperature gradient was increased (20→50 °C, Figure 52). As it could be seen in Figure 40, the pure PNIPAM gels behave radically differently as well. The overall process became much faster in case of the PNIPAM150, in accordance with previous observations [41], which polymer network is the base of the composite materials as well. However, the unloaded and loaded PNIPAM150 gels in the course of deswelling at 50 °C showed a very different shape (Figure 52).
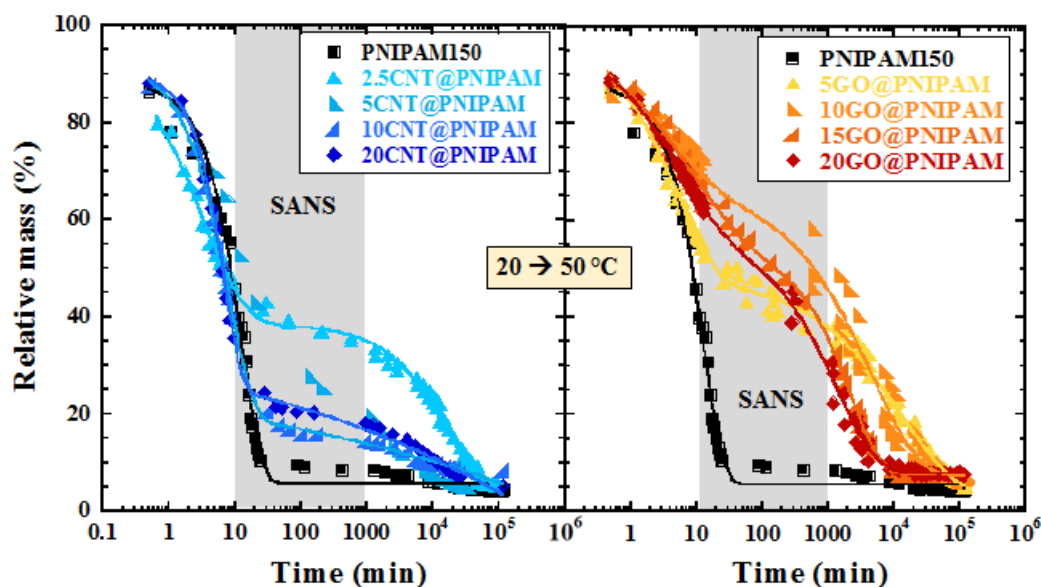
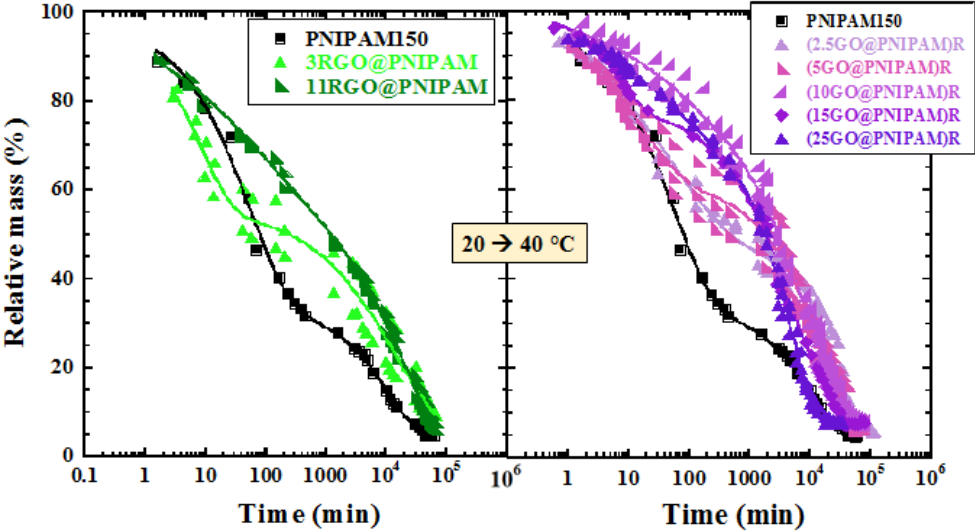*Figure 52. Semi-logarithmic plot of temperature shock (20 → 50 °C) induced shrinkage kinetics of pure PNIPAM gel (■), and CNT@PNIPAM (blue symbols) and GO@PNIPAM (red symbols) nanocomposite samples.*

Compared to the curves measured at the smaller temperature jump, the CNT incorporation resulted in a slightly faster response, but as the shrinkage of the PNIPAM was also faster than at 40 °C, the accelerating effect of the CNT played a role only in the first ~10 minutes (Figure 53).
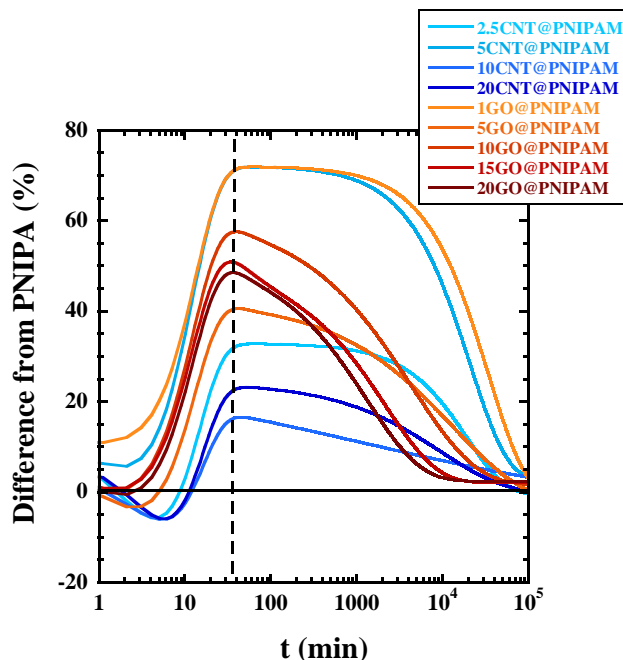
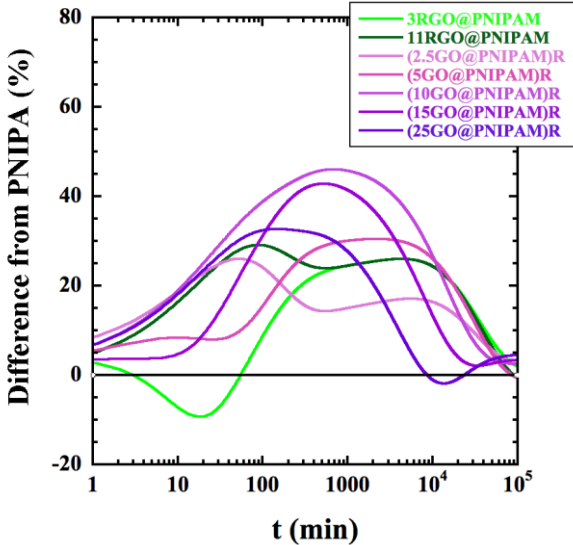*Figure 53. Shrinkage difference of CNT@PNIPAM (blue symbols) and GO@PNIPAM (red symbols): (Relative mass(nanocomposite)-Relative mass(PNIPAM)) obtained at 50 °C as a function of time with respect to pure PNIPAM. Vertical dashed lines show the position of the maxima.*

Their slowing effect was also more pronounced in the second part of the deswelling than it was seen in case of the 20 → 40 °C temperature jump. The more CNT we had the more time was required for the proper orientation of the polymer chains and the CNTs and thus for the relaxation of the CNT@PNIPAM systems (Figure 54).

The effect of GO incorporation had a remarkably different consequence on the responsive behaviour of the nanocomposites, however, it also consisted of 2 distinct steps. The presence of the hydrophilic GO sheets slowed down the temperature response from the beginning of the process. This may be related to the interaction between the GO platelets and the polymer chains. The maximum deviation in Figure 53 appeared practically at the same time (at ~30 min) for all the samples, i.e., when the pure gel already reached its final swelling ratio.
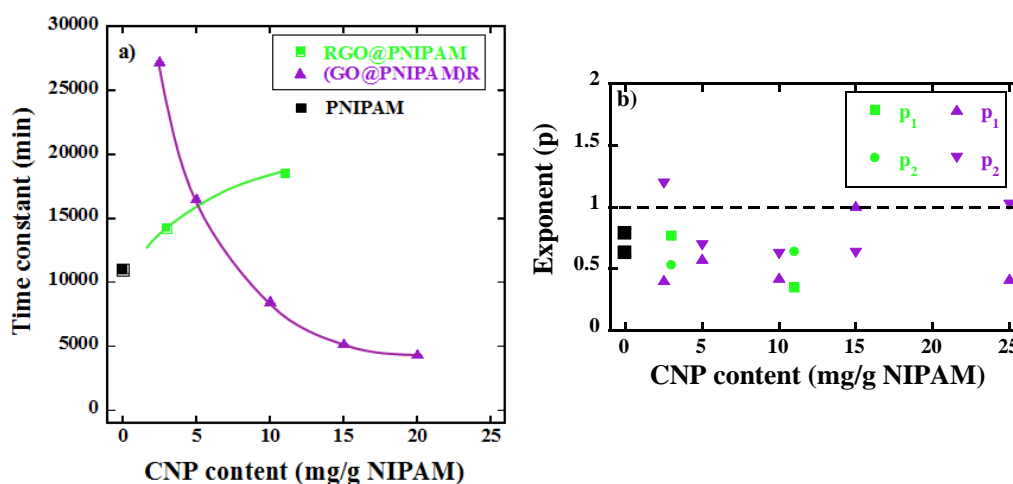
90

Figure 54. Fitted Time constants of the rate determining step and exponents of the fitted deswelling curves of CNT@PNIPAM and GO@PNIPAM systems at 50 °C.

The curves were fitted to Eq. 7 in case of the higher temperature jump as well (Figure 54). t_2 was found to increase with the CNT content indicating that higher CNT content hindered more the relaxation of the system. The obtained p_1 values for CNT@PNIPAM systems, similarly to the pure PNIPAM, were found to be higher than 1, reflecting jamming, whereas p_2 was found to be less than unity. In case of the GO@PNIPAM gels the fitted parameter $p_1<1$ implies that no jamming occurs in these systems. On the contrary to CNT@PNIPAM, t_2 decreased with the GO content (Figure 54), i.e., the smallest amount of GO hindered the deswelling the most. The overall shrinking process was characterized again with the AUC values (Figure 55). The increasing CNT or GO content showed a slight increase in the shrinking velocity, as it was seen from the time constant values as well.
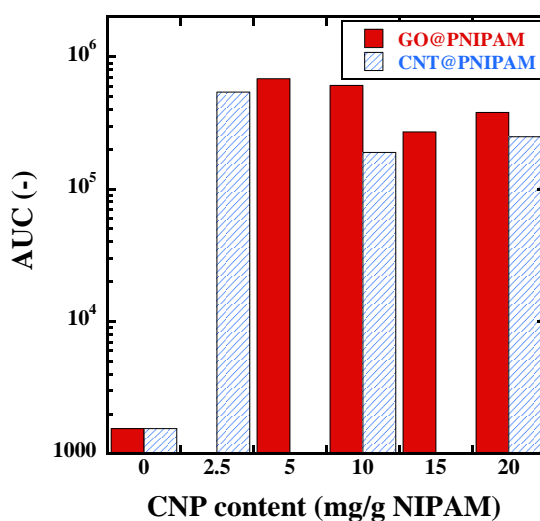
Figure 55. AUC values of the deswelling curves in Figure 52.

91

In case of RGO and post-reduced GO containing samples during the 20 → 50 °C jump (Figure 56) both systems showed a two-step deswelling curve. As we saw before, the behaviour of the RGO@PNIPAM gel was very similar to that of the CNT@PNIPAM systems. The shrinkage of the post-reduced samples was more hindered; the water loss in the first step was very low.
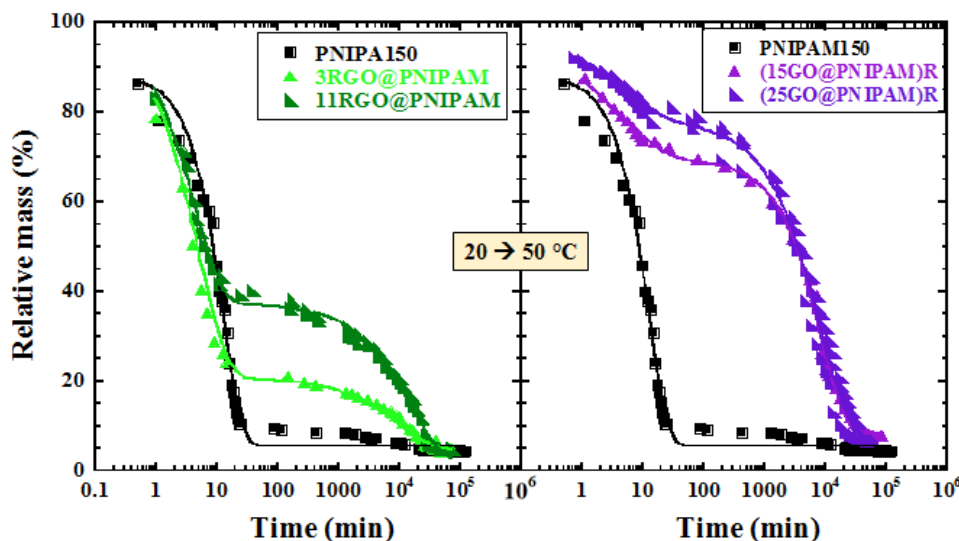
Figure 56. Semi-logarithmic plot of temperature shock (20→ 50 °C) induced shrinkage kinetics of pure PNIPAM gel (■), and RGO@PNIPAM (green symbols) and (GO@PNIPAM)R (purple symbols) nanocomposite samples.

Figure 57 shows the discrepancy of these curves from the pure PNIPAM150 gel.
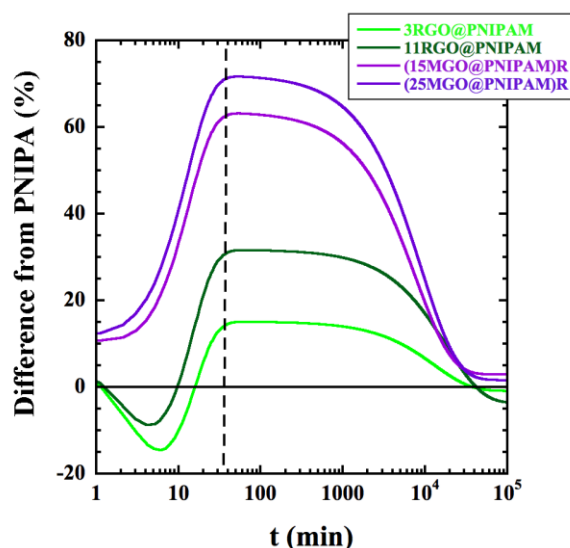
Figure 57. Shrinkage difference of RGO@PNIPAM (green symbols) and (GO@PNIPAM)R (purple symbols): (Relative mass(nanocomposite)-Relative mass(PNIPAM)) obtained at 50°C as a function of time with respect to pure PNIPAM. Vertical dashed lines show the position of the maxima.

None of the measured curves showed jamming (Figure 58). The RGO-content speeded up the water expulsion in the beginning of the shrinkage again and then it caused a significant slowing. The increasing amount of RGO load slowed the deswelling process more. It is easy to notice that the shrinking of the post-reduced systems was slower than that of all the other previously investigated systems. Upon concentration change, there was no significant difference in the rate determining time constant or in the overall shrinkage either (Figure 58, Figure 59).
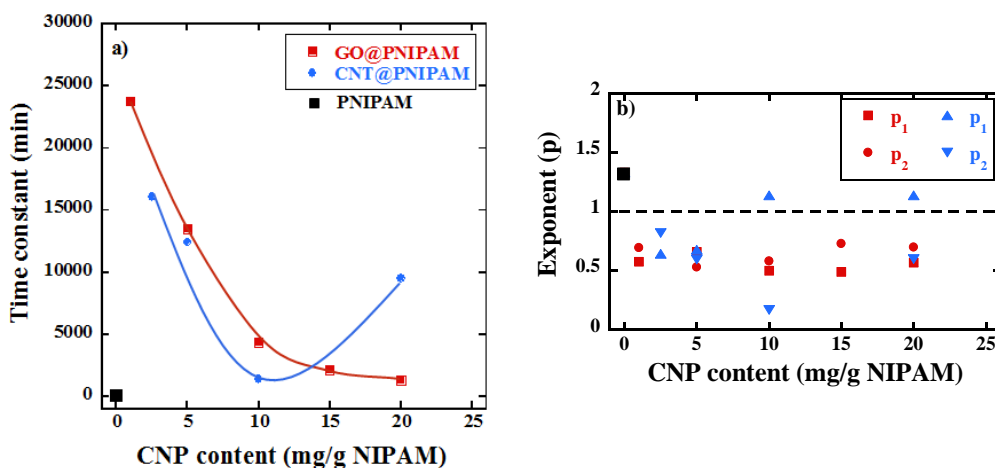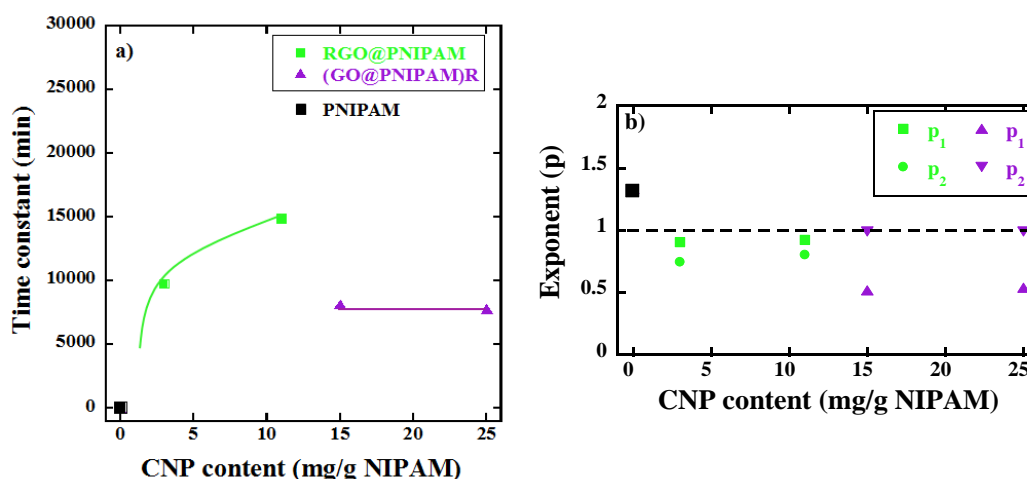

Figure 58. a)Time constants of the rate determining step and b) exponents of the fitted deswelling curves of RGO@PNIPAM and (GO@PNIPAM)R systems at 50 °C.
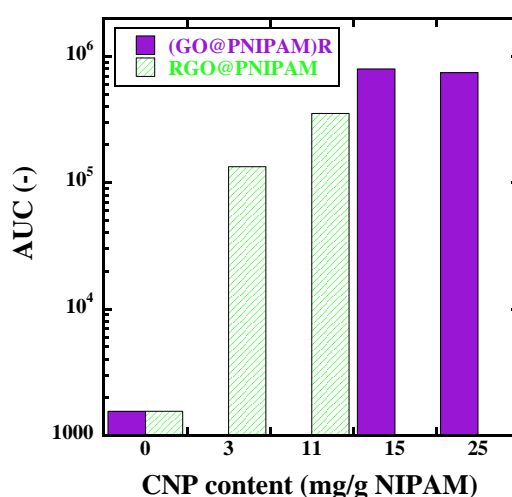
Figure 59. AUC values of the deswelling curves in Figure 56.

In-situ SANS measurements were performed to gain insight into the structural reorganisation occurring during the first 1200 min of the deswelling of GO@PNIPAM and CNT@PNIPAM systems during the 20 → 50 °C jump. Grey shaded areas in Figure 52 show the time window

on these measurements compared to the total deswelling time. As was shown earlier SANS measurements can deliver information from the polymer matrix only, whereas CNPs remain practically invisible. Figure 60a and b show the typical evolution of the scattering signal during the kinetic measurement. Owing to the long counting times needed for the data acquisition the time-resolution of these measurements was 18 min, which means that, unfortunately, the first, fast decay step remains unexplored. Obtained curves were fitted to Eq. 9 to quantify the differences and to determine the network inhomogeneity correlation length (Θ) of the systems. The VPT increased significantly the values of Θ. The increase of Θ can be
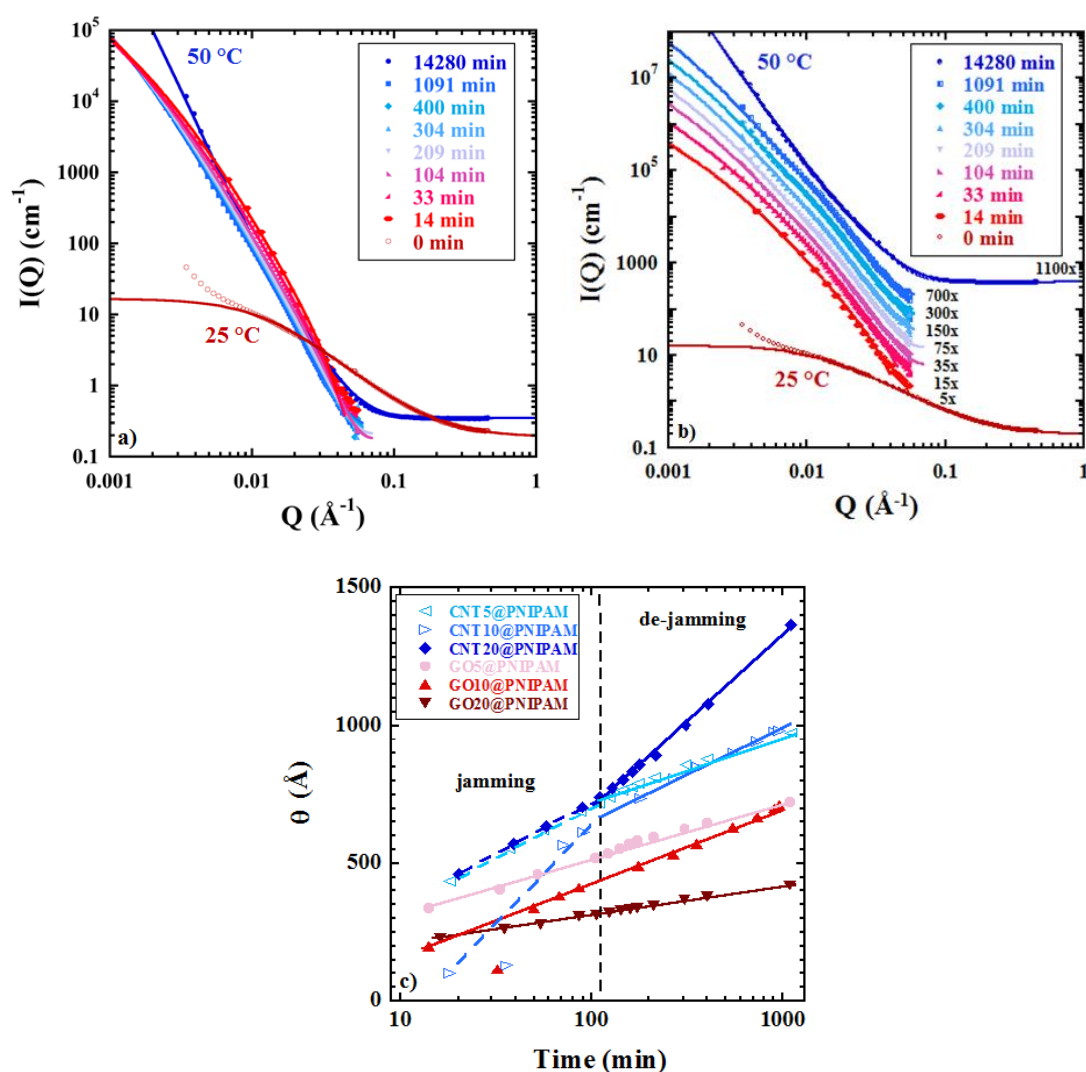
Figure 60. a) Scattering signals after background corrections of 5GO@PNIPAM gel at 25 ˚C (red) and after different amount of times at 50 ˚C (blue) with the corresponding fits and b) the same curves are shifted vertically for clarity. The used factors are shown in the figure. c) Time dependence of network inhomogeneity correlation length values upon shrinkage. Solid lines are guides for the eye.

explained by the clumping of the polymer chains. The time evolution of Θ for the nanocomposite systems is presented in Figure 60c. In case of the GO containing composites, the increment of the correlation length was continuous over the observed time scale indicating that the structural evolution was stationary. On the other hand, in CNT@PNIPAM systems two distinct regimes could be observed and the crossover time corresponded perfectly to the beginning of the second decay step (Figure 52), i.e., the "de-jamming".

5.5.3.2.   *Interpretation of the kinetic results*

When the VPT occurs at 50 °C in pure PNIPAM150 gel, the hydrophilic − hydrophobic transition results in an abrupt collision of the polymer chains, which hinders their movement, therefore, jamming can occur. The increasing cross-links density makes this process much slower. The lower final temperature value results in a smaller driving force, which slows down the shrinkage and makes the gel avoid the jamming as well.

The hydrophobic character of the CNTs fosters the water expulsion in the early stages of the process as due to the increased hydrophobicity; the water expulsion might become energetically more favourable. The CNT-aggregates act also as spacers in the gel, presenting a physical obstacle for the shrinkage and thus obstructing the motion of the polymer chains. The hindering effect of the higher CNT concentration is stronger and as the deswelling of the gel at 50 °C is governed by a jamming process a more sudden response provokes a stronger hindering on longer time scales. The second part of the deswelling (t > 20 min) can be described by a stretched exponential function ($p_2 < 1$) in all cases. It suggests that this slow process, at 50 °C it can be called the "de-jamming", is not anymore governed by the previously occurred jamming. Instead, it can be illustrated by the presence of multiple processes with relatively similar, but distinct time scales that can be attributed to a slow reorganization of the polymer chains and CNT aggregates.

GO has a 2-dimensional shape and a hydrophilic character, which facilitates the water expulsion at 40 °C, while at 50 °C, in the first minutes the deswelling kinetics is seemingly not affected by their presence. However, from ~3 min a significant slowing down/deceleration can be observed, as was shown above. The structure of the GO containing composites is different from that of the CNT@PNIPAM systems, and as GO sheets have higher surface area than CNTs, they give the possibility to more polymer chains to stick to their surface during the shrinkage. The covered surface hinders the water expulsion by the hydrophilic particles at the early stage, because a high fraction of the polymer chains is stuck to the GO surface this way obstructing the effect of hydrophilicity. It also means that when the polymer chains are

moving during deswelling, they have to pull the GO with them, the chains may try to move the platelets to the opposite direction, which causes a significantly slower deswelling. The similar process can occur in case of the CNT@PNIPAM, but the effect is less pronounced, because of the lower number of attached polymer chains. The decrease of the effective GO concentration beyond its percolation threshold might facilitate the movement of the grown polymer blobs around the stacked GO platelets because the polymer chains stick to only one side of the platelet that can allow the macroscopic gel to deswell in a faster way at higher GO concentrations. This very slow motion of the polymer chains avoids jamming for the GO@PNIPAM systems under all circumstances.

The results from RGO@PNIPAM and (GO@PNIPAM)R systems can shed light on the effect of hydrophilicity and available surface area. The RGO@PNIPAM gels have aggregates, which limit the available surface. As a result, their behaviour is very similar to the CNT@PNIPAM composites. On the other hand, when GO was reduced inside the polymer matrix the available surface area did not change significantly, but the hydrophilicity of the sheets was strongly modified. Due to these properties, the deswelling of the (GO@PNIPAM)R systems were slower than any other studied material. The deswelling rate is inversely proportional to the concentration during the 20 $\rightarrow$ 40 °C jump, which means that the effect of the lower available surface area beyond the percolation threshold is conserved after the reduction process. Alternatively, in case of the 20 $\rightarrow$ 50 °C jump, there is no significant effect of concentration, because without the facilitating effect of the hydrophilicity of the GO platelets, the movement of the polymer chains is so strongly hindered, that it will determine the shrinking rate alone.

6.   Conclusions

The goal of my PhD work was to investigate systematically the effect of shape and surface chemistry of CNPs incorporated into PNIPAM hydrogel systems. I tried to shed light on the formed interactions and their effect on the character of the constructed hybrids. I prepared CNT, GO and RGO containing composite PNIPAM gels and characterised them both on the macro- and the nanoscale size range. An important part of my work was focusing on the understanding of the responsive behaviour of the prepared composites.

The CNPs studied with various shape and surface chemistry had a different effect on the equilibrium properties and kinetics of the prepared composite systems but did not influence the local dynamics below the VPTT. The CNT aggregates formed in the aqueous system prior the gel synthesis. The presence of the aggregates resulted in an inhomogeneous distribution. While the CNT-content did not significantly influence the macroscopic properties, GO incorporation reduced the swelling capacity and increased the elastic modulus of the gels. This is due to the build-up of an interpenetrating GO network, which changes the architecture of the polymer gel: the polymer matrix forms a hypernode-structure following chain nucleation at the surface of the GO.

The structural change of the polymer matrix can be followed by its static polymer–polymer correlation length measured by SANS. The polymer-polymer correlation length decreases upon CNP incorporation. The decrease of ξ upon incorporation of GO reflected the structural modification of the nanoparticle and was a result of the formation of a hypernodal structure developing around the platelets. The effect of GO was not proportional to its concentration in the gel matrix, as percolation occurs between 5 and 10 mg/ g NIPAM. As at higher concentration GO particles may sterically hinder each other, i.e. their effective concentration is smaller than the nominal value, the effect becomes not proportional to the nominal concentration. In the case of the CNT@PNIPAM systems increasing concentration results in a slight decrease in ξ.

The structure of the incorporated nanoparticles could be followed by SAXS because in this method the signal is dominated by the CNPs. It was found that the morphology of the GO nanoparticles and CNT aggregates was approximately the same already in the suspension state, prior to gelation, and this morphology probably depended on the physicochemical properties of GO, i.e., its interaction with the solvent.

The reduction of the GO can be carried out efficiently with ascorbic acid even at room temperature. Since this method does not modify the PNIPAM matrix based on the performed

measurements (mechanical and swelling properties, microscopic structure), it was found to be an efficient method for the reduction of the GO after the composite synthesis. RGO containing composite hydrogels were prepared by two different methods: i) by incorporating RGO directly into the polymer matrix; ii) applying a post-reduction treatment on GO@PNIPAM nanocomposites. The effect of the CNP concentration as well as the preparation method was investigated. Direct incorporation of RGO is strongly limited by its reduced hydrophilicity, i.e., only a smaller concentration and a less than uniform distribution were achieved. The more homogeneous distribution of the hydrophilic GO particles even at higher CNP content was conserved in the post-synthesis reduction. We found that the aggregation tendency of RGO that was reduced prior to the polymerisation resulted in a small structural modification in the nanocomposites. Similarly to the CNT@PNIPAM gels, the swelling and mechanical properties remained almost unchanged compared to the pure PNIPAM gel, and the change in ξ remained similar to that of the CNT@PNIPAM systems. By contrast, when GO was reduced within the gel matrix, both structural and macroscopic properties showed a strong variation in the concentration of the CNPs. This process did not influence the pure polymer matrix, so all observed differences can be attributed to the change in the CNPs.

Thermogravimetric and NMR observations revealed strong interactions between GO and the polymer matrix, which are practically unchanged after the post-reduction treatment. Our results, however, show no clear evidence of covalent bonds. The damaged graphene structure may offer a niche for the polymer segments growing during the polymerisation in the confinement created by the carbon sheets. Further evidence is needed to reveal the real reason of the enhanced interactions. At the same time, RGO interacts only weakly when incorporated directly into the gel. The vicinity of the PNIPAM carbonyl groups is more rigid in the GO@PNIPAM samples than in the pure PNIPAM, and this is not affected by the post-reduction. On the contrary, the mobility of the polymer in the same environment increases when RGO is incorporated directly into the polymer gel. This impliesg a softening effect.

Based on the results from different length scales the structure of the CNP containing systems was proposed.

In addition to the structure, investigation of dynamical properties of the systems is inevitable for any applications. The hydrodynamic properties of the network chains measured by neutron spin-echo spectroscopy did not change upon CNP incorporation, which suggests that the mobility of the polymer chains was not influenced by the nanoparticle-content.

Alternatively, both microscopic and macroscopic observations show that the kinetics of the temperature response of the systems depend strongly both on the type and concentration of the CNPs. Moreover, it was found that the applied temperature gradient also affects the response of the systems. The kinetics of the deswelling was found to be altered by the shape and the hydrophilicity/hydrophobicity of the incorporated nanoparticles.

In the composite gels, the GO mediates the evacuation of water in the high temperature collapsed state, which, in pure PNIPAM, would otherwise remain trapped in the network in the form of microscopic droplets. This implies that the collapsed PNIPAM chains are oriented by the GO surfaces. In the post-reduced GO containing systems, which have a similar structure, the hydrophobic particles hindered the water expulsion, prolonging the water expulsion. The RGO and CNT aggregates, however, accelerated the beginning of the deswelling process and slowed down the second part of it.

The presented results show that the incorporated graphene derivates improve the mechanical properties of the PNIPAM gel. Both their chemistry and their concentration are promising means for tuning the thermal responsivity, thereby broadening the fields of application of such nanocomposite systems.

7.   References

[1]   N.K. Singh, D.S. Lee, In situ gelling pH and temperature-sensitive biodegradable block copolymer hydrogels for drug delivery, J. Control. Release. 193 (2014) 214–227. doi:10.1016/j.jconrel.2014.04.056.

[2]   J. Kopecek, Hydrogel biomaterials: a smart future?, Biomaterials. 28 (2007) 5185–5192. doi:10.1016/j.biomaterials.2007.07.044.

[3]   E.M. Ahmed, Hydrogel: Preparation, characterization, and applications, J. Adv. Res. 6 (2013) 105–121. doi:10.1016/j.jare.2013.07.006.

[4]   L.Z. Zhao, C.H. Zhou, J. Wang, D.S. Tong, W.H. Yu, H. Wang, Recent advances in clay mineral-containing nanocomposite hydrogels, Soft Matter. 11 (2015) 9229–9246. doi:10.1039/C5SM01277E.

[5]   S.K.H. Gulrez, S. Al-Assaf, G.O. Phillips, Hydrogels : Methods of Preparation , Characterisation and Applications, Prog. Mol. Environ. Bioeng. 51 (2003) 117–150. doi:10.1016/j.jvs.2009.12.028.

[6]   M. Rubinstein, R.H. Colby, Polymer Physics, Oxford, 2003.

[7]   A. Szilágyi, Hőmérsékletérzékeny polimer gélek – Az elmélettől a gyakorlati alkalmazásig (PhD Thesis), Budapesti Műszaki és Gazdaságtudományi Egyetem, 2005.

[8]   E. Geissler, A.-M. Hecht, F. Horkay, M. Zrínyi, Compressional modulus of swollen polyacrylamide networks, Macromolecules. 21 (1988) 2594–2599. doi:10.1021/ma00186a048.

[9]   T. Tanaka, Collapse of gels and the critical endpoint, Phys. Rev. Lett. 40 (1978) 820–823. doi:10.1103/PhysRevLett.40.820.

[10]   J.H. Bradbury, M.D. Fenn, I. Gosney, the Change of Volume Associated With the Helix-Coil Transition in Poly-Gamma-Benzyl-L-Glutamate., J. Mol. Biol. 11 (1965) 137–140. doi:10.1016/S0022-2836(65)80179-6.

[11]   M. Heskins, J.E. Guillet, Solution Properties of Poly(N-isopropylacrylamide), J. Macromol. Sci. Part A Pure Appl. Chem. 2 (1968) 1441–1455. doi:10.1080/10601326808051910.

[12]   J. Ricka, T. Tanaka, Swelling of ionic gels: quantitative performance of the Donnan theory, Macromolecules. 17 (1984) 2916–2921. doi:10.1021/ma00142a081.

[13]   Y.H. Bae, T. Okano, S. Wan Kim, Temperature dependence of swelling of crosslinked poly(N,N′-alkyl substituted acrylamides) in water, J. Polym. Sci. Part B Polym. Phys. 28 (1990) 923–936. doi:10.1002/polb.1990.090280609.

[14]   Y. Hirokawa, T. Tanaka, Volume phase transition in a nonionic gel, J. Chem. Phys. 81 (1984) 6379. doi:10.1063/1.447548.

[15]   S. Nayak, L. Andrew Lyon, Soft nanotechnology with soft nanoparticles, Angew. Chemie - Int. Ed. 44 (2005) 7686–7708. doi:10.1002/anie.200501321.

[16]   Z. Hu, X. Zhang, Y. Li, Synthesis and application of modulated polymer gels, Science. 269 (1995) 525–527. doi:10.1126/science.269.5223.525.

[17]   M. Zrínyi, Intelligent polymer gels controlled by magnetic fields, Colloid Polym. Sci. 278 (2000) 98–103. doi:10.1007/s003960050017.

[18]   S. Reinicke, S. Döhler, S. Tea, M. Krekhova, R. Messing, A.M. Schmidt, H. Schmalz, Magneto-responsive hydrogels based on maghemite/triblock terpolymer hybrid micelles, Soft Matter. 6 (2010) 2760. doi:10.1039/c000943a.

[19]   D.C. Coughlan, O.I. Corrigan, Drug-polymer interactions and their effect on thermoresponsive poly(N-isopropylacrylamide) drug delivery systems, Int. J. Pharm. 313 (2006) 163–174. doi:10.1016/j.ijpharm.2006.02.005.

[20]   A.K. Bajpai, S.K. Shukla, S. Bhanu, S. Kankane, Responsive polymers in controlled drug delivery, Prog. Polym. Sci. 33 (2008) 1088–1118. doi:10.1016/j.progpolymsci.2008.07.005.

[21]   R. Yoshida, K. Sakai, T. Okano, Y. Sakurai, Y.H. Bae, S.W. Kim, Surface-modulated skin

layers of thermal responsive hydrogels as on-off switches: I. Drug release, J. Biomater. Sci. Polym. Ed. 3 (1991) 155–162. doi:10.1163/156856292X00150.

[22] R. Yoshida, K. Sakai, T. Okano, Y. Sakurai, Surface-modulated skin layers of thermal responsive hydrogels as on-off switches: II. Drug permeation, J. Biomater. Sci. Polym. Edn. 3 (1992) 243–252. doi:10.1163/156856292X00150.

[23] A. Kumar, A. Srivastava, I.Y. Galaev, B. Mattiasson, Smart polymers: Physical forms and bioengineering applications, Prog. Polym. Sci. 32 (2007) 1205–1237. doi:10.1016/j.progpolymsci.2007.05.003.

[24] Z.B. Hu, Y.Y. Chen, C.J. Wang, Y.D. Zheng, Y. Li, Polymer gels with engineered environmentally responsive surface patterns, Nature. 393 (1998) 149–152. doi:Doi 10.1038/30205.

[25] L. Ionov, Hydrogel-based actuators: possibilities and limitations, Mater. Today. 17 (2014) 494–503. doi:10.1016/j.mattod.2014.07.002.

[26] P. Kim, L.D. Zarzar, X. He, A. Grinthal, J. Aizenberg, Hydrogel-actuated integrated responsive systems (HAIRS): Moving towards adaptive materials, Curr. Opin. Solid State Mater. Sci. 15 (2011) 236–245. doi:10.1016/j.cossms.2011.05.004.

[27] S. Sugiura, K. Sumaru, K. Ohi, K. Hiroki, T. Takagi, T. Kanamori, Photoresponsive polymer gel microvalves controlled by local light irradiation, Sensors Actuators A Phys. 140 (2007) 176–184. doi:10.1016/j.sna.2007.06.024.

[28] M.E. Harmon, M. Tang, C.W. Frank, A microfluidic actuator based on thermoresponsive hydrogels, Polymer. 44 (2003) 4547–4556. doi:10.1016/S0032-3861(03)00463-4.

[29] M. Andersson, A. Axelsson, G. Zacchi, Swelling kinetics of poly(N-isopropylacrylamide) gel, 50 (1998) 273–281. doi:10.1016/S0168-3659(97)00151-X.

[30] M. Annaka, Y. Ogata, T. Nakahira, Swelling Behavior of Covalently Cross-Linked Gellan Gels, J. Phys. Chem. B. 104 (2000) 6755–6760. doi:10.1021/jp0001539.

[31] N. Bouklas, R. Huang, Swelling kinetics of polymer gels: comparison of linear and nonlinear theories, Soft Matter. 8 (2012) 8194. doi:10.1039/c2sm25467k.

[32] T.R.C. Boyde, Swelling and contraction aqueous solutions of polyacrylamide gel slabs in aqueous solutions, J. Chromatogr. 219–230 (1976). doi:10.1016/S0021-9673(00)89737-X.

[33] T. Çaykara, S. Kiper, G. Demirel, Network parameters and volume phase transition behavior of poly(N-isopropylacrylamide) hydrogels, J. Appl. Polym. Sci. 101 (2006) 1756–1762. doi:10.1002/app.23513.

[34] W. Fan, X. Fan, W. Tian, X. Zhang, G. Wang, W. Zhang, Y. Bai, X. Zhu, Phase transition dynamics and mechanism for backbone-thermoresponsive hyperbranched polyethers, Polym. Chem. 5 (2014) 4022. doi:10.1039/c4py00155a.

[35] R. Gemeinhart, C. Guo, Fast swelling hydrogel systems, Reflexive Polym. Hydrogels Underst. Des. Fast Responsive Polym. Syst. (2004) 245–257. doi:doi:10.1201/9780203485354.ch13.

[36] P. Guo, H. Li, W. Ren, J. Zhu, F. Xiao, S. Xu, J. Wang, Unusual thermo-responsive behaviors of poly(NIPAM-co-AM)/PEG/PTA composite hydrogels, Mater. Lett. 143 (2015) 24–26. doi:10.1016/j.matlet.2014.12.074.

[37] A.R. Khare, N.A. Peppas, Swelling/deswelling of anionic copolymer gels, Biomaterials. 16 (1995) 559–567. doi:10.1016/0142-9612(95)91130-Q.

[38] Y. Li, T. Tanaka, Kinetics of swelling and shrinking of gels, J. Chem. Phys. 92 (1990) 1365. doi:10.1063/1.458148.

[39] X. Ma, Y. Cui, X. Zhao, S. Zheng, X. Tang, Different deswelling behavior of temperature-sensitive microgels of poly(N-isopropylacrylamide) crosslinked by polyethyleneglycol dimethacrylates., J. Colloid Interface Sci. 276 (2004) 53–9. doi:10.1016/j.jcis.2004.03.023.

[40] K. Makino, J. Hiyoshi, H. Ohshima, Kinetics of swelling and shrinking of poly (N-isopropylacrylamide) hydrogels at different temperatures, Colloids Surfaces B Biointerfaces.

19 (2000) 197–204. doi:10.1016/S0927-7765(00)00155-7.

[41] E. Sato Matsuo, T. Tanaka, Kinetics of discontinuous volume–phase transition of gels, J. Chem. Phys. 89 (1988) 1695. doi:10.1063/1.455115.

[42] K. Otake, H. Inomata, M. Konno, S. Saito, Thermal analysis of the volume phase transition with N-isopropylacrylamide gels, Macromolecules. 23 (1990) 283–289. doi:10.1021/ma00203a049.

[43] A. Suzuki, T. Tanaka, Phase transition in polymer gels induced by visible light, Nature. 346 (1990) 345–347. doi:10.1038/346345a0.

[44] H. Tajima, Y. Yoshida, K. Yamagiwa, Experimental study of swelling and shrinking kinetics of spherical poly(N,N-diethylacrylamide) gel with continuous phase transition, Polymer. 52 (2011) 732–738. doi:10.1016/j.polymer.2010.12.029.

[45] T. Tanaka, D.J. Fillmore, Kinetics of swelling of gels, J.Chem. Phys. 70 (1979) 1214–1218. doi:10.1021/ma00161a029.

[46] X.Z. Zhang, F.J. Wang, C.C. Chu, Thermoresponsive hydrogel with rapid response dynamics, J. Mater. Sci. Mater. Med. 14 (2003) 451–455. doi:10.1023/A:1023219019500.

[47] H. Tajima, F. Sato, K. Yamagiwa, Effect of Hydrophobic Pollution on Response of Thermo-Sensitive Hydrogel, Chemosensors. 1 (2013) 21–32. doi:10.3390/chemosensors1030021.

[48] J. Wang, D. Gan, L.A. Lyon, M.A. El-Sayed, Temperature-jump investigations of the kinetics of hydrogel nanoparticle volume phase transitions, J. Am. Chem. Soc. 123 (2001) 11284–11289. doi:10.1021/ja016610w.

[49] S. V Ghugare, E. Chiessi, M.T. Telling, A. Deriu, Y. Gerelli, J. Wuttke, G. Paradossi, Structure and dynamics of a thermoresponsive microgel around its volume phase transition temperature, J Phys Chem B. 114 (2010) 10285–10293. doi:10.1021/jp100962p.

[50] A. Srivastava, E. Jain, A. Kumar, The physical characterization of supermacroporous poly(N-isopropylacrylamide) cryogel: Mechanical strength and swelling/de-swelling kinetics, Mater. Sci. Eng. A. 464 (2007) 93–100. doi:10.1016/j.msea.2007.03.057.

[51] W. Xue, S. Champ, M.B. Huglin, T.G.J. Jones, Rapid swelling and deswelling in cryogels of crosslinked poly(N-isopropylacrylamide-co-acrylic), Eur. Polym. J. 40 (2004) 703–712. doi:10.1016/j.eurpolymj.2003.10.021.

[52] E. Manek, A. Domján, J. Madarász, K. László, Interactions in aromatic probe molecule loaded poly(N-isopropylacrylamide) hydrogels and implications for drug delivery, Eur. Polym. J. 68 (2015) 657–664. doi:10.1016/j.eurpolymj.2015.03.043.

[53] A. Domján, E. Manek, E. Geissler, K. László, Host-guest interactions in poly(N-isopropylacrylamide) hydrogel seen by one- and two-dimensional 1H CRAMPS solid-state NMR spectroscopy, Macromolecules. 46 (2013) 3118–3124. doi:10.1021/ma400295a.

[54] K. Kosik, E. Wilk, E. Geissler, K. László, Interaction of phenols with thermo-responsive hydrogels, Colloids Surfaces A Physicochem. Eng. Asp. 319 (2008) 159–164. doi:10.1016/j.colsurfa.2007.07.022.

[55] J. Bastide, S.J. Candau, Structure of gels a investigated by means of static scattering techniques, in: J.P. Cohen Addad (Ed.), Phys. Prop. Polym. Gels, John Wiley & Sons Ltd., West Sussex, 1996.

[56] E. Geissler, F. Horkay, A.-M. Hecht, Structure and thermodynamics of flexible polymer gels, J. Chem. Phys. 100 (1994) 8418–8424. doi:10.1063/1.466789.

[57] F. Zernike, L.S. Ornstein, 17(II), 793, KNAW Proc. 17 (1914) 793.

[58] K. Depa, A. Strachota, M. Šlouf, J. Hromádková, Fast temperature-responsive nanocomposite PNIPAM hydrogels with controlled pore wall thickness: Force and rate of T-response, Eur. Polym. J. 48 (2012) 1997–2007. doi:10.1016/j.eurpolymj.2012.09.007.

[59] H.G. Schild, Poly (N-Isopropylacrylamide): Experiment , Theory and Application, Prog. Polym. Sci. 17 (1992) 163–249. doi:10.1016/0079-6700(92)90023-R.

[60]   P.E. JagadeeshBabu, R. Suresh Kumar, B. Maheswari, Synthesis and characterization of temperature sensitive P-NIPAM macro/micro hydrogels, Colloids Surfaces A Physicochem. Eng. Asp. 384 (2011) 466–472. doi:10.1016/j.colsurfa.2011.05.004.

[61]   P.C. Thomas, B.H. Cipriano, S.R. Raghavan, Nanoparticle-crosslinked hydrogels as a class of efficient materials for separation and ion exchange, Soft Matter. 7 (2011) 8192–8197. doi:10.1039/c1sm05369h.

[62]   Y. Tamai, H. Tanaka, K. Nakanishi, Molecular Dynamics Study of Polymer−Water Interaction in Hydrogels. 1. Hydrogen-Bond Structure, Macromolecules. 29 (1996) 6750–6760. doi:10.1021/ma951635z.

[63]   P.L. Privalov, S.J. Gill, The hydrophobic effect: a reappraisal, Pure Appl. Chem. 61 (1989) 1097–1104. doi:10.1351/pac198961061097.

[64]   T.M. Letcher, B.C. Bricknell, Calorimetric Investigation of the Interactions of Some Hydrogen-Bonded Systems at 298.15 K, J. Chem. Eng. Data. 41 (1996) 166–169. doi:10.1021/je9501806.

[65]   N. V. Grinberg, A.S. Dubovik, V.Y. Grinberg, D. V. Kuznetsov, E.E. Makhaeva, A.Y. Grosberg, T. Tanaka, Studies of the Thermal Volume Transition of Poly(N -isopropylacrylamide) Hydrogels by High-Sensitivity Differential Scanning Microcalorimetry. 1. Dynamic Effects, Macromolecules. 32 (1999) 1471–1475. doi:10.1021/ma9810924.

[66]   S. Takata, K. Suzuki, T. Norisuye, M. Shibayama, Dependence of shrinking kinetics of poly(N-isopropylacrylamide) gels on preparation temperature, Polymer. 43 (2002) 3101–3107. doi:10.1016/S0032-3861(02)00089-7.

[67]   A. Chetty, J. Kovács, Z. Sulyok, Á. Mészáros, J. Fekete, A. Domján, A. Szilágyi, V. Vargha, A versatile characterization of poly(N-isopropylacrylamide-co-N,N'-methylene-bisacrylamide) hydrogels for composition, mechanical strength, and rheology, Express Polym. Lett. 7 (2013) 95–105. doi:10.3144/expresspolymlett.2013.9.

[68]   T.R. Hoare, D.S. Kohane, Hydrogels in drug delivery: Progress and challenges, Polymer. 49 (2008) 1993–2007. doi:10.1016/j.polymer.2008.01.027.

[69]   S.B. Campbell, T. Hoare, Externally addressable hydrogel nanocomposites for biomedical applications, Curr. Opin. Chem. Eng. 4 (2014) 1–10. doi:10.1016/j.coche.2013.12.003.

[70]   U. Szeluga, B. Kumanek, B. Trzebicka, Composites : Part A Synergy in hybrid polymer / nanocarbon composites . A review, Compos. Part a. 73 (2015) 204–231. doi:10.1016/j.compositesa.2015.02.021.

[71]   P. Schexnailder, G. Schmidt, Nanocomposite polymer hydrogels, Colloid Polym. Sci. 287 (2009) 1–11. doi:10.1007/s00396-008-1949-0.

[72]   S.A. Meenach, A.A. Anderson, M. Suthar, K.W. Anderson, J.Z. Hilt, Biocompatibility analysis of magnetic hydrogel nanocomposites based on poly(N-isopropylacrylamide) and iron oxide., J. Biomed. Mater. Res. A. 91 (2009) 903–909. doi:10.1002/jbm.a.32322.

[73]   K. Hu, D.D. Kulkarni, I. Choi, V. V. Tsukruk, Graphene-polymer nanocomposites for structural and functional applications, Prog. Polym. Sci. 39 (2014) 1934–1972. doi:10.1016/j.progpolymsci.2014.03.001.

[74]   P.M. Ajayan, L.S. Schadler, P.V. Braun, Nanocomposite science and technology, Weinheim: John Wiley & Sons, 2006. doi:10.1002/3527602127.

[75]   H. Kim, A. Abdala, C.W. Macosko, Graphene/polymer nanocomposites, Macromolecules. 43 (2010) 6515–6530. doi:10.1021/ma100572e.

[76]   T. Kuilla, S. Bhadra, D. Yao, N.H. Kim, S. Bose, J.H. Lee, Recent advances in graphene based polymer composites, Prog. Polym. Sci. 35 (2010) 1350–1375. doi:10.1016/j.progpolymsci.2010.07.005.

[77]   G. Mittal, V. Dhand, K.Y. Rhee, S.-J. Park, W.R. Lee, A review on carbon nanotubes and graphene as fillers in reinforced polymer nanocomposites, J. Ind. Eng. Chem. 21 (2014) 11–25.

doi:10.1016/j.jiec.2014.03.022.

[78] N. Grossiord, J. Loos, O. Regev, C.E. Koning, Toolbox for Dispersing Carbon Nanotubes into Polymer To Get Conductive Nanocomposites, Chem. Mater. 18 (2006) 1089–1099. doi:10.1021/cm051881h.

[79] H. Takeno, C. Sato, Effects of molecular mass of polymer and composition on the compressive properties of hydrogels composed of Laponite and sodium polyacrylate, Appl. Clay Sci. 123 (2016) 141–147. doi:10.1016/j.clay.2016.01.030.

[80] B.S. Villacorta, T.H. Hubing, A. a. Ogale, Influence of composite electrical properties on the VHF-UHF electromagnetic shielding characteristics of polyethylene-carbon nanoparticle composites, Compos. Sci. Technol. 89 (2013) 158–166. doi:10.1016/j.compscitech.2013.10.003.

[81] B. Safadi, R. Andrews, E.A. Grulke, Multiwalled carbon nanotube polymer composites: Synthesis and characterization of thin films, J. Appl. Polym. Sci. 84 (2002) 2660–2669. doi:10.1002/app.10436.

[82] J. Jang, J. Bae, S.-H. Yoon, A study on the effect of surface treatment of carbon nanotubes for liquid crystalline epoxide–carbon nanotube composites, J. Mater. Chem. 13 (2003) 676–681. doi:10.1039/b212190e.

[83] X. Gong, J. Liu, S. Baskaran, R.D. Voise, J.S. Young, Surfactant-assisted processing of carbon nanotube/polymer composites, Chem. Mater. 12 (2000) 1049–1052. doi:10.1021/cm9906396.

[84] S. Cui, R. Canet, A. Derre, M. Couzi, P. Delhaes, C haracterization of multiwall carbon nanotubes and in uence of surfactant in the nanocomposite processing, Carbon. 41 (2003) 797–809. doi:10.1016/S0008-6223(02)00405-0.

[85] F. Du, J.E. Fischer, K.I. Winey, Coagulation Method for Preparing Single-Walled Carbon Nanotube / Poly (methyl methacrylate) Composites and Their Modulus , Electrical Conductivity , and Thermal Stability, J. Polym. Sci. Part B Polym. Phys. 41 (2003) 3333–3338.

[86] Y. Dror, W. Salalha, R.L. Khalfin, Y. Cohen, A.L. Yarin, E. Zussman, Carbon Nanotubes Embedded in Oriented Polymer Nanofibers by Electrospinning, Langmuir. 19 (2003) 7012–7020. doi:10.1021/la034234i.

[87] R. Sen, B. Zhao, D. Perea, M.E. Itkis, H. Hu, J. Love, E. Bekyarova, R.C. Haddon, Preparation of Single-Walled Carbon Nanotube Reinforced Polystyrene and Polyurethane Nanofibers and Membranes by Electrospinning, Nano Lett. 4 (2004) 459–464. doi:10.1021/nl035135s.

[88] D.E. Hill, Y. Lin, a M. Rao, L.F. Allard, Y.P. Sun, Functionalization of carbon nanotubes with polystyrene, Macromolecules. 35 (2002) 9466–9471. doi:Doi 10.1021/Ma020855r.

[89] P. Pötschke, A.R. Bhattacharyya, A. Janke, Melt mixing of polycarbonate with multiwalled carbon nanotubes: Microscopic studies on the state of dispersion, Eur. Polym. J. 40 (2004) 137–148. doi:10.1016/j.eurpolymj.2003.08.008.

[90] R. Haggenmueller, W. Zhou, J.E. Fischer, K.I. Winey, Production and Characterization of Polymer Nanocomposites with Highly Aligned Single-Walled Carbon Nanotubes, J. Nanosci. Nanotechnol. 3 (2003) 105–110. doi:10.1166/jnn.2003.173.

[91] J.Y. Kim, S.H. Kim, Influence of Multiwall Carbon nanotube on Physical Properties of Poly(ethylene 2,6-naphhlae) Nanocomposies, J. Polym. Sci. Part B Polym. Phys. 44 (2006) 1062–1071. doi:10.1002/polb.20728.

[92] C.A. Cooper, D. Ravich, D. Lips, J. Mayer, H.D. Wagner, Distribution and alignment of carbon nanotubes and nano brils in a polymer matrix, Compos. Sci. Technol. 62 (2008) 1105–1112. doi:10.1016/S0266-3538(02)00056-8.

[93] M. Moniruzzaman, K.I. Winey, Polymer nanocomposites containing carbon nanotubes, Macromolecules. 39 (2006) 5194–5205. doi:10.1021/ma060733p.

[94] D. Qian, E.C. Dickey, R. Andrews, T. Rantell, Load transfer and deformation mechanisms in carbon nanotube-polystyrene composites, Appl. Phys. Lett. 76 (2000) 2868–2870.

doi:10.1063/1.126500.

[95] K. Haraguchi, Y. Xu, G. Li, Poly(N-isopropylacrylamide) prepared by free-radical polymerization in aqueous solutions and in nanocomposite hydrogels, Macromol. Symp. 306–307 (2011) 33–48. doi:10.1002/masy.201000149.

[96] K. Haraguchi, Y. Xu, G. Li, Molecular characteristics of poly(N-isopropylacrylamide) separated from nanocomposite gels by removal of clay from the polymer/clay network, Macromol. Rapid Commun. 31 (2010) 718–723. doi:10.1002/marc.200900819.

[97] T. Nishida, A. Obayashi, K. Haraguchi, M. Shibayama, Stress relaxation and hysteresis of nanocomposite gel investigated by SAXS and SANS measurement, Polym. (United Kingdom). 53 (2012) 4533–4538. doi:10.1016/j.polymer.2012.07.038.

[98] M. Shibayama, T. Karino, S. Miyazaki, Small-angle neutron scattering study on uniaxially stretched poly (N-isopropylacrylamide)-clay nanocomposite gels, Macromolecules. (2005) 10772–10781. doi:10.1021/ma051979h.

[99] H. Takeno, Y. Kimura, Molecularweight effects on tensile properties of blend hydrogels composed of clay and polymers, Polym. (United Kingdom). 85 (2016) 47–54. doi:10.1016/j.polymer.2016.01.008.

[100] E. Manek, B. Berke, N. Miklósi, M. Sajbán, A. Domán, T. Fukuda, O. Czakkel, K. László, Thermal sensitivity of carbon nanotube and graphene oxide containing responsive hydrogels, Express Polym. Lett. 10 (2016) 710–720. doi:10.3144/expresspolymlett.2016.64.

[101] K. Shi, Z. Liu, Y.-Y. Wei, W. Wang, X.-J. Ju, R. Xie, L.-Y. Chu, Near-infrared light-responsive poly(N-isopropylacrylamide)/graphene oxide nanocomposite hydrogels with ultrahigh tensibility, ACS Appl. Mater. Interfaces. 7 (2015) 27289–27298. doi:10.1021/acsami.5b08609.

[102] Z. Li, J. Shen, H. Ma, X. Lu, M. Shi, N. Li, M. Ye, Preparation and characterization of pH- and temperature-responsive hydrogels with surface-functionalized graphene oxide as the crosslinker, Soft Matter. 8 (2012) 3139–3145. doi:10.1039/c2sm07012j.

[103] C.-W. Lo, D. Zhu, H. Jiang, An infrared-light responsive graphene-oxide incorporated poly(N-isopropylacrylamide) hydrogel nanocomposite, Soft Matter. 7 (2011) 5604–5609. doi:10.1039/c1sm00011j.

[104] X. Ma, Y. Li, W. Wang, Q. Ji, Y. Xia, Temperature-sensitive poly(N-isopropylacrylamide)/graphene oxide nanocomposite hydrogels by in situ polymerization with improved swelling capability and mechanical behavior, Eur. Polym. J. 49 (2013) 389–396. doi:10.1016/j.eurpolymj.2012.10.034.

[105] V. Alzari, D. Nuvoli, S. Scognamillo, Graphene-containing thermoresponsive nanocomposite hydrogels of poly (N-isopropylacrylamide) prepared by frontal polymerization, J. Mater. Chem. (2011) 8727–8733. doi:10.1039/c1jm11076d.

[106] E. Loizou, P. Butler, L. Porcar, G. Schmidt, Dynamic Responses in Nanocomposite Hydrogels, Macromolecules. 39 (2006) 1614–1619. doi:10.1021/ma0517547.

[107] P. Das, S. Schipmann, J.M. Malho, B. Zhu, U. Klemradt, A. Walther, Facile access to large-scale, self-assembled, nacre-inspired, high-performance materials with tunable nanoscale periodicities, ACS Appl. Mater. Interfaces. 5 (2013) 3738–3747. doi:10.1021/am400350q.

[108] X. Sun, H. Sun, H. Li, H. Peng, Developing polymer composite materials: Carbon nanotubes or graphene?, Adv. Mater. 25 (2013) 5153–5176. doi:10.1002/adma.201301926.

[109] P. Podsiadlo, A.K. Kaushik, E.M. Arruda, A.M. Waas, B.S. Shim, J. Xu, H. Nandivada, B.G. Pumplin, J. Lahann, A. Ramamoorthy, N. a Kotov, Ultrastrong and stiff layered polymer nanocomposites., Science. 318 (2007) 80–83. doi:10.1126/science.1143176.

[110] Z. Shi, X. Chen, X. Wang, T. Zhang, J. Jin, Fabrication of superstrong ultrathin free-standing single-walled carbon nanotube films via a wet process, Adv. Funct. Mater. 21 (2011) 4358–4363. doi:10.1002/adfm.201101298.

[111] A.A. Mamedov, N.A. Kotov, M. Prato, D.M. Guldi, J.P. Wicksted, A. Hirsch, Molecular design of strong single-wall carbon nanotube/polyelectrolyte multilayer composites., Nat. Mater. 1 (2002) 190–194. doi:10.1038/nmat747.

[112] B.S. Shim, J. Zhu, E. Jan, K. Critchley, S. Ho, P. Podsiadlo, K. Sun, N.A. Kotov, Multiparameter structural optimization of single-walled carbon nanotube composites: Toward record strength, stiffness, and toughness, ACS Nano. 3 (2009) 1711–1722. doi:10.1021/nn9002743.

[113] A. Eitan, F.T. Fisher, R. Andrews, L.C. Brinson, L.S. Schadler, Reinforcement mechanisms in MWCNT-filled polycarbonate, Compos. Sci. Technol. 66 (2006) 1159–1170. doi:10.1016/j.compscitech.2005.10.004.

[114] R. Gunawidjaja, C. Jiang, S. Peleshanko, M. Ornatska, S. Singamaneni, V. V. Tsukruk, Flexible and robust 2D arrays of silver nanowires encapsulated within freestanding layer-by-layer films, Adv. Funct. Mater. 16 (2006) 2024–2034. doi:10.1002/adfm.200600430.

[115] C. Jiang, S. Markutsya, V. V. Tsukruk, Compliant, robust, and truly nanoscale free-standing multilayer films fabricated using spin-assisted layer-by-layer assembly, Adv. Mater. 16 (2004) 157–161. doi:10.1002/adma.200306010.

[116] K. Haraguchi, T. Takehisa, S. Fan, Effects of Clay Content on the Properties of Nanocomposite Hydrogels Composed of Poly(N -isopropylacrylamide) and Clay, Macromolecules. 35 (2002) 10162–10171. doi:10.1021/ma021301r.

[117] K. Haraguchi, K. Uyama, H. Tanimoto, Self-healing in nanocomposite hydrogels, Macromol. Rapid Commun. 32 (2011) 1253–1258. doi:10.1002/marc.201100248.

[118] X. Xia, J. Yih, N. a. D'Souza, Z. Hu, Swelling and mechanical behavior of poly (N-isopropylacrylamide)/Na-montmorillonite layered silicates composite gels, Polymer. 44 (2003) 3389–3393. doi:10.1016/S0032-3861(03)00228-3.

[119] B. Strachotová, a. Strachota, M. Uchman, M. Šlouf, J. Brus, J. Pleštil, L. Matějka, Super porous organic-inorganic poly(N-isopropylacrylamide)-based hydrogel with a very fast temperature response, Polymer. 48 (2007) 1471–1482. doi:10.1016/j.polymer.2007.01.042.

[120] G.P. Baeza, A.-C. Genix, N. Paupy-Peyronnet, C. Degrandcourt, M. Couty, J. Oberdisse, Revealing nanocomposite filler structures by swelling and small-angle X-ray scattering, Faraday Discuss. 186 (2016) 295–309. doi:10.1039/C5FD00117J.

[121] J. Rubio-Retama, N.E. Zafeiropoulos, C. Serafinelli, R. Rojas-Reyna, B. Voit, E.L. Cabarcos, M. Stamm, Synthesis and Characterization of Thermosensitive PNIPAM Microgels Covered with Superparamagnetic γ -Fe2O3 Nanoparticles, Langmuir. (2007) 10280–10285. doi:10.1021/la7009594.

[122] L. Janovák, Intelligens hidrogél / rétegszilikát és hidrogél / arany nanohibrid rendszerek szintézise és tulajdonságai (PhD Thesis), Szegedi Tudományegyetem, 2009.

[123] T. Endo, R. Ikeda, Y. Yanagida, T. Hatsuzawa, Stimuli-responsive hydrogel-silver nanoparticles composite for development of localized surface plasmon resonance-based optical biosensor, Anal. Chim. Acta. 611 (2008) 205–211. doi:10.1016/j.aca.2008.01.078.

[124] Z. Spitalsky, D. Tasis, K. Papagelis, C. Galiotis, Carbon nanotube-polymer composites: Chemistry, processing, mechanical and electrical properties, Prog. Polym. Sci. 35 (2010) 357–401. doi:10.1016/j.progpolymsci.2009.09.003.

[125] Z.-M. Dang, J.-K. Yuan, J.-W. Zha, T. Zhou, S.-T. Li, G.H. Hu, Fundamentals, processes and applications of high-permittivity polymer-matrix composites, Prog. Mater. Sci. 57 (2012) 660–723. doi:10.1016/j.pmatsci.2011.08.001.

[126] R. Sengupta, M. Bhattacharya, S. Bandyopadhyay, A.K. Bhowmick, A review on the mechanical and electrical properties of graphite and modified graphite reinforced polymer composites, Prog. Polym. Sci. 36 (2011) 638–670. doi:10.1016/j.progpolymsci.2010.11.003.

[127] M. Biron, Thermosets and Composites, in: Mater. Sel. Appl. Manuf. Cost Anal., 2013: pp.

299–473. doi:10.1016/B978-1-4557-3124-4.00006-7.

[128] C. Sirisinha, N. Prayoonchatphan, Study of carbon black distribution in BR/NBR blends based on damping properties: Influences of carbon black particle size, filler, and rubber polarity, J. Appl. Polym. Sci. 81 (2001) 3198–3203. doi:10.1002/app.1773.

[129] S.Y. Yang, W.N. Lin, Y.L. Huang, H.W. Tien, J.Y. Wang, C.C.M. Ma, S.M. Li, Y.S. Wang, Synergetic effects of graphene platelets and carbon nanotubes on the mechanical and thermal properties of epoxy composites, Carbon. 49 (2011) 793–803. doi:10.1016/j.carbon.2010.10.014.

[130] G. Cirillo, S. Hampel, U.G. Spizzirri, O.I. Parisi, N. Picci, F. Iemma, Carbon nanotubes hybrid hydrogels in drug delivery: A perspective review, Biomed Res. Int. 2014 (2014) Article ID 825017, 17 pages. doi:10.1155/2014/825017.

[131] C.H. Zhu, Y. Lu, J. Peng, J.F. Chen, S.H. Yu, Photothermally sensitive poly(N-isopropylacrylamide)/graphene oxide nanocomposite hydrogels as remote light-controlled liquid microvalves, Adv. Funct. Mater. 22 (2012) 4017–4022. doi:10.1002/adfm.201201020.

[132] E. Miyako, H. Nagata, K. Hirano, T. Hirotsu, Photodynamic thermoresponsive nanocarbon-polymer gel hybrids, Small. 4 (2008) 1711–1715. doi:10.1002/smll.200800601.

[133] X. Zhang, C.L. Pint, M.H. Lee, B.E. Schubert, A. Jamshidi, K. Takei, H. Ko, A. Gillies, R. Bardhan, J.J. Urban, M. Wu, R. Fearing, A. Javey, Optically- and thermally-responsive programmable materials based on carbon nanotube-hydrogel polymer composites, Nano Lett. 11 (2011) 3239–3244. doi:10.1021/nl201503e.

[134] J.N. Coleman, U. Khan, W.J. Blau, Y.K. Gun'ko, Small but strong: A review of the mechanical properties of carbon nanotube-polymer composites, Carbon. 44 (2006) 1624–1652. doi:10.1016/j.carbon.2006.02.038.

[135] W. Bauhofer, J.Z. Kovacs, A review and analysis of electrical percolation in carbon nanotube polymer composites, Compos. Sci. Technol. 69 (2009) 1486–1498. doi:10.1016/j.compscitech.2008.06.018.

[136] G. Pandey, E.T. Thostenson, Carbon Nanotube-Based Multifunctional Polymer Nanocomposites, Polym. Rev. 52 (2012) 355–416. doi:10.1080/15583724.2012.703747.

[137] D. Li, M.B. Müller, S. Gilje, R.B. Kaner, G.G. Wallace, Processable aqueous dispersions of graphene nanosheets., Nat. Nanotechnol. 3 (2008) 101–105. doi:10.1038/nnano.2007.451.

[138] T. Zhou, J.W. Zha, Y. Hou, D. Wang, J. Zhao, Z.M. Dang, Surface-functionalized MWNTs with emeraldine base: Preparation and improving dielectric properties of polymer nanocomposites, ACS Appl. Mater. Interfaces. 3 (2011) 4557–4560. doi:10.1021/am201454e.

[139] W. Li, A. Dichiara, J. Bai, Carbon nanotube-graphene nanoplatelet hybrids as high-performance multifunctional reinforcements in epoxy composites, Compos. Sci. Technol. 74 (2013) 221–227. doi:10.1016/j.compscitech.2012.11.015.

[140] M. Xia, W. Wu, F. Liu, P. Theato, M. Zhu, Swelling behavior of thermosensitive nanocomposite hydrogels composed of oligo(ethylene glycol) methacrylates and clay, Eur. Polym. J. 69 (2015) 472–482. doi:10.1016/j.eurpolymj.2015.03.072.

[141] M. Ashraful Alam, M. Takafuji, H. Ihara, Thermosensitive hybrid hydrogels with silica nanoparticle-cross-linked polymer networks, J. Colloid Interface Sci. 405 (2013) 109–117. doi:10.1016/j.jcis.2013.04.054.

[142] V. Can, S. Abdurrahmanoglu, O. Okay, Unusual swelling behavior of polymer-clay nanocomposite hydrogels, Polymer. 48 (2007) 5016–5023. doi:10.1016/j.polymer.2007.06.066.

[143] L.V. Radushkevich, V.M. Lukyanovich, About the structure of carbon formed by thermal decomposition of carbon monoxide on iron substrate, Zurn. Fis. Chim. 26 (1952) 88–95.

[144] S. Iijima, Helical microtubules of graphitic carbon, Nature. 354 (1991) 56–58. doi:10.1038/354056a0.

[145] S. Iijima, T. Ichihashi, Single-shell carbon nanotubes of 1-nm diameter, Nature. 363 (1993)

603–605. doi:10.1038/363603a0.

[146] http://images.iop.org/objects/ntw/journal/11/5/13/image1.jpg, (n.d.).

[147] M. Buongiorno Nardelli, C.J. Brabec, A. Maiti, C.M. Roland, J. Bernholc, Lip-Lip Interactions and the Growth of Multiwalled Carbon Nanotubes, Phys. Rev. Lett. 80 (1998) 313–316. doi:10.1103/PhysRevLett.80.313.

[148] Z. Wang, M.D. Shirley, S.T. Meikle, R.L.D. Whitby, S. V. Mikhalovsky, The surface acidity of acid oxidised multi-walled carbon nanotubes and the influence of in-situ generated fulvic acids on their stability in aqueous dispersions, Carbon. 47 (2009) 73–79. doi:10.1016/j.carbon.2008.09.038.

[149] M. Monthioux, V.L. Kuznetsov, Who should be given the credit for the discovery of carbon nanotubes?, Carbon. 44 (2006) 1621–1623. doi:10.1016/j.carbon.2006.03.019.

[150] E.T. Thostenson, Z. Ren, T.-W. Chou, Advances in the science and technology of carbon nanotubes and their composites: a review, Compos. Sci. Technol. 61 (2001) 1899–1912. doi:10.1016/S0266-3538(01)00094-X.

[151] M.M.J. Treacy, T.W. Ebbesen, J.M. Gibson, Exceptionally high Young's modulus observed for individual carbon nanotubes, Nature. 381 (1996) 678–680. doi:10.1038/381678a0.

[152] M.-F. Yu, B.S. Files, S. Arepalli, R.S. Ruoff, Tensile Loading of Ropes of Single Wall Carbon Nanotubes and their Mechanical Properties, Phys. Rev. Lett. 84 (2000) 5552–5555. doi:10.1103/PhysRevLett.84.5552.

[153] O.A. Ageev, O.I. Il'in, A.S. Kolomiitsev, B.G. Konoplev, M. V. Rubashkina, V.A. Smirnov, A.A. Fedotov, Development of a technique for determining Young's modulus of vertically aligned carbon nanotubes using the nanoindentation method, Nanotechnologies Russ. 7 (2012) 47–53. doi:10.1134/S1995078012010028.

[154] N. Hamada, S.I. Sawada, A. Oshiyama, New one-dimensional conductors: Graphitic microtubules, Phys. Rev. Lett. 68 (1992) 1579–1581. doi:10.1103/PhysRevLett.68.1579.

[155] S. Berber, Y.-K. Kwon, D. Tomanek, Unusually high thermal conductivity of carbon nanotubes, Phys. Rev. Lett. 84 (2000) 4613–4616. doi:10.1103/PhysRevLett.84.4613.

[156] J. Hone, M. Whitney, C. Piskoti, A. Zettl, Thermal conductivity of single-walled carbon nanotubes, Phys. Rev. B. 59 (1999) R2514–R2516. doi:10.1103/PhysRevB.59.R2514.

[157] A. Szabó, C. Perri, A. Csató, G. Giordano, D. Vuono, J.B. Nagy, Synthesis methods of carbon nanotubes and related materials, Materials. 3 (2010) 3092–3140. doi:10.3390/ma3053092.

[158] C.E. Baddour, C. Briens, Carbon Nanotube Synthesis : A Review, Int. J. Chem. React. Eng. 3 (2005). doi:10.2202/1542-6580.1279.

[159] J.-F. Colomer, C. Stephan, S. Lefrant, G. Van Tendeloo, I. Willems, Z. Kónya, A. Fonseca, C. Laurent, J.. Nagy, Large-scale synthesis of single-wall carbon nanotubes by catalytic chemical vapor deposition (CCVD) method, Chem. Phys. Lett. 317 (2000) 83–89. doi:10.1016/S0009-2614(99)01338-X.

[160] R. Das, Z. Shahnavaz, M.E. Ali, M.M. Islam, S.B. Abd Hamid, Can We Optimize Arc Discharge and Laser Ablation for Well-Controlled Carbon Nanotube Synthesis?, Nanoscale Res. Lett. 11 (2016) 510. doi:10.1186/s11671-016-1730-0.

[161] A. Bougrine, A. Naji, J. Ghanbaja, D. Billaud, Purification and structural characterization of single-walled carbon nanotubes, Synth. Met. 103 (1999) 2480–2481. doi:10.1016/S0379-6779(98)01064-9.

[162] F. Li, H.M. Cheng, Y.T. Xing, P.H. Tan, G. Su, Purification of single-walled carbon nanotubes synthesized by the catalytic decomposition of hydrocarbons, Carbon. 38 (2000) 2041–2045. doi:10.1016/S0008-6223(00)00061-0.

[163] Y. Feng, G. Zhou, G. Wang, M. Qu, Z. Yu, Removal of some impurities from carbon nanotubes, Chem. Phys. Lett. 375 (2003) 645–648. doi:10.1016/S0009-2614(03)00947-3.

[164] L. Vaccarini, C. Goze, R. Aznar, V. Micholet, C. Journet, P. Bernier, Purification procedure of

carbon nanotubes, Synth. Met. 103 (1999) 2492–2493. doi:10.1016/S0379-6779(98)01087-X.

[165] J.-F. Colomer, P. Piedigrosso, I. Willems, C. Journet, P. Bernier, G. Van Tendeloo, a Fonseca, J. B.Nagy, Purification of catalytically produced multi-wall nanotubes, J. Chem. Soc. Faraday Trans. 94 (1998) 3753–3758. doi:10.1039/a806804f.

[166] R. Verdejo, S. Lamoriniere, B. Cottam, A. Bismarck, M. Shaffer, Removal of oxidation debris from multi-walled carbon nanotubes, Chem. Commun. (2007) 513–515. doi:10.1039/B611930A.

[167] P.M. Ajayan, O. Stephan, C. Colliex, D. Trauth, Aligned carbon nanotube arrays formed by cutting a polymer resin--nanotube composite., Science. 265 (1994) 1212–1214. doi:10.1126/science.265.5176.1212.

[168] M.F. Islam, a M. Alsayed, Z. Dogic, J. Zhang, T.C. Lubensky, a G. Yodh, Nematic nanotube gels., Phys. Rev. Lett. 92 (2004) 88303. doi:10.1103/PhysRevLett.92.088303.

[169] M.C. Weisenberger, E.A. Grulke, D. Jacques, T. Rantell, R. Andrews, Enhanced mechanical properties of polyacrylonitrile/multiwall carbon nanotube composite fibers., J. Nanosci. Nanotechnol. 3 (2003) 535–539. doi:10.1166/jnn.2003.239.

[170] J. Bai, Evidence of the reinforcement role of chemical vapour deposition multi-walled carbon nanotubes in a polymer matrix, Carbon. 41 (2003) 1325–1328. doi:10.1016/S0008-6223(03)00034-4.

[171] R. Andrews, M.C. Weisenberger, Carbon nanotube polymer composites, Curr. Opin. Solid State Mater. Sci. 8 (2004) 31–37. doi:10.1016/j.cossms.2003.10.006.

[172] A.B. Dalton, S. Collins, E. Munoz, J.M. Razal, V.H. Ebron, J.P. Ferraris, J.N. Coleman, B.G. Kim, R.H. Baughman, Super-tough carbon-nanotube fibres, Nature. 423 (2006) 703. doi:10.1038/423703a.

[173] M. Cadek, J.N. Coleman, V. Barron, K. Hedicke, W.J. Blau, Morphological and mechanical properties of carbon-nanotube-reinforced semicrystalline and amorphous polymer composites, Appl. Phys. Lett. 81 (2002) 5123–5125. doi:10.1063/1.1533118.

[174] M.J. Biercuk, M.C. Llaguno, M. Radosavljevic, J.K. Hyun, A.T. Johnson, J.E. Fischer, Carbon nanotube composites for thermal management, Appl. Phys. Lett. 80 (2002) 2767–2769. doi:10.1063/1.1469696.

[175] C. Velasco-Santos, A.L. Martínez-Hernández, F.T. Fisher, R.S. Ruoff, V.M. Castaño, Improvement of Thermal and Mechanical Properties of Carbon Nanotube Composites through Chemical Functionalization, Chem. Mater. 15 (2003) 4470–4475. doi:10.1021/cm034243c.

[176] P.C. Ma, J.K. Kim, B.Z. Tang, Effects of silane functionalization on the properties of carbon nanotube/epoxy nanocomposites, Compos. Sci. Technol. 67 (2007) 2965–2972. doi:10.1016/j.compscitech.2007.05.006.

[177] L. Chen, X.J. Pang, Z.L. Yu, Study on polycarbonate/multi-walled carbon nanotubes composite produced by melt processing, Mater. Sci. Eng. A. 457 (2007) 287–291. doi:10.1016/j.msea.2007.01.107.

[178] Y.S. Chen, P.C. Tsou, J.M. Lo, H.C. Tsai, Y.Z. Wang, G.H. Hsiue, Poly(N-isopropylacrylamide) hydrogels with interpenetrating multiwalled carbon nanotubes for cell sheet engineering, Biomaterials. 34 (2013) 7328–7334. doi:10.1016/j.biomaterials.2013.06.017.

[179] Z. Yang, Z. Cao, H. Sun, Y. Li, Composite films based on aligned carbon nanotube arrays and a poly(N-isopropyl acrylamide) hydrogel, Adv. Mater. 20 (2008) 2201–2205. doi:10.1002/adma.200701964.

[180] T. Fujigaya, T. Morimoto, Y. Niidome, N. Nakashima, NIR laser-driven reversible volume phase transition of single-walled carbon nanotube/ poly(N-isopropylacrylamide) composite gels, Adv. Mater. 20 (2008) 3610–3614. doi:10.1002/adma.200800494.

[181] B. Jiang, C. Liu, C. Zhang, B. Wang, Z. Wang, The effect of non-symmetric distribution of

fiber orientation and aspect ratio on elastic properties of composites, Compos. Part B Eng. 38 (2007) 24–34. doi:10.1016/j.compositesb.2006.05.002.

[182] H.G. Chae, M.L. Minus, S. Kumar, Oriented and exfoliated single wall carbon nanotubes in polyacrylonitrile, Polymer. 47 (2006) 3494–3504. doi:10.1016/j.polymer.2006.03.050.

[183] T. V. Kosmidou, A.S. Vatalis, C.G. Delides, E. Logakis, P. Pissis, G.C. Papanicolaou, Structural, mechanical and electrical characterization of epoxy-amine/carbon black nanonocomposites, Express Polym. Lett. 2 (2008) 364–372. doi:10.3144/expresspolymlett.2008.43.

[184] T. Fukushima, A. Kosaka, Y. Yamamoto, T. Aimiya, S. Notazawa, T. Takigawa, T. Inabe, T. Aida, Dramatic effect of dispersed carbon nanotubes on the mechanical and electroconductive properties of polymers derived from ionic liquids, Small. 2 (2006) 554–560. doi:10.1002/smll.200500404.

[185] P.C. Ma, N. a. Siddiqui, G. Marom, J.K. Kim, Dispersion and functionalization of carbon nanotubes for polymer-based nanocomposites: A review, Compos. Part A Appl. Sci. Manuf. 41 (2010) 1345–1367. doi:10.1016/j.compositesa.2010.07.003.

[186] A. Allaoui, S. Bai, H.M. Cheng, J.B. Bai, Mechanical and electrical properties of a MWNT / epoxy composite, Compos. Sci. Technol. 62 (2002) 1993–1998. doi:10.1016/S0266-3538(02)00129-X.

[187] J.O. Aguilar, J.R. Bautista-Quijano, F. Avilés, Influence of carbon nanotube clustering on the electrical conductivity of polymer composite films, Express Polym. Lett. 4 (2010) 292–299. doi:10.3144/expresspolymlett.2010.37.

[188] Q. Zhang, S. Rastogi, D. Chen, D. Lippits, P.J. Lemstra, Low percolation threshold in single-walled carbon nanotube/high density polyethylene composites prepared by melt processing technique, Carbon. 44 (2006) 778–785. doi:10.1016/j.carbon.2005.09.039.

[189] M. Martin-Gallego, M.M. Bernal, M. Hernandez, R. Verdejo, M.A. Lopez-Manchado, Comparison of filler percolation and mechanical properties in graphene and carbon nanotubes filled epoxy nanocomposites, Eur. Polym. J. 49 (2013) 1347–1353. doi:10.1016/j.eurpolymj.2013.02.033.

[190] S. Stankovich, D. a Dikin, G.H.B. Dommett, K.M. Kohlhaas, E.J. Zimney, E. a Stach, R.D. Piner, S.T. Nguyen, R.S. Ruoff, Graphene-based composite materials., Nature. 442 (2006) 282–286. doi:10.1038/nature04969.

[191] J. Li, J.K. Kim, Percolation threshold of conducting polymer composites containing 3D randomly distributed graphite nanoplatelets, Compos. Sci. Technol. 67 (2007) 2114–2120. doi:10.1016/j.compscitech.2006.11.010.

[192] T. Wei, G. Luo, Z. Fan, C. Zheng, J. Yan, C. Yao, W. Li, C. Zhang, Preparation of graphene nanosheet/polymer composites using in situ reduction-extractive dispersion, Carbon. 47 (2009) 2296–2299. doi:10.1016/j.carbon.2009.04.030.

[193] D. Galpaya, Recent Advances in Fabrication and Characterization of Graphene-Polymer Nanocomposites, Graphene. 1 (2012) 30–49. doi:10.4236/graphene.2012.12005.

[194] N. Yousefi, X. Lin, Q. Zheng, X. Shen, J.R. Pothnis, J. Jia, E. Zussman, J.K. Kim, Simultaneous in situ reduction, self-alignment and covalent bonding in graphene oxide/epoxy composites, Carbon. 59 (2013) 406–417. doi:10.1016/j.carbon.2013.03.034.

[195] L. Yue, G. Pircheraghi, S.A. Monemian, I. Manas-Zloczower, Epoxy composites with carbon nanotubes and graphene nanoplatelets - Dispersion and synergy effects, Carbon. 78 (2014) 268–278. doi:10.1016/j.carbon.2014.07.003.

[196] P. Pokharel, Q.T. Truong, D.S. Lee, Multi-step microwave reduction of graphite oxide and its use in the formation of electrically conductive graphene/epoxy composites, Compos. Part B Eng. 64 (2014) 187–193. doi:10.1016/j.compositesb.2014.04.013.

[197] J. Syurik, N. Alyabyeva, A. Alekseev, O. a. Ageev, AFM-based model of percolation in

graphene-based polymer nanocomposites, Compos. Sci. Technol. 95 (2014) 38–43. doi:10.1016/j.compscitech.2014.02.006.

[198] P. Zhao, Y. Luo, J. Yang, D. He, L. Kong, P. Zheng, Q. Yang, Electrically conductive graphene-filled polymer composites with well organized three-dimensional microstructure, Mater. Lett. 121 (2014) 74–77. doi:10.1016/j.matlet.2014.01.100.

[199] S. Wu, R.B. Ladani, J. Zhang, E. Bafekrpour, K. Ghorbani, A.P. Mouritz, A.J. Kinloch, C.H. Wang, Aligning multilayer graphene flakes with an external electric field to improve multifunctional properties of epoxy nanocomposites, Carbon. 94 (2015) 607–618. doi:10.1016/j.carbon.2015.07.026.

[200] A.K. Geim, K.S. Novoselov, The rise of graphene., Nat. Mater. 6 (2007) 183–191. doi:10.1038/nmat1849.

[201] S. V. Morozov, K.S. Novoselov, M.I. Katsnelson, F. Schedin, D.C. Elias, J.A. Jaszczak, A.K. Geim, Giant intrinsic carrier mobilities in graphene and its bilayer, Phys. Rev. Lett. 100 (2008) 11–14. doi:10.1103/PhysRevLett.100.016602.

[202] C. Lee, X. Wei, J.W. Kysar, J. Hone, Measurement of the elastic properties and intrinsic strength of monolayer graphene., Science. 321 (2008) 385–388. doi:10.1126/science.1157996.

[203] A.A. Balandin, S. Ghosh, W. Bao, I. Calizo, D. Teweldebrhan, F. Miao, C.N. Lau, Superior Thermal Conductivity of Single-Layer Graphene 2008, Nano Lett. 8 (2008) 902–907. doi:10.1021/nl0731872.

[204] P. Avouris, F. Xia, Graphene applications in electronics and photonics, MRS Bull. 37 (2012) 1225–1234. doi:10.1557/mrs.2012.206.

[205] Y. Zhu, S. Murali, W. Cai, X. Li, J.W. Suk, J.R. Potts, R.S. Ruoff, Graphene and graphene oxide: Synthesis, properties, and applications, Adv. Mater. 22 (2010) 3906–3924. doi:10.1002/adma.201001068.

[206] K.E. Whitener, P.E. Sheehan, Graphene synthesis, Diam. Relat. Mater. 46 (2014) 25–34. doi:10.1016/j.diamond.2014.04.006.

[207] E. Jimenez-Cervantes Amieva, J. Barroso-López, A.L. Martínez-Hernández, C. Velasco-Santos, Graphene - Based Materials Functionalization with Natural Polymeric Biomolecules, in: Recent Adv. Graphene Res., 2016. doi:10.5772/64001.

[208] T. Szabó, O. Berkesi, P. Forgó, K. Josepovits, Y. Sanakis, D. Petridis, I. Dékány, Evolution of surface functional groups in a series of progressively oxidized graphite oxides, Chem. Mater. 18 (2006) 2740–2749. doi:10.1021/cm060258+.

[209] H. He, J. Klinowski, M. Forster, A. Lerf, A new structural model for graphite oxide, Chem. Phys. Lett. 287 (1998) 98–101. doi:10.1016/S0009-2614(98)00144-4.

[210] D.R. Dreyer, S. Park, C.W. Bielawski, R.S. Ruoff, The chemistry of graphene oxide., Chem. Soc. Rev. 39 (2010) 228–240. doi:10.1039/b920539j.

[211] B.C. Brodie, On the Atomic Weight of Graphite, Philos. Trans. R. Soc. London. 149 (1859) 249–259. doi:10.1098/rstl.1859.0013.

[212] L. Staudenmaier, Verfahren zur Darstellung der Graphitsaure, Ber. Dtsch. Chem. Ges. 31 (1898) 1481–1487. doi:10.1002/cber.18980310237.

[213] W.S.J. Hummers, R.E. Offeman, Preparation of Graphitic Oxide, J. Am. Chem. Soc. 80 (1958) 1339. doi:10.1021/ja01539a017.

[214] D.C. Marcano, D. V. Kosynkin, J.M. Berlin, A. Sinitskii, Z. Sun, A. Slesarev, L.B. Alemany, W. Lu, J.M. Tour, Improved synthesis of graphene oxide, ACS Nano. 4 (2010) 4806–4814. doi:10.1021/nn1006368.

[215] N. Justh, B. Berke, K. László, I.M. Szilágyi, Thermal analysis of the improved Hummers' synthesis of graphene oxide, J. Therm. Anal. Calorim. (2017). doi:10.1007/s10973-017-6697-2.

[216] C. Botas, P. Álvarez, C. Blanco, R. Santamaría, M. Granda, P. Ares, F. Rodríguez-Reinoso, R. Menéndez, The effect of the parent graphite on the structure of graphene oxide, Carbon. 50

(2012) 275–282. doi:10.1016/j.carbon.2011.08.045.

[217] S. Kim, Y. Yoo, H. Kim, E. Lee, J.Y. Lee, Reduction of graphene oxide/alginate composite hydrogels for enhanced adsorption of hydrophobic compounds, Nanotechnology. 26 (2015) 1–9. doi:10.1088/0957-4484/26/40/405602.

[218] S. Pei, H.-M. Cheng, The reduction of graphene oxide, Carbon. 50 (2012) 3210–3228. doi:10.1016/j.carbon.2011.11.010.

[219] H.C. Schniepp, J. Li, M.J. Mcallister, H. Sai, M. Herrera-Alonso, D.H. Adamson, R.K. Prud, R. Car, D.A. Saville, I.A. Aksay, Functionalized Single Graphene Sheets Derived from Splitting Graphite Oxide Functionalized Single Graphene Sheets Derived from Splitting Graphite Oxide, 2 (2006) 8535–8539. doi:10.1021/jp060936f.

[220] Y.L. Zhang, L. Guo, H. Xia, Q.D. Chen, J. Feng, H.B. Sun, Photoreduction of Graphene Oxides: Methods, Properties, and Applications, Adv. Opt. Mater. (2013) 1–19. doi:10.1002/adom.201300317.

[221] N.A. Kotov, I. Dékány, J.H. Fendler, Ultrathin graphite oxide - polyelectrolyte composites prepared by self - assembly: non - conductive states, Adv. Mater. 8 (1996) 637–641. doi:10.1002/adma.19960080806.

[222] M.J. Fernández-Merino, L. Guardia, J.I. Paredes, S. Villar-Rodil, P. Solís-Fernández, a. Martínez-Alonso, J.M.D. Tascón, Vitamin C is an ideal substitute for hydrazine in the reduction of graphene oxide suspensions, J. Phys. Chem. C. 114 (2010) 6426–6432. doi:10.1021/jp100603h.

[223] S. Pei, J. Zhao, J. Du, W. Ren, H.M. Cheng, Direct reduction of graphene oxide films into highly conductive and flexible graphene films by hydrohalic acids, Carbon. 48 (2010) 4466–4474. doi:10.1016/j.carbon.2010.08.006.

[224] I.K. Moon, J. Lee, R.S. Ruoff, H. Lee, Reduced graphene oxide by chemical graphitization, Nat. Commun. 1 (2010) 1–6. doi:10.1038/ncomms1067.

[225] Y. Zhou, Q. Bao, L.A.L. Tang, Y. Zhong, K.P. Loh, Hydrothermal dehydration for the "green" reduction of exfoliated graphene oxide to graphene and demonstration of tunable optical limiting properties, Chem. Mater. 21 (2009) 2950–2956. doi:10.1021/cm9006603.

[226] H. Wang, J.T. Robinson, X. Li, H. Dai, Solvothermal reduction of chemically exfoliated graphene sheets, J. Am. Chem. Soc. 131 (2009) 9910–9911. doi:10.1021/ja904251p.

[227] S. Dubin, S. Gilje, K. Wang, V.C. Tung, K. Cha, A.S. Hall, J. Farrar, R. Varshneya, Y. Yang, R.B. Kaner, A one-step, solvothermal reduction method for producing reduced graphene oxide dispersions in organic solvents, ACS Nano. 4 (2010) 3845–3852. doi:10.1021/nn100511a.

[228] G. Demazeau, Solvothermal processes: a route to the stabilization of new materials, J. Mater. Chem. 9 (1999) 15–18. doi:10.1039/a805536j.

[229] D. Kim, S. Lee, J. Yoon, Remote control of volume phase transition of hydrogels containing graphene oxide by visible light irradiation, RSC Adv. 4 (2014) 25379–25383. doi:10.1039/c4ra01537a.

[230] J.J. Luo, I.M. Daniel, Characterization and modeling of mechanical behavior of polymer/clay nanocomposites, Compos. Sci. Technol. 63 (2003) 1607–1616. doi:10.1016/S0266-3538(03)00060-5.

[231] S. Komarneni, Nanocornposites, 2 (1992) 1219–1230. doi:10.1039/JM9920201219.

[232] P.B. Messersmith, E.P. Giannelis, Polymer-Layered SIlicate Naocomposites: In Situ Intercalative Polymerization of E-Caprolactone in Layered Silicates, 5 (1993) 1064–1066. doi:10.1021/cm00032a005.

[233] J. Texter, Graphene dispersions, Curr. Opin. Colloid Interface Sci. 19 (2014) 163–174. doi:10.1016/j.cocis.2014.04.004.

[234] D. Kim, H.S. Lee, J. Yoon, Highly bendable bilayer-type photo-actuators comprising of reduced graphene oxide dispersed in hydrogels, Sci. Rep. 6 (2016) 1–10.

doi:10.1038/srep20921.

[235] Y. Wu, M. Cai, X. Pei, Y. Liang, F. Zhou, Switching friction with thermal- responsive gels, Macromol. Rapid Commun. 34 (2013) 1785–1790. doi:10.1002/marc.201300649.

[236] L. Breuer, M. Raue, M. Kirschbaum, T. Mang, M.J. Schöning, R. Thoelen, T. Wagner, Light-controllable polymeric material based on temperature-sensitive hydrogels with incorporated graphene oxide, Phys. Status Solidi. 212 (2015) 1368–1374. doi:10.1002/pssa.201431944.

[237] A. Flores, H.J. Salavagione, F. Ania, G. Martínez, G. Ellis, M.A. Gómez-Fatou, The overlooked role of reduced graphene oxide in the reinforcement of hydrophilic polymers, J. Mater. Chem. C. 3 (2015) 1177–1180. doi:10.1039/C4TC02425G.

[238] A. Gaffer, D. Aman, Preparation and Characterization of Conductive Polymer / Reduced Graphite Oxide (RGO) Composite via Miniemulsion Polymerization, 38 (2015) 35–39.

[239] S.B. Lee, S.M. Lee, N. Il Park, S. Lee, D. Chung, Preparation and characterization of conducting polymer nanocomposite with partially reduced graphene oxide, Synth. Met. 201 (2015) 61–66. doi:10.1016/j.synthmet.2015.01.021.

[240] Y. Zhuang, F. Yu, H. Chen, J. Zheng, jie ma, J. Chen, Alginate/graphene double-network nanocomposite hydrogel bead with low-swelling, enhanced mechanical property, and enhanced adsorption capacity, J. Mater. Chem. A. 4 (2016) 10885–10892. doi:10.1039/C6TA02738E.

[241] C. Teng, J. Qiao, J. Wang, L. Jiang, Y. Zhu, Hierarchical Layered Heterogeneous Graphene-poly(N -isopropylacrylamide)-clay Hydrogels with Superior Modulus, Strength, and Toughness, ACS Nano. 10 (2016) 413–420. doi:10.1021/acsnano.5b05120.

[242] A. GhavamiNejad, S. Hashmi, M. Vatankhah-Varnoosfaderani, F.J. Stadler, Effect of H2O and reduced graphene oxide on the structure and rheology of self-healing, stimuli responsive catecholic gels, Rheol. Acta. 55 (2016) 163–176. doi:10.1007/s00397-015-0906-3.

[243] B. Adhikari, A. Biswas, A. Banerjee, Graphene oxide-based hydrogels to make metal nanoparticle-containing reduced graphene oxide-based functional hybrid hydrogels, ACS Appl. Mater. Interfaces. 4 (2012) 5472–5482. doi:10.1021/am301373n.

[244] A.J. Glover, M. Cai, K.R. Overdeep, D.E. Kranbuehl, H.C. Schniepp, In situ reduction of graphene oxide in polymers, Macromolecules. 44 (2011) 9821–9829. doi:10.1021/ma2008783.

[245] Y. Piao, B. Chen, One-pot synthesis and characterization of reduced graphene oxide–gelatin nanocomposite hydrogels, RSC Adv. 6 (2016) 6171–6181. doi:10.1039/c5ra20674j.

[246] T. Jiao, H. Guo, Q. Zhang, Q. Peng, Y. Tang, X. Yan, B. Li, Reduced Graphene Oxide-Based Silver Nanoparticle-Containing Composite Hydrogel as Highly Efficient Dye Catalysts for Wastewater Treatment, Sci. Rep. 5 (2015) 1–12. doi:10.1038/srep11873.

[247] L. Wu, M. Ohtani, M. Takata, A. Saeki, S. Seki, Y. Ishida, T. Aida, Magnetically induced anisotropic orientation of graphene oxide locked by in situ hydrogelation, ACS Nano. 8 (2014) 4640–4649. doi:10.1021/nn5003908.

[248] J. Baruchel, J.-L. Hodeau, M.S. Lehmann, J.-R. Regnard, C. Schlenker, eds., Neutron and synchrotron radiation for condensed matter studies Volume I Theory, instruments and methods, Springer-Verlag, Berlin Heidelberg, 1993.

[249] F. Mezei, Neutron spin echo: A new concept in polarized thermal neutron techniques, Zeitschrift Für Phys. 255 (1972) 146–160. doi:10.1007/BF01394523.

[250] Y. Hertle, M. Zeiser, P. Fouquet, M. Maccarini, T. Hellweg, The Internal Network Dynamics of Poly(NIPAM) Based Copolymer Micro- and Macrogels: A Comparative Neutron Spin-Echo Study, Zeitschrift Für Phys. Chemie. 228 (2014) 1053–1075. doi:10.1515/zpch-2014-0586.

[251] M. Karg, T. Hellweg, New "smart" poly(NIPAM) microgels and nanoparticle microgel hybrids: Properties and advances in characterisation, Curr. Opin. Colloid Interface Sci. 14 (2009) 438–450. doi:10.1016/j.cocis.2009.08.002.

[252] T. Kanaya, N. Takahashi, K. Nishida, H. Seto, M. Nagao, Y. Takeba, Dynamic and static fluctuations in polymer gels studied by neutron spin-echo, Phys. B Condens. Matter. 385–386 I

(2006) 676–681. doi:10.1016/j.physb.2006.05.289.

[253] M. Shibayama, S. Takata, T. Norisuye, Static inhomogeneities and dynamic uctuations of temperature sensitive polymer gels, 249 (1998) 245–252. doi:10.1016/S0378-4371(97)00472-X.

[254] A.-C. Genix, A. Arbe, J. Colmenero, J. Wuttke, D. Richter, Neutron Scattering and X-ray Investigation of the Structure and Dynamics of Poly(ethyl methacrylate), Macromolecules. 45 (2012) 2522–2536. doi:10.1021/ma202653k.

[255] F. Mezei, C. Pappas, T. Gutberlet, Neutron Spin Echo Spectroscopy: Basics, Trends and Applications, 2008. doi:10.1007/3-540-45823-9.

[256] F. Horkay, M. Zrínyi, Studies on the Mechanical and Swelling Behavior of Polymer Networks Based on the Scaling Concept. 4. Extension of the Scaling Approach to Gels Swollen to Equilibrium in a Diluent of Arbitrary Activity, Macromolecules. 15 (1982) 1306–1310. doi:10.1021/ma00233a018.

[257] M. Sztucki, [http://www.esrf.eu/home/UsersAndScience/Experiments/CBS/ID02/available_software.html#, (2017).

[258] J. Ilavsky, P.R. Jemian, Irena: Tool suite for modeling and analysis of small-angle scattering, J. Appl. Crystallogr. 42 (2009) 347–353. doi:10.1107/S0021889809002222.

[259] B. Berke, O. Czakkel, E. Geissler, K. László, L. Porcar, Structure of thermoresponsible nanocomposites below and above the volume phase transition temperature, 2016. doi:10.5291/ILL-DATA.9-12-446.

[260] K. László, Sorption Interactions in Coherent Systems (DSc Thesis), Hungarian Academy of Sciences, 2006.

[261] O. Czakkel, B. Berke, E. Geissler, K. László, Study of the internal dynamics of soft gel – carbon nanoparticle composite systems, 2015. doi:10.5291/ILLDATA. 9-12-374.

[262] B. Berke, O. Czakkel, Internal time on IN11, 2016. doi:10.5291/ILL-DATA.INTER-352.

[263] B. Berke, O. Czakkel, E. Geissler, K. László, Exploring complex internal dynamics in thermoresponsive nanocomposite gels, 2017. doi:10.5291/ILL-DATA.9-12-482.

[264] B. Berke, O. Czakkel, Internal time on IN15, 2017. doi:10.5291/ILL-DATA.INTER-361.

[265] K. László, K. Kosik, C. Rochas, E. Geissler, Phase transition in poly(N-isopropylacrylamide) hydrogels induced by phenols, Macromolecules. 36 (2003) 7771–7776. doi:10.1021/ma034531u.

[266] J.E. Kim, T.H. Han, S.H. Lee, J.Y. Kim, C.W. Ahn, J.M. Yun, S.O. Kim, Graphene oxide liquid crystals, Angew. Chemie - Int. Ed. 50 (2011) 3043–3047. doi:10.1002/anie.201004692.

[267] S.H. Aboutalebi, M.M. Gudarzi, Q. Bin Zheng, J.-K. Kim, Spontaneous Formation of Liquid Crystals in Ultralarge Graphene Oxide Dispersions, Adv. Funct. Mater. 21 (2011) 2978–2988. doi:10.1002/adfm.201100448.

[268] L.S. Ornstein, F. Zernike, Accidental deviations of density and opalescence at the critical point of a single substance, Proc. Acad. Sci. Amsterdam. 17 (1914) 793–806.

[269] P. Pusey, W. van Meegen, P. Pusey and W. van Meegen, , 1989, 157, 705, Physica A. 157 (1989) 705.

[270] E. Geissler, F. Horkay, A.M. Hecht, Scattering from network polydispersity in polymer gels, Phys. Rev. Lett. 71 (1993) 645–648. doi:https://doi.org/10.1103/PhysRevLett.71.645.

[271] Z. Yang, Y. Hemar, L. Hilliou, E.P. Gilbert, D.J. Mcgillivray, M.A.K. Williams, S. Chaieb, Nonlinear Behavior of Gelatin Networks Reveals a Hierarchical Structure, (2016). doi:10.1021/acs.biomac.5b01538.

[272] G. Beaucage, Approximations leading to a unified exponential power-law approach to small-angle scattering, J. Appl. Crystallogr. 28 (1995) 717–728. doi:Doi 10.1107/S0021889895005292.

[273] G. Beaucage, Small-Angle Scattering from Polymeric Mass Fractals of Arbitrary Mass-Fractal Dimension, J. Appl. Crystallogr. 29 (1996) 134–146. doi:10.1107/S0021889895011605.

[274] B. Hammouda, Analysis of the Beaucage model, J. Appl. Crystallogr. 43 (2010) 1474–1478. doi:10.1107/S0021889810033856.

[275] I. Berts, Y. Gerelli, J. Hilborn, A.R. Rennie, Structure of polymer and particle aggregates in hydrogel composites, J. Polym. Sci. Part B Polym. Phys. 51 (2013) 421–429. doi:10.1002/polb.23230.

[276] A. Habicht, W. Schmolke, G. Goerigk, F. Lange, K. Saalwächter, M. Ballauff, S. Seiffert, Critical fluctuations and static inhomogeneities in polymer gel volume phase transitions, J. Polym. Sci. Part B Polym. Phys. 53 (2015) 1112–1122. doi:10.1002/polb.23743.

[277] M. Shibayama, T. Tanaka, Volume phase transtition and related phenomena of polymer gels, Adv. Polym. Sci. 109 (1993) 1–62. doi:10.1007/3-540-56791-7_1.

[278] M. Chalal, F. Ehrburger-Dolle, I. Morfin, F. Bley, M.-R. Aguilar de Armas, M.-L. López Donaire, J. San Roman, N. Bölgen, E. Pişkin, O. Ziane, R. Casalegno, SAXS Investigation of the Effect of Temperature on the Multiscale Structure of a Macroporous Poly(N -isopropylacrylamide) Gel, Macromolecules. 43 (2010) 2009–2017. doi:10.1021/ma902655h.

[279] S. Hashmi, A. Ghavaminejad, J. Stadler, D. Wu, Soft Matter oxide and reduced graphene oxide with grafted, Soft Matter. 11 (2015) 1315–1325. doi:10.1039/C4SM02544J.

[280] W. Kolodziejski, J. Klinowski, Kinetics of Cross-Polarization in Solid-State NMR : A Guide for Chemists, Chem. Rev. 102 (2002) 613–628. doi:10.1021/cr000060n.

[281] S. Wang, D. Ábrahám, F. Vallejos-Burgos, K. László, E. Geissler, K. Takeuchi, M. Endo, K. Kaneko, Distorted Graphene Sheet Structure-Derived Latent Nanoporosity, Langmuir. 32 (2016) 5617–5622. doi:10.1021/acs.langmuir.6b00483.

[282] A. Vértes, S. Nagy, Z. Kulcsár, R.G. Lovas, F. Rösch, Handbook of Nuclear Chemistry, Springer, Dordrecht, Heidelberg, London, New York, 2011.

[283] R.C. Hardy, R.L. Cottington, Viscosity of deuterium oxide and water in the range 5 to 125 C, J. Res. Natl. Bur. Stand. (1934). 42 (1949) 573. doi:10.6028/jres.042.049.

[284] D. Schmaljohann, Thermo- and pH-responsive polymers in drug delivery, Adv. Drug Deliv. Rev. 58 (2006) 1655–1670. doi:10.1016/j.addr.2006.09.020.

[285] G. Kali, S. Vavra, K. László, B. Iván, Thermally responsive amphiphilic conetworks and gels based on poly(N -isopropylacrylamide) and polyisobutylene, Macromolecules. 46 (2013) 5337–5344. doi:10.1021/ma400535r.

[286] K. László, K. Kosik, E. Geissler, High-sensitivity isothermal and scanning microcalorimetry in PNIPA hydrogels around the volume phase transition, Macromolecules. 37 (2004) 10067–10072. doi:10.1021/ma048363x.

[287] K. László, A. Fluerasu, A. Moussaid, E. Geissler, Deswelling kinetics of PNIPA gels, Soft Matter. 6 (2010) 4335–4338. doi:10.1039/csm00297f.

[288] B. Ruta, O. Czakkel, Y. Chushkin, F. Pignon, R. Nervo, F. Zontone, M. Rinaudo, Silica nanoparticles as tracers of the gelation dynamics of a natural biopolymer physical gel., Soft Matter. 10 (2014) 4547–4554. doi:10.1039/c4sm00704b.

[289] A. Madsen, R.L. Leheny, H. Guo, M. Sprung, O. Czakkel, Beyond simple exponential correlation functions and equilibrium dynamics in x-ray photon correlation spectroscopy, New J. Phys. 12 (2010) 1–16. doi:10.1088/1367-2630/12/5/055001.

8.   Appendix

The neutron spin-echo spectroscopy (NSE) data above VPTT was measured at the end of the project and the analysis requires more work before reaching a clear interpretation. In order to keep the results of the project together, the present Appendix contains the preliminary outcomes of these measurements.

Before the NSE measurements at 40 ˚C, the chosen samples were thermalized for 1 day. The internal dynamics of the samples changed significantly upon the VPT. The movement of the polymer units slowed down in all Q values. Due to the collapse, the swelling degree of the gels decreased, which resulted in an increased polymer concentration. The increased amount of hydrogen atom caused strong incoherent scattering, because of which the curves had to be normalized. The normalized curves are shown in Figure A1.

The fitting of the final curves were performed similarly to the low temperature measurements. The baselines were not seen, but after this short time no frozen components were assumed. Only slight variance was observed below the VPTT, but at 40 ˚C, more difference was seen. Based on the macroscopic deswelling measurement, where the GO@PNIPAM systems showed a significantly faster shrinkage in the beginning of the process, the mobility of the chains were expected to be more hindered than in case of the CNT@PNIPAM composites. To compare the differences the dynamic correlation values were determined with the Stokes-Einstein equation. The values are shown at the end of the chapter.
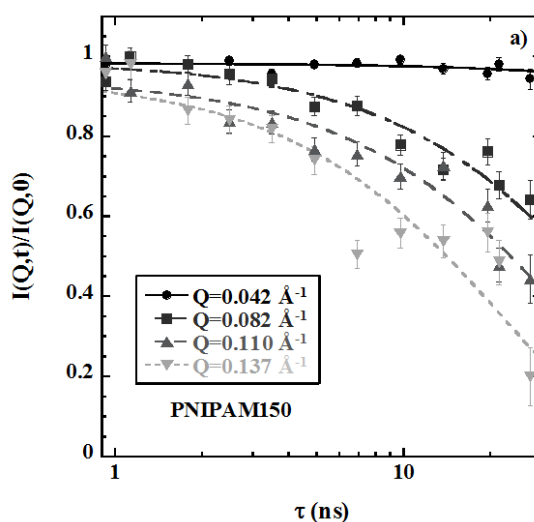

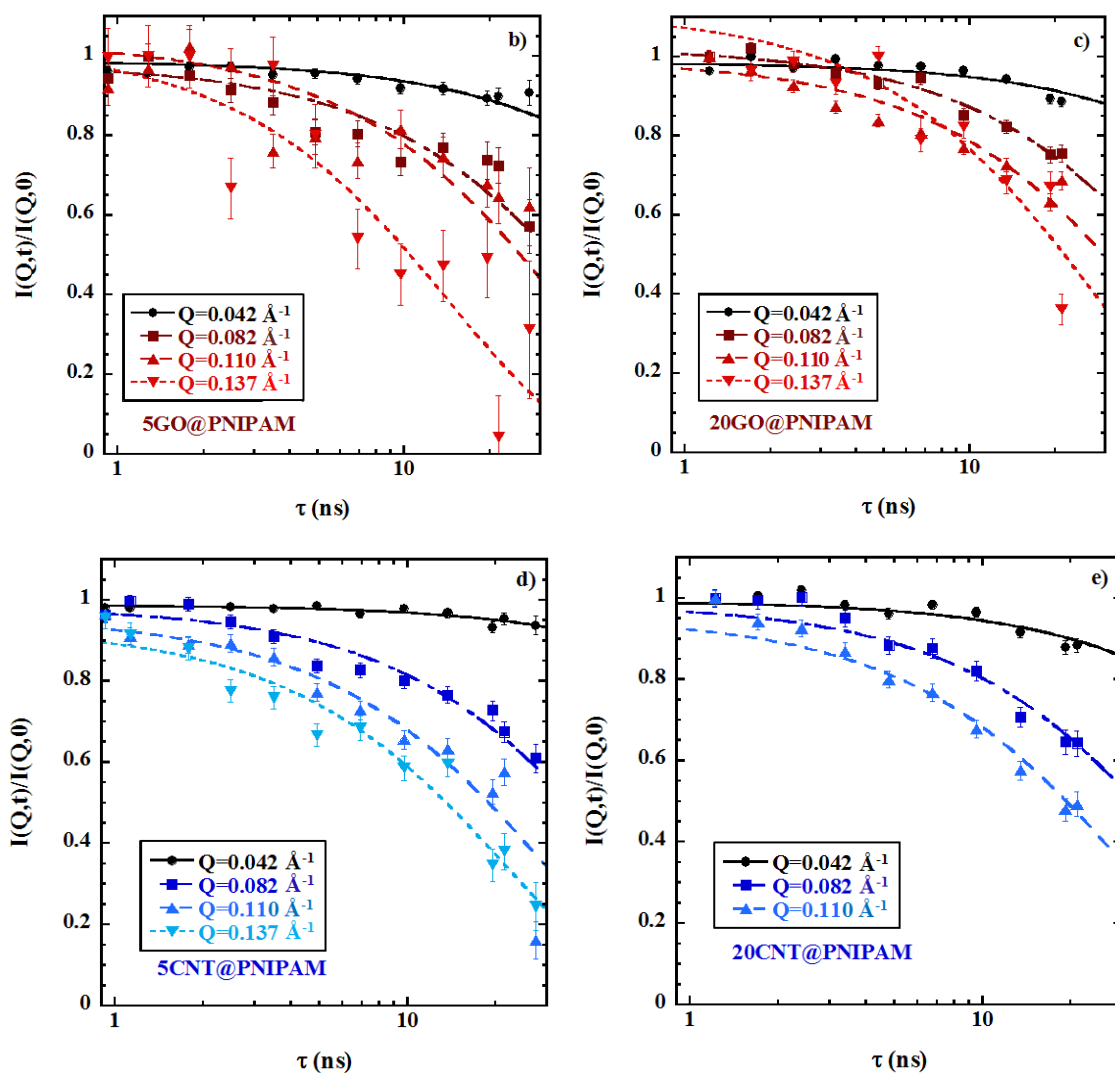*Figure A1. Measured intermediate scattering functions of a) pure PNIPAM150 at 40 ˚C.*

116

*Figure A1. Measured intermediate scattering functions of b) 5GO@PNIPAM,
c) 20GO@PNIPAM, d) 5CNT@PNIPAM and e) 20CNT@PNIPAM) at 40 ˚C after 1 day.*

The reversibility of the observed changes was checked at 1 *Q*-value on one sample by measuring the signal below the VPTT after the measurements above the VPTT. Our results showed that the dynamics completely recovered its original behaviour once the sample is cooled back below the VPTT. It means that the volume phase transition in case of the 5GO@PNIPAM is reversible; no permanent defect of stacking was seen.

To compare the effect of the temperature on the dynamic properties of the collapsed gel, similar measurements were performed at 50 ˚C after 1 day of thermalisation. The observed curves showed, again, slower dynamics than below the VPTT (Figure A2).
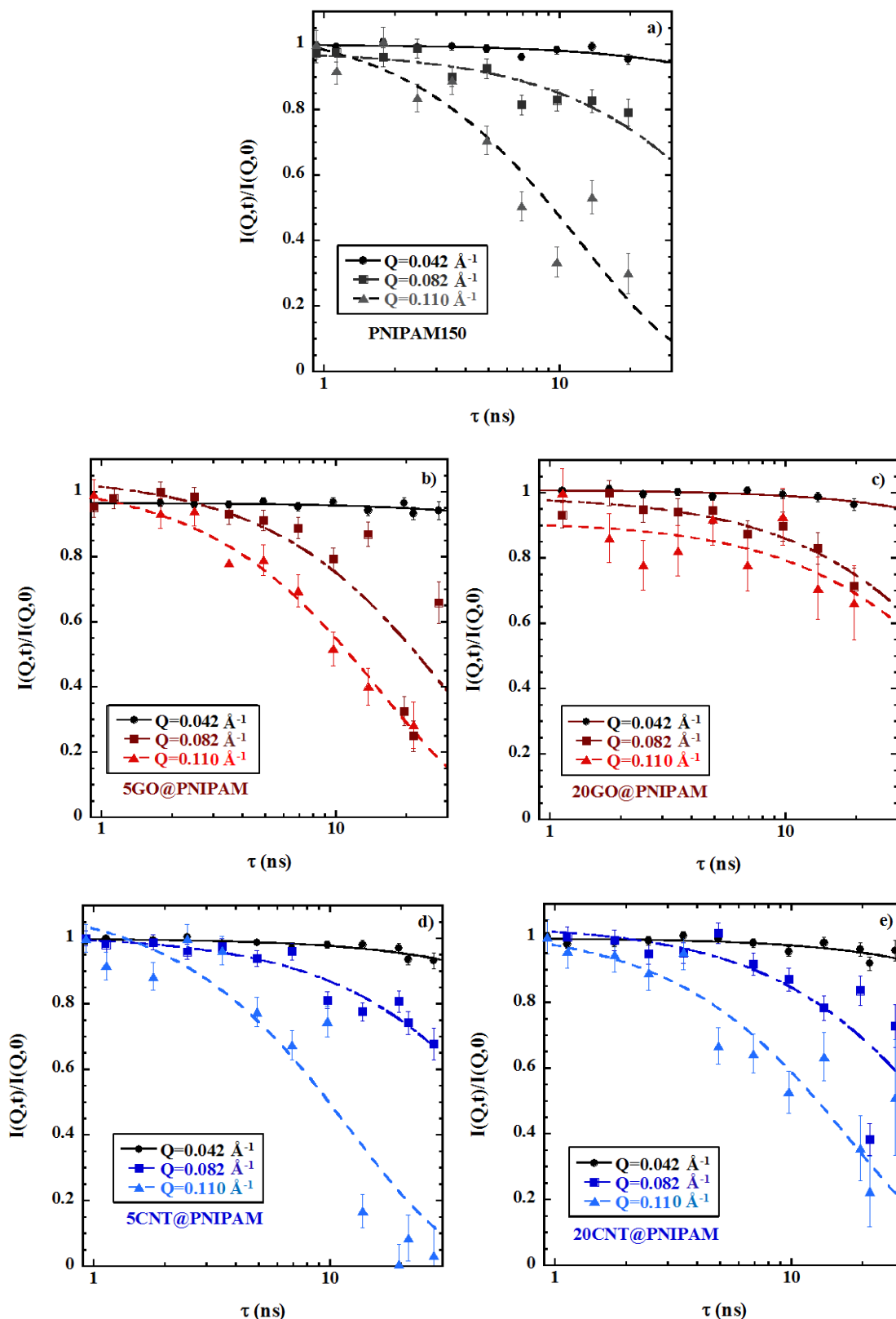
Figure A2. Measured intermediate scattering functions of a) PNIPAM150, b) 5GO@PNIPAM, c) 20GO@PNIPAM, d) 5CNT@PNIPAM and e)20CNT@PNIPAM at 50 ˚C after 1 day

On Figure A3, the already presented below VPTT values were compared with the calculated dynamic correlation length values above the VPTT. The increasing temperature resulted in a larger dynamic correlation length. The polymer chains stuck together, but after 1 day, they were still able to move. In case of the GO@PNIPAM systems, the ξ_H increased with the increasing concentration at 40 and 50 °C as well. Macroscopically, 20GO@PNIPAM shrunk more at both temperatures than 5GO@PNIPAM, which can explain the larger values. CNT@PNIPAM systems shrunk rapidly at 50 °C, therefore the ξ_H values at 50 °C are smaller than those at 40 °C in all cases.
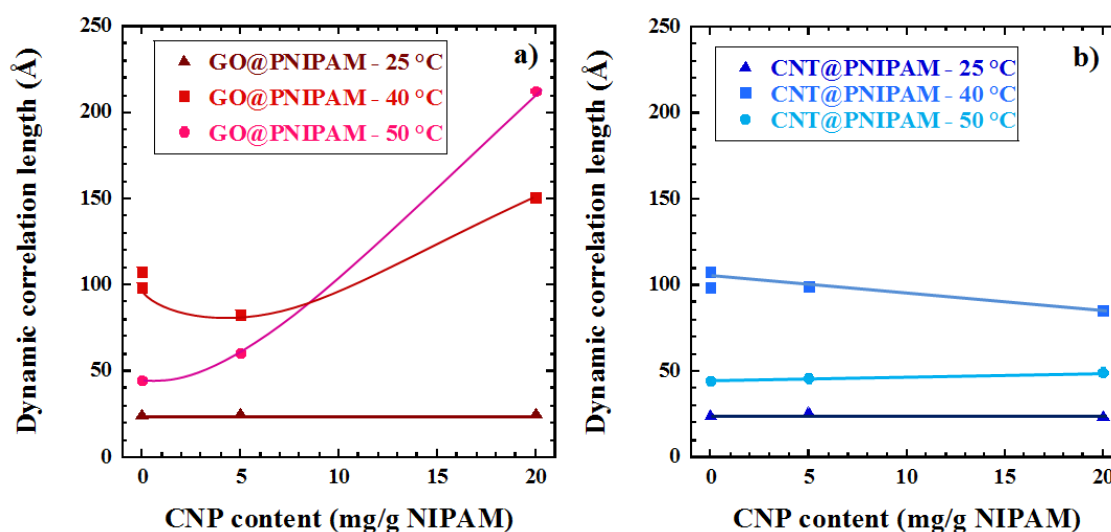

Figure A3. Calculated dynamic correlation length values for a) GO@PNIPAM and b) CNT@PNIPAM systems at 25, 40 and 50 ˚C after 1 day. The solid lines are guides for the eye.

The gel dynamics were studied at 40 ˚C after ~42 days as well. As Figure A4 shows, the dynamics of the gels significantly slowed down. Most likely there were frozen in components owing to the long deswelling process, but the baseline could have not been determined in this time window, therefore, accurate fitting was not possible.
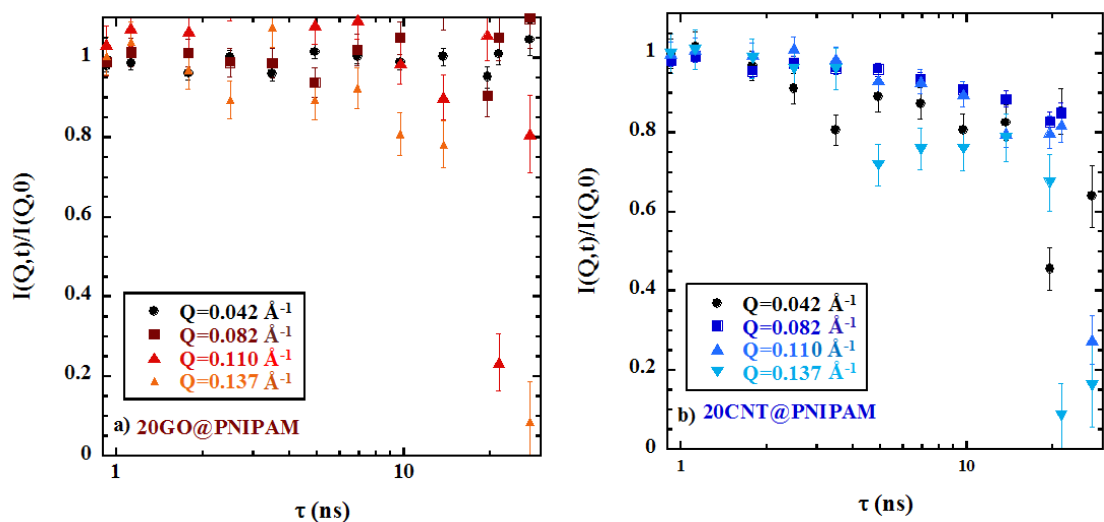
Figure A4. Measured intermediate scattering functions of a) 20GO@PNIPA150 and b)20CNT@PNIPA150 at 40 ˚C after 42 days

In comparison to the samples which spent only 1 day at 40 °C, we can say that the curves of the CNT@PNIPAM composites decayed slightly, but practically no movement could be seen in case of the GO@PNIPAM systems. No *Q*-dependence was seen either. These observations were in accordance with the macroscopic deswelling measurements as well, because the gels were getting closer to the equilibrium state.

NYILATKOZAT

Alulírott Berke Barbara kijelentem, hogy ezt a doktori értekezést magam készítettem és abban csak a megadott forrásokat használtam fel. Minden olyan részt, amelyet szó szerint, vagy azonos tartalomban, de átfogalmazva más forrásból átvettem, egyértelműen, a forrás megadásával megjelöltem.

Budapest, 2018.02.07.

Berke Barbara